Fluorescent Labeling Methods for Super-resolution and Optical-sectioning Imaging

Min Yen Lee

A dissertation

submitted in partial fulfillment of the

requirements for the degree of

Doctor of Philosophy

University of Washington

2020

Reading Committee:

Dr. Joshua C. Vaughan, Chair

Dr. Dustin Maly

Dr. Dan Fu

Program Authorized to Offer Degree:

Chemistry

University of Washington

Abstract

Fluorescent Labeling Methods for Super-resolution and Optical-sectioning Imaging

Min Yen Lee

Chair of the Supervisory Committee:

Professor Joshua C. Vaughan

Departments of Chemistry and Physiology & Biophysics

Throughout the development of light and fluorescence microscopy, a variety of labeling methods have evolved; from mostly affinity-based labeling used in histological staining to specific labeling using antibodies and genetically encoded fluorescent proteins. Recently, there is a growing interest in the *de novo* design of proteins as an alternative to repurposing naturally occurring protein scaffolds. Here I present the method used to characterize the photophysical properties of *de novo* fluorescence-activating β-barrel that are genetically encodable. Also, inspired by well-established histological staining methods, I present a simple labeling method that uses commercially available fluorophores to efficiently, and uniformly, label abundant chemical functional groups on biological specimens for expansion microscopy and cleared tissue microscopy. Amine-reactive fluorophores could effectively label distributions of proteins while aldehyde-reactive fluorophores could show distributions of oxidized carbohydrates. Despite the relatively abundance of such chemical groups, the combination of these covalent chemical stains can powerfully reveal key nanoscale features and general physiological landmarks in a wide variety of thin or thick tissue specimens and fixed cells that were either expanded or cleared.

TABLE OF CONTENTS

Acknowledgements

I am truly grateful to many people in my life who made this learning journey bearable, and fun at times. The PhD journey was completely different from what I had envisioned. I knew it would be tough but could never predict the kind of challenges I would face. I am especially thankful for the patience and guidance from people around me, both in the United States and Singapore.

This thesis would not be possible without the support of the University and the Department. I would like to extend gratitude towards my thesis committee members: Dustin Maly, Dan Fu, and Jesse Zalatan, who have been extremely understanding, supportive and caring throughout my time here.

During my six years of study, the one person who would be the most crucial to my success is my advisor and mentor, Joshua Vaughan. Josh is always excited to talk about science and ideas, and I am glad to have such a great scientific role model as I trained. His tolerance and open-mindedness helped bring our differences together. In addition, I am especially grateful for his care, patience, and constructive criticisms. I wished that I could continue learning more here, but the growth that I had already gained under his wings was significant and definitely helped shape the scientist in me. To Josh, thank you for everything!

Being in the Vaughan Lab, I managed to acquire personal growth, while cultivating my fondness for science and facts. I love the open culture in the group, and everyone is akin to family. Aaron Halpern, our postdoctoral researcher, is equivalent to my brother. I would not be where I am without the additional impactful guidance from Aaron. A lot of my personal and scientific growth can also be attributed to him, and I am extremely thankful for the times we had together. To Aaron, I will miss all the food adventures, boba trips and the lengthy science, crazy ideas, or politics discussion that we had!

I also had the honor to work with Honglin Li, an excellent organic synthetic chemist. I am glad to be able to learn from him and help him with experiments. I am also grateful to Danying Lin, a visiting scientist from China, for her love and care during her short stint here.

The family-like atmosphere would not be complete without other key members of the lab: Lauren Gagnon, Tyler Chozinski, Marco Howard, Chenyi Mao and Marcus Woodworth. Lauren and Tyler, being the first graduate students of the lab, pioneered the awesome lab atmosphere together with Aaron and Honglin. I would like to thank them for their hard work and success in helping to set up the lab in which I was a beneficiary of. Lauren is like my sister and I gained a lot of wisdom from her. Her humor and guidance of all things personal had been great support during this period. I am thankful for Tyler's acumen and advices, and for always responding to my questions.

Marco entered the program in the same year as I did. While we are opposites in some ways, we got along really well, and I thank him for his unwavering support and dim sum trips throughout the years. In my last two and a half years, I enjoyed working with Chenyi, who made the science

a lot more fun as we can bounce ideas and solutions off each other, help each other out, and have someone to share the ups and downs of a project. To Chenyi, thank you for the last two years plus of fun and angst as we try to get the story together and publish! I would also like to show deep appreciation for Marcus who is a brilliant thinker and is able to enlighten me with different perspectives on an issue, be it science, politics, or movies.

I would like to acknowledge past and present undergraduates of the lab: Sarah Parkhurst, Hyeon-Jin Kim, Grant Tremel, Tran Le, Ethan Vo, Jonathon Perr, Leonard Shin and Zachariah Fincher. Every one of them contributed to the the lab and I am pretty sure that I benefited much from the contribution they made. In particular, I would like to extend my deepest gratitude to Sarah, Lee, and her family. It can be challenging and lonely to study in a completely foreign environment and therefore, I am deeply touched by their unconditional love and warmth. Friendships and collaborations made in graduate school (You know who you are! 😊) definitely made learning in classes and in research more enjoyable.

In addition, I have spent a majority of my time working with several professors, lecturers and technicians in teaching undergraduate classes, and would like to thank them: Andrea Carroll, Colleen Craig, Xiaosong Li, Deborah Wiegand, Leesa Kurtz, Dave Lindquist, for always being so understanding and having our backs as we juggle research and teaching. Research would not be possible without the support of several core facilities and staff, such as the NMR, mass spectrometry (Martin Sadilek), photonics research center, and the imaging facility (Wai Pang Chan) by the Department of Biology.

Despite being so far away from home, I am privileged to have friends who never forget and occasionally send me letters and/or care packages. Thank you for thinking of me, Sixiao Lam, Josephine Goh, Kelly Ong, Xiaohan Sim, Pee Mei Tan, and Shufen Ho! I am also grateful for friends who are also my deeply respected seniors providing me with advices and help: Yin Nah Teo, Kim Png and Huibin Zhang. In addition, I am beholden to Uncle Yew Kong and family for their care and support here, as well as Marko and Santi Sandoval for their love and concern. Lastly, and most importantly, I am most grateful to my parents and sister, who continued to love and support me unconditionally while I selfishly persisted through a PhD program. To end off, I would like to include a viral dedication written by Brendan Pietsch, which I found quite amusing.

"I blame all of you. Writing this [dissertation] has been an exercise in sustained suffering. The casual reader may, perhaps, exempt herself from excessive guilt, but for those who have played the larger role in prolonging my agonies with your encouragement and support, well… you know who you are, and you owe me."

(Pietsch, Brendan. Dispensational Modernism. Oxford UP, 2015.)

I thought that was some wicked sense of humor. But it is true that a mere two-page acknowledgements cannot justify the gratitude I have for all the people I have encountered and received help and support from during these years. I owe much. 😊

Dedication

To *Dr. Sydney Brenner*,

whose life, and love for knowledge and learning are my constant source of inspiration and motivation

LIST OF FIGURES

Chapter 1 Figures

Chapter 2 Figures

Chapter 3 Main Figures

Chapter 3 Supplementary Figures

Chapter 4 Figures

LIST OF TABLES

Chapter 2 Tables

Chapter 3 Tables

CHAPTER 1. INTRODUCTION

1.1 Thesis structure

This thesis is organized into four chapters. The first chapter covers the background of various light and fluorescence microscopy developments, followed by a discussion of common labeling techniques used on biological specimens, such as immunolabeling. Chapters two through four include publications and/or protocols that I co-authored. Chapter 2 reports on the method I used to measure photophysical properties of reversible fluorescence-activating protein binders that were designed and published by the Baker Lab. Chapter 3 records the optimization and development of a method to use established reactive fluorophores to stain features of biological specimens with high contrast. Chapter 4 includes an updated protocol and future directions of the staining method developed in Chapter 3.

1.2 Overview: Light Microscopy and Visualizing Biology

Biologists study life over a wide range of length scales, from organisms as large as the blue whale, to microbes so small that they are invisible to the naked eye, and down to the molecular building blocks that all life shares. At these different length scales, biologists use various instruments to visualize organization, which in turn reveals information about function. The basic tools available such as lenses existed long before their first application to biological observations in the 17^{th} century, and the development of light microscopy since has led to the routine visualization of an otherwise unseen biological world. From a single lens used by Leeuwenhoek to modern sophisticated microscopy set-ups with advanced biological sample preparation available now, many areas of science contributed to these advancements.

This chapter briefly reviews some of the tools developed and the major advancements of light and fluorescence microscopy over the years.

1.2.1 Light Microscopy and its limits

In the 17th century, Hooke and van Leeuwenhoek constructed their own rudimentary home-built microscopes to observe biological specimens. Hooke used a compound microscope design, while Leeuwenhoek preferred a simpler design based on a single, carefully-ground ball lens. Because the combination of multiple lenses over a distance introduces undesired aberrations, simple microscopes using a single lens were the choice instrument until the development of achromatic and apochromatic lenses in the 19th century. Besides lens development, researchers have made multiple important advancements in the theoretical and technical aspects that have led to the immense power of the modern light microscope.

1.2.1.1 The diffraction-limit theory of light

One of the most important developments in the 19th century was the diffraction-limit theory of light developed by Airy, Abbe, and Rayleigh. The diffraction-limit theory describes the fundamental resolving limit of the standard light microscope due to the wave properties of light. Diffraction occurs when light wave fronts that pass through an aperture spread out and interfere constructively or destructively. Therefore, when light from a point source travels through an aperture, the diffracted light waves will spread out, producing an image of the point source that is broadened and patterned due to constructive and destructive wave interferences. The diffraction-patterned image of the point source, when magnified, consists of a central disc of a fixed area but larger than the point source surrounded by alternate dark and light rings. This is commonly known as the Airy disc, and the intensity distribution in all directions is the point spread function (PSF). John Herschel first observed this optical phenomenon, and then George Airy characterized the optical phenomenon theoretically.

Ernst Abbe subsequently defined in mathematical terms the lateral spatial resolution limit of light microscopy as approximately half of the imaging wavelength: $d_{x,y} \approx \frac{\lambda}{2NA}$, where $d_{x,y}$ is the lateral spatial resolution (along the *x*- and *y*-axes), λ is the wavelength of light used for imaging, and *NA* is the numerical aperture of the objective lens of the microscope.[1] The numerical aperture (*NA*) is mathematically defined as: $NA = n \cdot sin\,(\vartheta)$, where *n* is the refractive index of

the medium, and ϑ is the maximum half angle of the cone of light entering and exiting the lens. In other words, $d_{x,y}$ is the minimum required distance between two point-source objects in order to distinguish them. Another commonly used criterion in instrumentation is Rayleigh's resolution limit that was established later. Lord Rayleigh based his definition on the ability of the human eye to distinguish the intensity differences of two point-source objects. Lord Rayleigh's mathematical definition was similar in form to Abbe's despite being 22% larger.

As an example, based on Abbe's resolution limit, a lens with a numerical aperture of 1.0 and an illumination wavelength of 500 nm would produce a spatial resolution of at best 250 nm. In other words, any object smaller than 250 nm would always be observed as being at least 250 nm in size. The discrepancy in the actual object size and the observed size underlies the resolution limit of conventional light microscopy and is widely known as the "diffraction limit". Since cells are densely packed with organelles (~30 - 3000 nm) and macromolecules (~2 - 20 nm) that are only a few nanometers apart, the intricate details of cell organization are not resolvable with routine conventional light microscopes. Researchers must turn to other techniques to observe features below the diffraction limit (**Section 1.5**).

1.2.1.2 Optical Contrast

A separate challenge of brightfield light microscopy is achieving optical contrast. Optical contrast is the ability to distinguish an object through the difference in light intensities produced by the object and its background environment. The optical contrast of biological specimens, such as cells, is typically poor under observation with transmitted light. This is due to most specimens being highly transparent and having similar refractive index as water; cells and their features are hard to distinguish from the background environment. To improve brightfield contrast, Köhler designed a new method of illumination, commonly referred to as Köhler illumination. His design improved the specimen's contrast by balancing the illumination and diffusing the image of the light source (filament image). Some other advancements to improve contrast that will not be discussed here include phase contrast microscopy[2,3], polarization microscopy[4] and differential interference contrast (DIC)[5].

Another way to improve contrast is to use fluorescence microscopy (**Section 1.2.2**) that distinguishes the emitted light from the illuminated light. In addition, labeling of specimens (**Section 1.3**) improves contrast through highlighting desired cells and features and are useful for both brightfield and fluorescence microscopy.

1.2.2 Introduction of Fluorescence in Light Microscopy

The first step towards applying fluorescence in microscopy stems from trying to improve image resolution. According to Abbe's resolution limit, one way to improve resolution is to use light with shorter wavelengths. With this idea, Köhler developed the first ultra-violet (UV) microscope and noted that the samples emitted light (auto-fluoresce) upon irradiation with UV light. In 1911, Heimstädt built upon that observation and made further improvements to the microscope through filtering the excitation source to specific UV wavelength using liquid filters, and using a dark background to improve contrast of the luminescent sample.[6] Since then, many improvements to the fluorescence microscope have been made. For example, the advent of dichroic mirrors[7] in 1967 finally developed the standard diffraction-limited fluorescence microscope, that is still used to date for routine biological imaging.

1.3 Overview of Fluorescent Labeling Methods

The term *fluorescence* was first introduced by Stokes in the 19th century.[8] Prior to that, there were many instances of photoluminescence observed, for example, from minerals and chlorophyll.[9] A notable observation about fluorescence was by Herschel who saw blue light emission from colorless quinine in tonic water when illuminated with sunlight. Stokes then experimented and found that quinine absorbed in the UV region and emitted blue light, which was at a longer wavelength than the absorbed light. The difference between the emitted wavelength and the absorbed wavelength is now known as the Stokes Shift. This, in combination with Jablönski's theoretical groundwork (**Fig. 1.1**), later formed the basis for the principles of modern fluorescence spectroscopy and is highly important for fluorescent probes and method development. Since then, many classes of fluorophores have been developed (**Section 1.3.2**) for

various purposes, as well as methods of labeling specimens (**Section 1.3.3 – 1.3.4**) with fluorescent molecules.

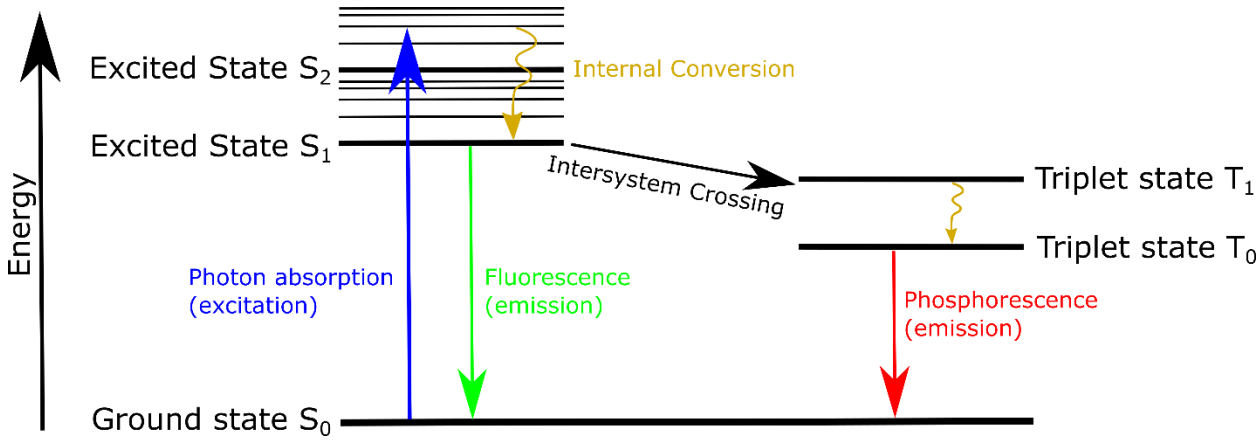

Fig. 1.1. Simplified Jablönski Diagram showing common electronic transitions.

Fluorescence emission (green) is the energy released when an excited molecule returns to ground state.

1.3.1 Overview in Early Histological Staining

The usage of dyes to stain matter have long existed in other industries such as textile manufacturing. The colored extracts from animals and plants was the most common way to obtain the dyes needed for fabric staining. For example, carmine dyes used in textiles were extracted from the cochineal insect. As early as 18th century, biologists applied the use of carmine dyes on biological samples. Since then, there were many applications involved in using a variety of carmine derivative dyes on microorganisms and tissues. Many carmine dye researchers also studied the formulas and cocktails of dye solutions to yield better stains and found that the addition of base, acid, or alcohol helped with stain differentiation, resulting in better specificity.

Besides cochineal dyes, logwood was another popular class of extracted dye. Hematoxylin is one of the dyes in this class and has remained the preferred stain in modern histology. (**Fig. 1.2a**) Purity of hematoxylin was always a concern and hence required crystallization before application to biological samples. Some early researchers also started exploring the possibility of combining hematoxylin with various metals, e.g. copper sulfate. Some metal salts such as aluminum, known as mordants (also used in carmine dyes), help oxidize hematoxylin to hematein

(**Fig. 1.2a**) and forms a positively charged complex. Hematein complex, not hematoxylin, is the form that gives the coloration we see in histologically stained tissues.

The combination that eventually prevailed in modern histopathology uses hematoxylin and eosin (H&E) introduced by Wissowzky in 1876.[10] Eosin (**Fig. 1.2a**) is a derivative of fluorescein. (**Section 1.3.2.1**) As with most histological stains, H&E staining relies on the non-specific affinity of cellular components to the dyes. Hematoxylin stains basophilic (negatively charged) components such as DNA blue while eosin stains acidophilic (positively charged) protein components pink. (**Fig. 1.2b**)

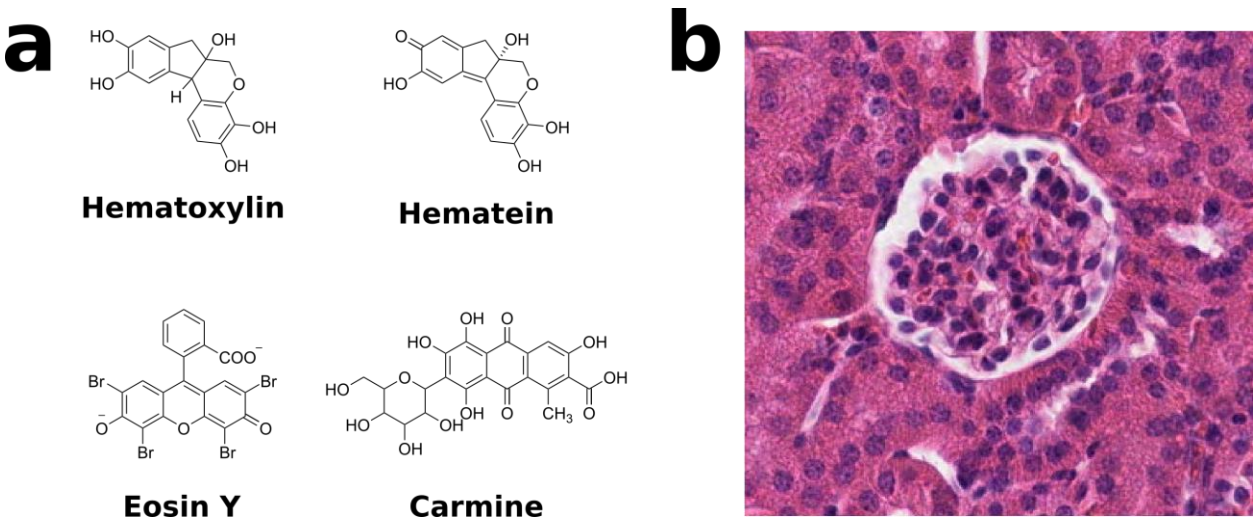

Fig. 1.2. a) Structures of some common histological dyes. b) Example of a H&E stained mouse kidney glomerulus.

1.3.2 Overview in Synthetic Organic Fluorophores

Aniline dyes are a class of well-known synthetic dyes used in textile industry. In the 19th century, aniline was a common waste product in the extraction of coal tar and thus became a widely available starting material for dye synthesis. As such, many experimental researchers during that period contributed to the discovery and synthesis of various aniline derivative dyes. Some aniline dyes used for biological specimens such as methylene blue, methyl violet, aniline blue, are still widely available to date.

Unlike regular pigments, fluorophores are molecules with the ability to emit fluorescence, such as the aniline derivative dyes. While some fluorophores are naturally available and extracted

for use, most modern organic fluorophores now are synthetic and carefully designed. This section briefly discusses several common classes of modern synthetic fluorophores, but many other classes of fluorophores also exist.

1.3.2.1 Common Classes of Synthetic Organic Fluorophores

In 1871, Adolf von Baeyer synthesized fluorescein (**Fig. 1.3**) by using resorcinol and phthalic anhydride.[11] Now, the fluorophore is recognized as a xanthene-based fluorophore and is widely used. In the 20th century, chemists started developing and classifying many other organic fluorophores, such as BODIPY dyes, resulting in the rapid growth of synthetic fluorophores. (**Fig. 1.3**) The majority of them were developed and improved after the introduction of lasers that required fluorophores to have certain photophysical properties such as brightness and photostability. A popular xanthene-based derivative, rhodamine, has great photostability and pH insensitivity.[12] Recently, the quantum yield was further improved by changing the *N,N*-dimethylamino groups to four-membered azetidine rings.[13] In addition, rhodamines were optimized to enable fine spectral tuning through 1) the change of xanthene oxygen to carbon or silicon, and 2) the modulation of the four-membered azetidine rings.[14]

C.H.G. Williams synthesized the first reported blue cyanine dye in 1856.[15] The dye was unstable under light and thus did not have widespread use in textile industry. However, H. W. Vogel discovered the use of cyanine as a sensitizer in photographic emulsions and thereafter cyanine dyes became a stronghold in photography.[15] In 1990s, Alan Waggoner greatly improved the cyanine class of fluorophores, through the addition of sulfonates to enhance solubility[16], rigidization of cyanine chromophores to increase quantum yield and photostability[17], and the attachment of various bioconjugation functional groups to couple the dyes to biomolecules of interest.[16,18–20] This class of fluorophore has great tunability for excitation/emission wavelengths by modulating the length of the polymethine chain and bioconjugation ability through the easy addition of functionalized groups. One of the best dyes in single molecule localization microscopy (**Section 1.5.1**) is Alexa 647, which is a cyanine dye.[21]

Some other dye classes include BODIPY and phenoxazine. BODIPY dyes were introduced in 1968.[22] Since then, chemists have greatly studied the synthesis of various BODIPY dyes[23], as

well as explored various properties of the dyes, such as photostability, solubility and expansion of spectral range into the far-red.[24,25] Resorufin is a widely used phenoxazine dye (**Fig. 1.3**). The resorufin/resazurin system (**Fig. 1.3**) is often used to probe redox activities in cells[26], and electro-chemically induced redox activities on surfaces.[27]

The development of new classes of dyes and the modulation of their properties now allow us to have an extensive palette of dyes for various applications, and multiplex biomolecular labeling within the visible spectrum.[28]

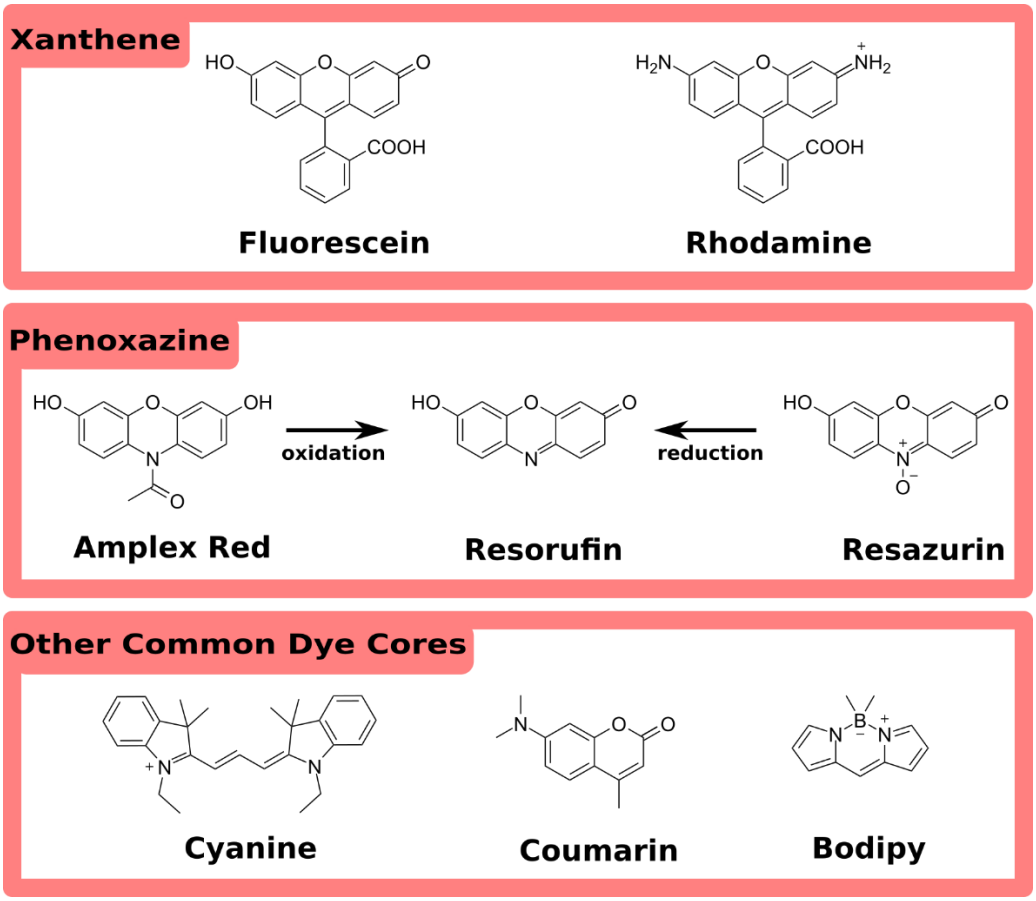

Fig. 1.3. Representative chemical structures of some common classes of organic fluorophores

1.3.2.2 Fluorophores and their properties

The excitation and emission properties of fluorophores depend on the energy gap between the ground and excited state. If the energy gap is small, the amount of energy required to excite the molecule will be low (i.e., red light). The absorbed energy quickly dissipates into

both non-radiative pathways, such as internal conversion, and radiative pathways, such as in the form of fluorescence emission. Due to the non-radiative loss prior to emission, the energy of the emitted photon is less than that of the absorbed photon. Therefore, the wavelength peak for emission is redder than the wavelength peak for absorbance or excitation (Stokes Shift). (**Fig. 1.1**)

The quantum yield efficiency of a fluorophore is defined as the number of photons emitted divided by the number of photons absorbed, while extinction coefficient (molar absorptivity constant) is the value that defines how strongly the fluorophore absorbs at a certain wavelength. **Chapter 2** further discusses the analytical method used to measure quantum yield and extinction coefficient. For traditional fluorescence microscopy, since the brightness of a fluorophore depends on both quantum yield and extinction coefficient, these are the two critical physical properties for dye characterization, besides absorbance/excitation/emission spectra and solubility.

Photostability is also a highly desired characteristic of fluorophores. Fluorophores that resist irreversible photo oxidative damage can remain bright for a longer period leading to more information extracted from the sample. While intrinsically photostable dyes are preferable, chemicals that can prolong the photostability of a wide range of dyes exist. Examples of such chemicals include trolox (TX), cyclooctatetraene (COT), n-propyl gallate (NPG), 1,4-diazabicyclo[2.2.2]octane (DABCO), para-nitrobenzyl alcohol (NBA), methyl viologen/ascorbic acid (MV/AA). Although the mechanisms used by these chemicals require more studies, some proposed mechanisms include reducing and oxidizing system (ROXS), inhibiting singlet oxygen, or quenching triplet state (TSQ).[29–31] Enzymatic oxygen scavengers systems, such as commonly used glucose oxidase/catalase (GLOX) system,[32] are also used to improve photostability. While some oxygen scavenging systems such as GLOX causes pH to change due to production of carboxylic acids in the process, there are alternative non-acidifying systems developed. One such example is the pyranose oxidase/catalase system[33] that produces ketones instead of acids. These photostabilizing agents can be used individually or in combination to improve performance.[30,34]

1.3.3 Immuno-tag overview: Antibodies

In the past, most biological sample staining requires incubation in dye solutions and observation of non-specific, affinity-based, non-covalent interactions of dyes on samples. (**Section 1.3.1**) However, in 1941, Albert Coons and co-workers revolutionized the way biology is labeled and visualized by using fluorescently conjugated antibody to specifically label biological specimens.[35] In a series of experiments, they added a reactive isothiocyanate group to fluorescein for easy covalent attachment to antibody. Since then, it is routine to use fluorophore-conjugated antibodies for specific detection and the types of fluorophores (**Section 1.3.2**) used have vastly expanded.

Multiplexing is possible by using fluorophores with different excitation and/or emission spectra coupled to secondary antibodies. These fluorophore-conjugated secondary antibodies then bind to the primary antibodies that specifically target desired proteins in the biological sample. Multiplexing is also further achievable by raising the primary and secondary antibodies in a variety of animal hosts. Moreover, many studies were done on bioconjugation to improve the efficiency of labeling and expand the type of labeling chemistry possible, such as n-hydroxysuccinimide activated esters.[36] While immunolabeling provides detection of specific proteins, the use of antibodies has its own set of challenges, such as slow penetration into thick biological specimens (**Section 1.4.3**) and high lot-to-lot variability.[37]

1.3.4 Genetic-tag overview: Fluorescent Proteins

Previously, the labeling of biological samples required samples to be fixed and have the stains added externally. This changed with the discovery of fluorescent proteins (FPs). Now, it is possible to tag a fluorescent protein to a protein of interest in live cell and observe what happens. Although green fluorescent protein (GFP) was first isolated from jellyfish in 1962[38], researchers were only able to express viable proteins outside of jellyfish in 1994 after a 30-year gap.[39] The work on GFP revolutionized the way researchers are able to investigate biology, and was awarded the Nobel Prize in Chemistry in 2008.[40]

Since the discovery of GFP, exploration of other marine organisms and the use of protein engineering led to the discovery and innovation of other fluorescent proteins, including those that emit in other channels such as the red or far-red region.[41–46] (**Fig. 1.4a**) Due to increasing popularity in using FPs for biological investigation, there is a need for better variants that are brighter, more photostable, have a higher rate of chromophore maturation, and that are smaller in size. In addition, smaller monomeric FPs are more favorable as protein fusion tags. In the past several years of fluorescent protein engineering, researchers have discovered and developed many prototypes that filled the entire visible spectrum. (**Fig. 1.4b**)

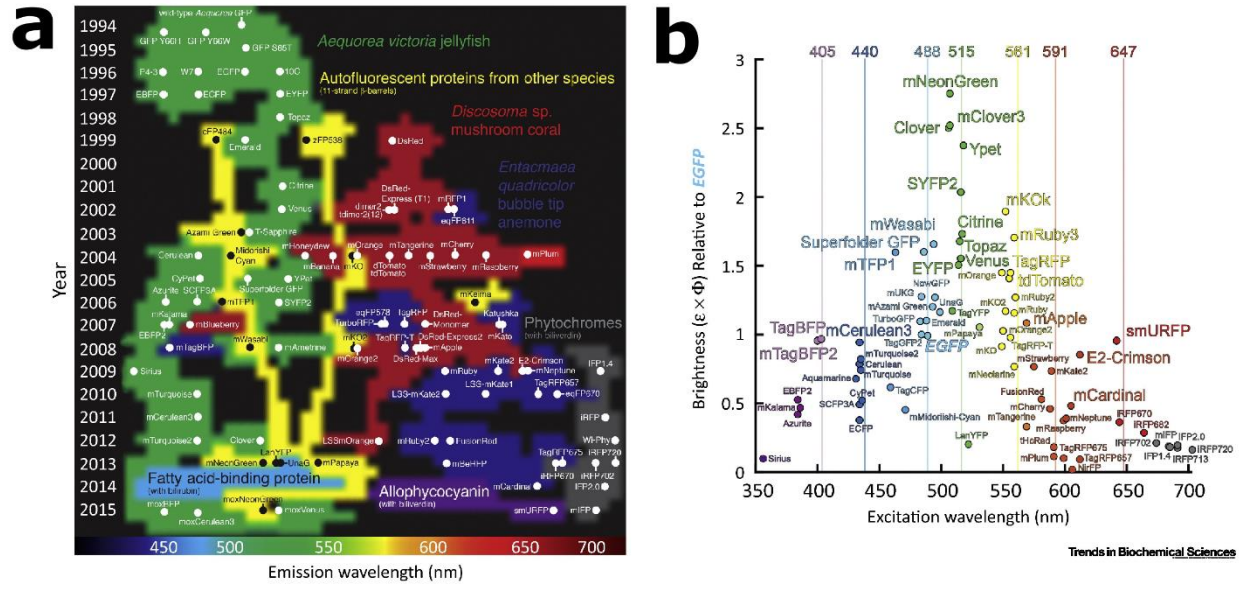

Fig. 1 4. An overview of fluorescent proteins introduced since the expression of GFP in 1994.

a) Chart of the year when the FP was introduced relative to the peak emission wavelength. Shown on the chart are 11-stranded β-barrel homologs of GFP, as well as proteins that are fluorescent when bound to a biliverdin or bilirubin chromophore. b) Plot of Intrinsic fluorescent brightness (ε x ϕ) of selected FPs relative to EGFP against peak excitation wavelength. Vertical lines at 405 nm, 440 nm, 488 nm, 515 nm, 561 nm, 591 nm, and 647 nm indicate commonly available laser lines on fluorescence microscopes. Figure and caption adapted with permission from Rodriguez *et al.*[47] Trends in Biochemical Sciences. Copyright Cell Press, Elsevier Ltd.

Besides engineering for traditional fluorescence microscopy, there are efforts made to develop fluorescent proteins that can photoswitch between distinct fluorescent states or can photoactivate from a nonfluorescent to a fluorescent state when exposed to light of certain wavelength. Single-molecule-based super-resolution microscopy widely uses the ability of

fluorescent proteins to undergo intermittent fluorescent emission ("blinking"). (**Section 1.5.1**) This intermittent fluorescent emission is a result of fluorescent proteins switching between two different molecular states (photochromism). This mechanism was established in 1997[48] with further efforts in categorizing the various mechanisms, such as cis-trans isomerization.[49,50] In 2002, Patterson and Lippincott-Schwartz published the first designed photoactivatable protein by mutagenesis.[51]

1.3.5 Summary of Fluorescent Labeling Methods

In summary, staining of biological specimens have undergone various advancements in the method of labeling, as well as the chemistry of pigments, fluorophores, and conjugation. Biologists first used non-specific affinity-based dyes, then progressed onto specific labeling through using antibody and fluorescent proteins. Coupling with the advancement in labeling methods, the chemistry and synthetic design of dyes and fluorophores have advanced significantly resulting in a huge palette of dyes for researchers to use. In addition, the development of labeling methods had spurred on the design of various bioconjugation chemistries.

1.4 Overview of Thick Specimen Imaging

Recently, there is an increasing trend in seeking volumetric structural information from biological specimens. The knowledge gain from the details of three-dimensional (3D) structures allow biologist to gain better inferences and put function into perspective. However, imaging of thick specimens (>100 μm) faces several key challenges. In order to image thicker specimen (>500 μm), researchers developed a method that requires imaging a series of thin sections that are reconstructed into a three-dimensional image.[52] While such methods are useful, they are destructive towards samples and prone to distortions. For imaging of a thick specimen without destructive physical sectioning, researchers have developed several optical-sectioning methods (**Section 1.4.1**) that filter out-of-focus and background light. In addition, for optical-sectioning methods to work well, the thick specimen must allow light to enter and leave without unwanted light scattering. Hence, researchers have also created a multitude of tissue-clearing methods to

reduce light scattering in biological tissues (**Section 1.4.2**). A final challenge of thick sample imaging lies in labeling the sample uniformly as briefly mentioned, above, in **Section 1.3.3**, and as will be further elaborated in **Section 1.4.3**.

1.4.1 Optical Sectioning Methods

The quest for thick, non-destructive 3D imaging has led to the development of many optical-sectioning techniques such as confocal microscopy, laser scanning two-photon microscopy, light sheet microscopy and computational image deconvolution. This chapter briefly focuses on the most widely used techniques, confocal microscopy (**Section 1.4.1.1**) and light sheet microscopy (**Section 1.4.1.2**).

1.4.1.1 Confocal Microscopy

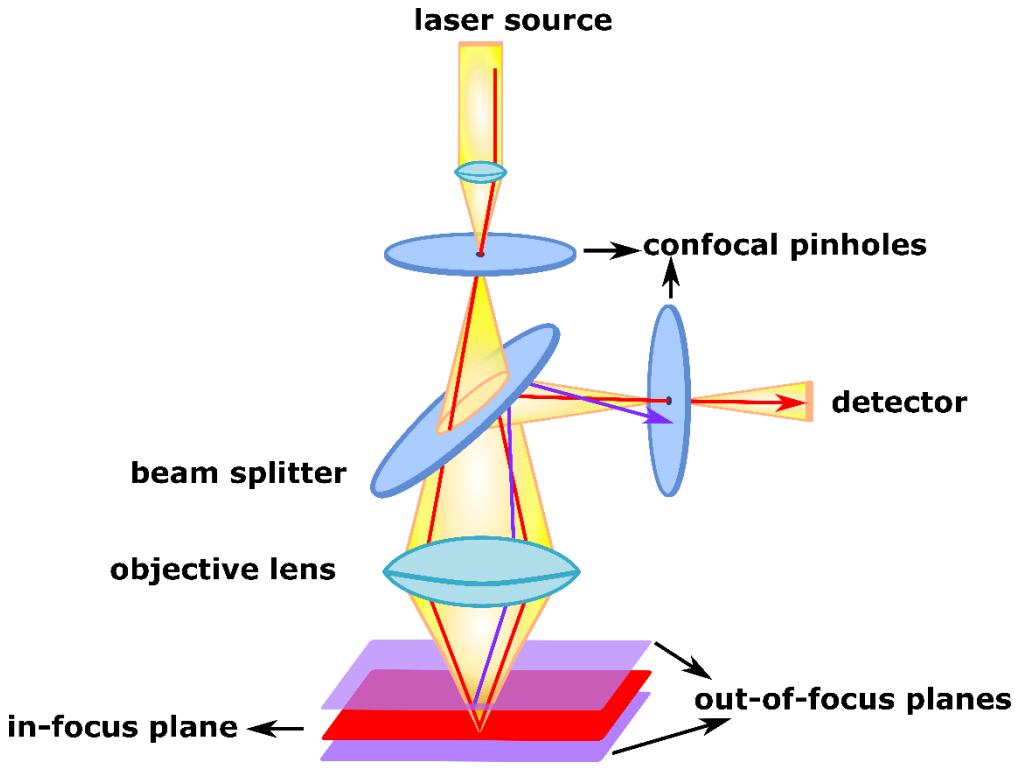

Fig. 1.5. Schematic diagram of a confocal microscope.

Excitation laser light passes through the first pinhole, beam splitter, objective lens and finally impinges on sample. Only emitted light from the in-focus plane of the sample (red) can pass through the second conjugate pinhole onto the detector. Most out-of-focus light emitted from the sample (purple) is unable to reach the detector.

Marvin Minsky developed the first confocal microscope to minimize out-of-focus light in 1956.[53] However, the light source for confocal microscope must be sufficiently powerful enough to allow enough emitted light to be collected through the conjugate pinhole in order to obtain adequate signal. Due to the low power of the available incoherent light source at the time, the idea of confocal microscopy was not widely utilized. Lasers developed from the 1960s helped to improve and build the confocal laser scanning microscope in 1978. The advancement of lasers and computers allowed the commercialization of the laser point-scanning confocal microscope, which is now a routine imaging tool for biology.

In a confocal microscope, an objective lens focuses a collimated laser beam to a small spot within the sample. Fluorescence is excited along the entire path of the laser beam, both before and after the focus spot, but a pinhole is installed in the detection path so that only light emitted by the sample from the in-focus plane can pass through the pinhole to the detector. Thus, the pinhole effectively works to filter away light emitted from out-of-focus planes, rejecting contaminating background fluorescence at each plane, and enhancing spatial resolution. (**Fig. 1.5**) In order to observe a larger area and build up an image, the focal spot is raster-scanned across the sample.

1.4.1.2 Light Sheet Microscopy

Light sheet microscope can expose and image a thin sheet quickly, instead of illuminating the entire depth of the sample. Therefore, a thicker sample can be imaged with minimized photobleaching. Although Siedentopf and Zsigmondy published the first version of light sheet microscope in 1902[54], it did not spur any further developments until the late 20th century. The concept was re-introduced by Voie and coworkers as they developed a system named orthogonal-plane fluorescence optical sectioning (OPFOS) in 1993 to look at hair cell structure and other cochlear features.[55] But it was the publication of single-plane illumination microscopy (SPIM) by Huisken and coworkers in 2004 that boosted the development of the light sheet fluorescence microscopy.[56] Since then, many designs by different researchers have been published.[57] In particular, the lattice light sheet microscope achieved excellent spatiotemporal resolution in a wide variety of living specimens with low phototoxicity.[58]

1.4.2 Optical Clearing Methods

Despite developments in optical-sectioning methods, it is still challenging to image thick specimens due to intrinsic light scattering in tissue specimens. As such, it is popular to use optical clearing methods in combination.[59] This section will briefly discuss two main categories of optical clearing: organic solvent-based clearing (**Section 1.4.2.2**) and aqueous-based clearing (**Section 1.4.2.3**).

1.4.2.1 Overview of light scattering in tissues

Tissue consists of many different types of molecules in various environments, such as lipids, membranes, organelles, collagen fibers etc. Due to the heterogeneity of tissue at the micro- and nanoscopic size ranges, refractive index mismatches occur throughout the sample resulting in the scatter of light. However, as the wavelength of light is increased with respect to the size of the features, the scattering is reduced, which results in improved thick tissue imaging in the infra-red region. For both categories of optical clearing methods, the end goal is to minimize light scattering by homogenizing the refractive indexes of the tissue so that light can pass through the sample more efficiently and to avoid optical aberrations.

1.4.2.2 Organic Solvent-based Clearing

This method of clearing uses organic solvents to remove water and lipids from tissues. The removal of these components increases the refractive index of the sample as dehydrated proteins have a high refractive index of >1.5, similar to that of coverslip glass and immersion oil (refractive index of 1.51). The sample is treated with an organic solvent, typically an alcohol, which is miscible in water and can dissolve lipids. In some methods, the sample undergo gradual dehydration and delipidation through incubation with increasing concentrations of the organic solvent. Finally, the completely dehydrated sample undergo index-matching with a second organic solvent of similar refractive index of >1.5. (**Fig. 1.6**)

Dehydration is commonly performed using methanol[60], ethanol[61] or THF[62,63], while common final clearing solutions include benzyl alcohol[61], benzyl benzoate[61], methylsalicilate[64], dibenzyl ether[62,63], ethyl cinnamate[65], and dichloromethane[63].

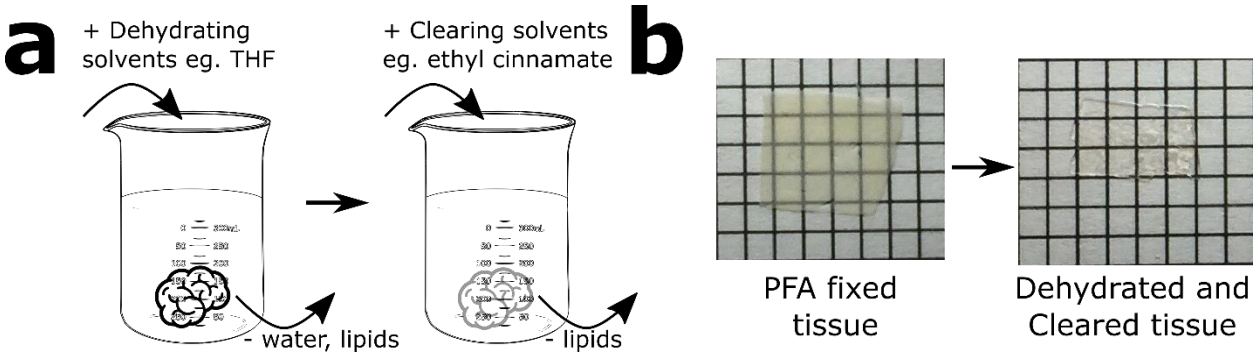

Fig. 1.6. Overview of organic-based clearing

a) Simplified diagram of the process of organic-based clearing process, whereby the dehydration step removes most of the water and lipid, and the clearing step removes the remaining lipid present and homogenizes the refractive index of the sample. b) An example of a human prostate tissue section that underwent the process of dehydration and ethyl cinnamate clearing.

1.4.2.3 Aqueous-based Clearing

Depending on the type of experiments, the dehydration process in organic-based clearing results in issues such as tissue shrinkage or distortion. In addition, fluorescent proteins in genetically modified tissues do not remain fluorescent after the harsh dehydration step in organic solvent-based clearing. Although researchers finally improved organic solvent-based clearing for fluorescent proteins[63,66], their fluorescent signals are only retained for a few days. Therefore, there is an increasing trend in using aqueous-based clearing. The three main categories of aqueous-based clearing include: 1) immersing the sample in solution that has the same refractive index as the tissue, 2) lowering the refractive index of the tissue by removing lipids and hydrating the sample, and 3) immersing the sample in refractive index matched solution after active or passive removal of lipids.

In order to clear a hydrated tissue specimen containing lipids simply by immersion, a solution containing high refractive index molecules of >1.45 is used. Some examples include glycerol[67], fructose[68], sucrose[69], formamide[70], 2,2'-thiodiethanol[71–73] and histodenz[74]. While

passive immersion is not the best at tissue clearing, it is simple with broad compatibility with different dyes and fluorescent proteins. (**Fig. 1.7a**) Another method is to remove lipids in the sample via surfactants such as Triton-X and further hydrate the sample using urea in the presence of glycerol[75] or index-match the delipidated sample with sucrose.[76] (**Fig. 1.7b**) The loss of proteins during lipid clearing lead to the development of hydrogel-embedding methods which first crosslink the proteins of tissue in a polyacrylamide polymer to provide the tissue with structure and minimal protein loss in the clearing process.[77]

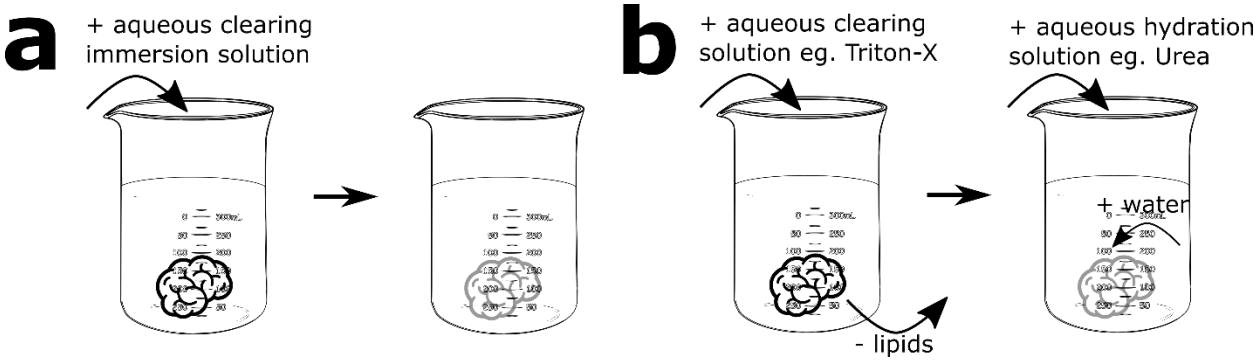

Fig. 1.7. Overview of aqueous-based clearing

a) Simplified diagram of the process of aqueous-based clearing via simple passive immersion and b) Simplified diagram of the process of aqueous-based clearing via lipid clearing and urea. Urea/formamide denatures the proteins and induces water to get into hydrophobic spaces for homogenous clearing.

1.4.3 Improving Thick Sample Labeling for Imaging

Another aspect of large specimen imaging relies on accurate and uniform labeling of the specimens. Immunolabeling is a widely used technique to highlight desired features in cells and tissues. While immunolabeling on cells and thin specimens (<10 μm) are common and easy, larger specimens remain a challenge. This is due to slow passive diffusion of antibodies through large complex structures, thus requiring long incubation times (>weeks). Even with unlimited time and large quantities of antibodies, the stain through large specimens is still uneven. The use of large amounts of antibodies makes optimization for various types of biological specimens expensive and difficult.

Therefore, researchers are finding various ways to rapidly label large specimens. One such method uses electrophoresis to efficiently transport labels through various types of biological

tissues. In some cases this can shorten the antibody incubation times from weeks to a day, but the method requires the use of custom hardware and considerable optimization.[78]

1.5 Overview of Super-resolution Microscopy Techniques

The diffraction limit of light (~250 nm) does not allow biological features closer than 250 nm to be fully resolved, thus obscuring the interrogation of biological structures using light microscopy. To overcome the diffraction limit, several groups have developed super-resolution methods that allow researchers to probe such nanoscale structures. Some of these methods were recognized with the 2014 Nobel Prize in Chemistry, including Single-molecule Localization Microscopy[79,80] (SMLM), and Stimulated Emission Depletion[81] (STED). This section focuses on super-resolution methods such as SMLM, STED, Structured Illumination Microscopy[82] (SIM), and Expansion Microscopy[83] (ExM). This section also includes a brief discussion on the challenges of super-resolution methods. (**Section 1.5.6**)

1.5.1 Single-Molecule Localization Microscopy (SMLM)

In conventional microscopy, the camera typically detects the overlapping, blurry images of an ensemble of fluorophores labeling the sample. In contrast, SMLM achieves high spatial resolution by sequentially switching on sparse, resolvable subsets of fluorophores that are individually localized with low uncertainty. The fluorescent probes within a diffraction-limited space are stochastically turned on and off to reveal their individual positions through various mechanisms.[84–87] The locations of each turn-on event are then detected and recorded using a highly sensitive camera, localized with low uncertainty to their estimated true position using a suitable mathematical model, and finally reconstructed through the combination of a large set of single molecule positions to obtain a high resolution image. (**Fig. 1.8**)

The concept of using single-molecule localization to reconstruct an image was proposed by Burns *et al.*[88] in 1985 and Betzig[89] in 1995. However, the implementation of the theory in densely labeled regions proved to be difficult. The discovery of photoswitchable organic fluorophore[90,91] allowed Rust and coworkers to develop a technique called Stochastic Optical Reconstruction Microscopy[80] (STORM). At the same time, the discovery of photoactivatable

fluorescent proteins[87] allowed Betzig to put his theory into action, and developed Photoactivatable Localization Microscopy[79] (PALM). Although PALM and STORM were reported in separate publications, both method developers recognized that their methods are compatible with any photoswitchable organic fluorophores or photoactivatable fluorescent proteins. Both PALM and STORM are the pioneering methods and now amongst some of the many acronyms and variations of the SMLM method subsequently developed.

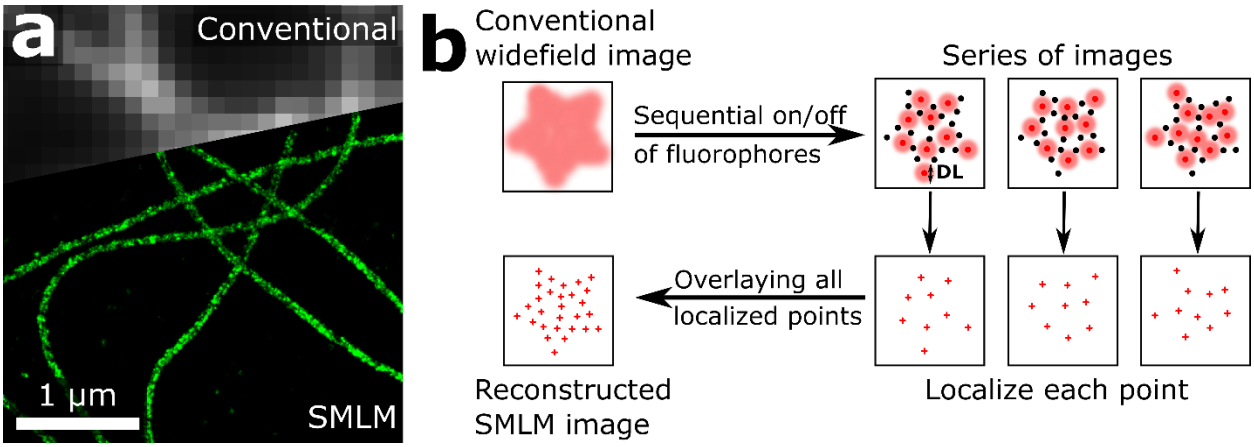

Fig. 1.8. Overview of SMLM.

A partial SMLM/Conventional image overlay showing a fixed cell immunostained for alpha-tubulin. b) Simplified diagram showing how SMLM bypasses diffraction limit (**DL**) by the reconstruction of single fluorophore localizations.

1.5.2 Stimulated Emission Depletion Microscopy (STED)

Another super-resolution technique developed was the Stimulated Emission Depletion Microscopy (STED).[81] This idea, by Hell and coworkers, is similar in part to a laser confocal point-scanning microscope (**Section 1.4.1.1**). However, unlike the confocal microscope, STED requires two superimposed illumination beams. The first illumination beam is a Gaussian-shaped beam used to excite the fluorophores. The second illumination beam is red-shifted and shaped like a donut to act as a depletion beam through a process called stimulated emission that transitions excited fluorophores back to their ground state at the same wavelength as the depletion beam. The purpose of the second, donut-shaped illumination beam is to de-excite the fluorophores toward the periphery of the excitation Gaussian beam such that, when stimulated emission is saturating, spontaneous fluorescence is only detected from fluorophores in a small fraction of

the initial excitation volume. (**Fig. 1.9**) The fluorescence emission is different from the spectral region of the two illumination beams as well as the photons released by the stimulated emission process, and thus easily monitored. By superimposing the beams, the method is successful in narrowing the PSF and is typically able to achieve a spatial resolution of ~30 – 70 nm.[92–94]

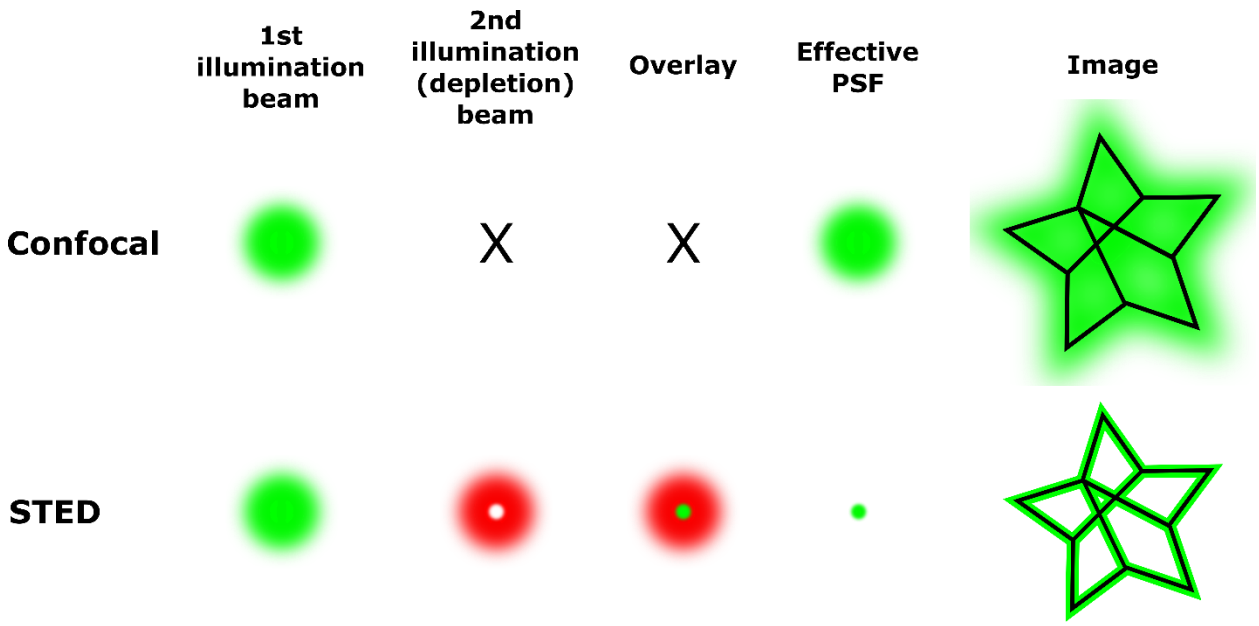

Fig. 1.9. Overview of STED.

The difference between STED and a point-scanning confocal is the use of the 2nd illumination (depletion) beam that effectively shrinks the emission PSF resulting in a much higher resolution image.

1.5.3 Structured Illumination Microscopy (SIM)

SIM uses periodic patterned illumination to derive high spatial frequency information from a sample and there were a few significant developments towards its advancement. One of those earlier developments include work by Bailey and coworkers.[95] Their standing wave microscopy set-up improved axial resolution through interfering illumination patterns from overlapping laser beams. Later, Heintzmann and Cremer presented laterally modulated excitation microscopy, the first case of SIM.[96] The method was then further improved by Gustafsson and coworkers in 2000 that gives a spatial resolution of ~110 nm.[82] Since then, there have been many modifications and improvements from various research groups.[97]

After light passes through the regular wide-field microscope, structural details associated with high spatial frequency information are typically lost. To retain the high spatial frequency information, structured illumination mixes that information into the low frequency region that is within the spatial frequency bandwidth of the optical transfer function of the microscope. This results in the extension of frequency region observed and thus improves resolution. Structural illumination enables such spatial frequency information mixing through exciting the sample with a sinusoidal illumination pattern. The interaction between the high frequency illumination pattern and the high frequency structural details within the sample produces a lower frequency pattern, in which high frequency spatial information can be derived. A series of these patterned images at varying angles and phases is obtained and computationally analyzed to reconstruct a high-resolution image. Two-dimensional or three-dimensional SIM is possible and can achieve a lateral spatial resolution of ~110 nm.

1.5.4 Expansion Microscopy (ExM)

In 2015, Chen *et al.* developed another super-resolution method known as Expansion Microscopy (ExM).[83] ExM can resolve features within a diffraction-limited area by physically expanding the biological specimens to ~4× its original size and is similar to an aqueous-based hydrogel embedding clearing method. The amines of a biological specimen are covalently attached to a monomer that is incorporated into a swellable hydrogel grown within the specimen through free radical polymerization. The two common ways of attaching a monomer to amines in biological specimens include either using NHS-activated monomer[98,99] such as NHS-activated methacrylic acid or a methylolation reaction using paraformaldehyde, methanol and acrylamide[100]. After that, the specimen is digested with proteolytic enzymes[83,98,99] or denatured with heat and detergent[100] in order to soften tough components of the specimen that may otherwise resist expansion (**Fig. 1.10**). The digested or denatured hydrogel-embedded biological samples expand ~4× isotropically along each axis after incubation in pure water. Unlike SMLM, SIM or STED, the expanded samples can be easily imaged on commonly accessible epifluorescence or confocal microscopes. In the years since the first ExM publication, many

variations and subsequent innovations have been published,[98,99,101–107] and the technique has been widely used in a number of different biological specimens.[108–115]

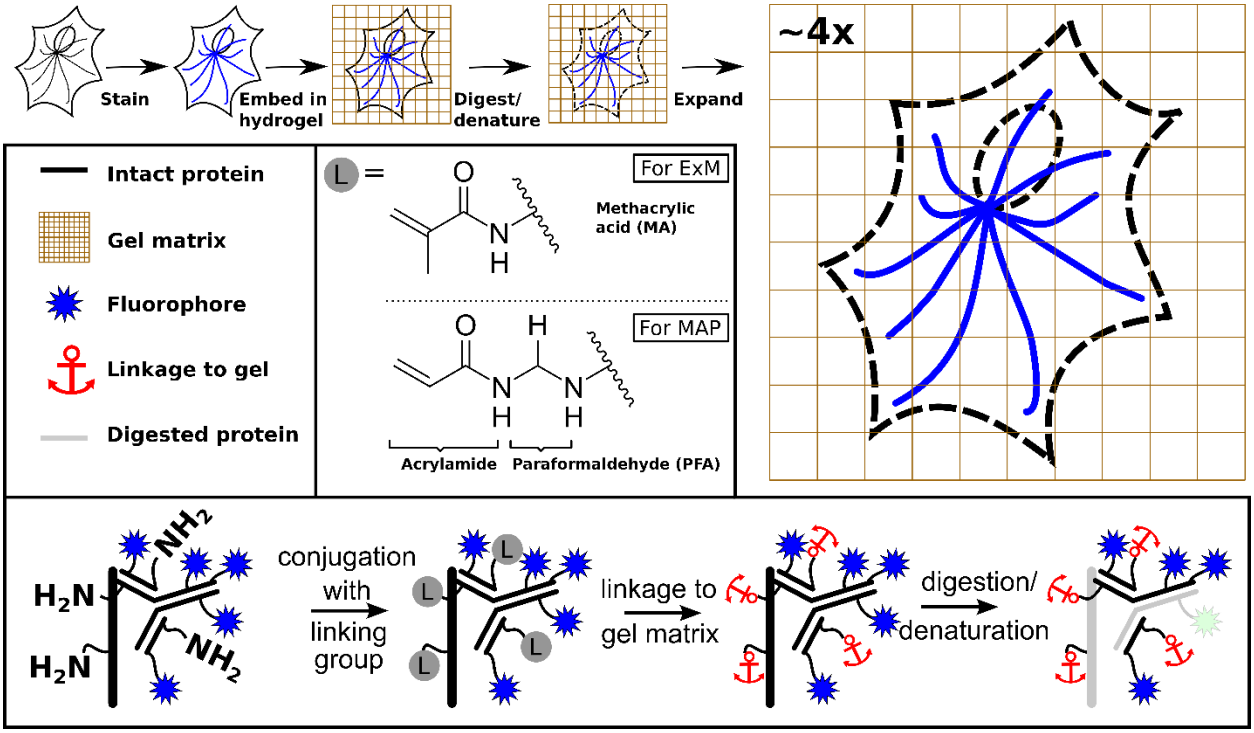

Fig. 1.10. Schematic diagram for expansion microscopy.

1.5.5 Alternatives to Light Microscopy for Nanoscale Observation

There are other powerful and well-established technologies such as electron microscopy and atomic force microscopy that allow the examination of features below the diffraction limit of light. The two main categories of electron microscopy are Transmission Electron Microscopy (TEM) and Scanning Electron Microscopy (SEM). In TEM, a beam of electrons is transmitted through the sample to a detector while in SEM, a focused beam of electrons is scanned across a small area and detects electrons emitted from the surface of the sample. Atomic Force Microscopy (AFM) uses a cantilever tip to scan the surfaces of the sample and the deflection of the tip due to forces between the tip and the sample is measured. These techniques and their derivatives can achieve much higher spatial resolution than super-resolution methods. For example, cryo-TEM with single particle averaging is used for structural determination at the few

angstrom level. However, these techniques, while powerful, may be limited to surface probing (SEM or AFM) or very thin samples (TEM).

1.5.6 Challenges of Super-resolution Methods

While super-resolution methods are effective in probing below the diffraction limit, each of these methods face certain limitations. SMLM requires special fluorescent probes that can photoswitch while remaining resistant to photobleaching. Dempsey and coworkers have screened a variety of commercially available fluorescent probes and found that only Alexa Fluor 647 or its Cy5 analogues are optimal for the technique.[21] STED requires fluorescent probes that are highly resistant to photobleaching due to the high laser intensity required. Because both SMLM and STED requires high laser power, they have limited applicability for live biological system imaging due to phototoxicity. Despite their limitations, both SMLM and STED have accomplished much in probing nanoscale biology, and in some cases, proved compatible with live cell imaging.[116–118] SIM is compatible with live specimens due to the use of relatively low laser intensity, but the technique requires care and awareness for artifacts.[119] Despite being very different methods, the common limitations for all these methods are: 1) the high cost and low accessibility of the instruments for most researchers, and 2) the high requirement of technical expertise.

Expansion microscopy, on the other hand, remains accessible and cost-effective as the method is compatible with common fluorescent microscopes and the reagents are inexpensive. However, expansion microscopy is only usable for fixed samples and may be limited to specimens that are easier to digest. Since not all samples expand well, it is necessary to optimize and analyze the digestion and denaturation processes for different biological samples. The radical polymerization process for hydrogel formation also bleaches fluorophores, thereby restricting the palette of usable fluorophores. Lastly, expansion microscopy requires fluorescent probes to be covalently attached to the hydrogel.

1.6 Summary and Goals of Study

"If and to what degree fluorescence microscopy will widen the possibilities of microscopic imaging, only the future will show." – Heimstädt[6,120], 1911

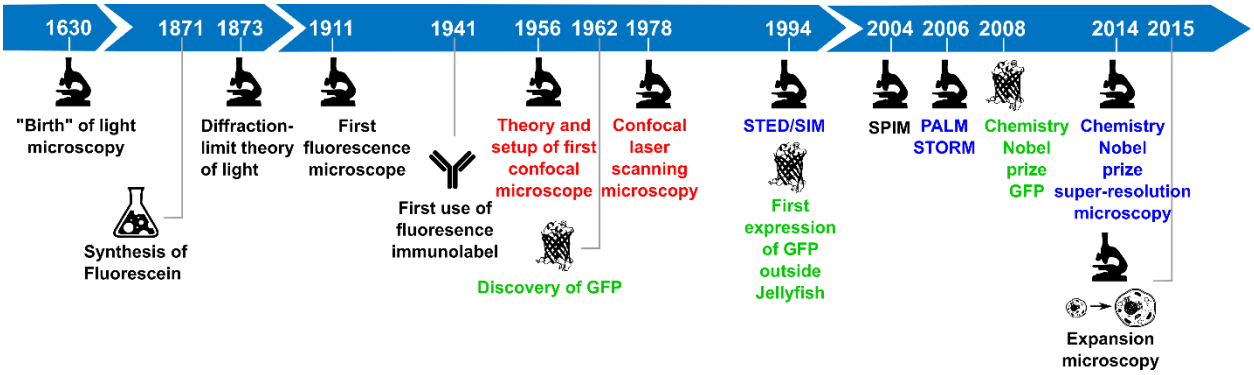

Fig. 1.11. Illustrated timeline of selected events in light and fluorescence microscopy development.

The history of light and fluorescence microscopy development have shown us that the use of an imaging method requires the interweaving of advances in different fields: optics, physics, mathematics, organic synthesis, polymer chemistry, biological chemistry and many others. It started with using rudimentary optics to observe simple phenomenon through light transmission and absorption to provide contrast. Now, we can visualize biological samples using fluorescence with a variety of methods. We can look at sub-diffraction limited organelles with super-resolution microscopes and image thick biological specimens with optical-sectioning microscopes. (**Fig. 1.11**) Chemistry has played a big part in the production and analysis of a wide palette of organic dyes available for labeling, in the optimization of thick tissue optical-clearing, and in bio-conjugating proteins to dyes or polymeric networks. The field of fluorescence imaging has advanced significantly due to advancements in optical-sectioning methods and breakthrough using super-resolution techniques. As a result, there remains room for improvement in areas such as the labeling methods in these new techniques.

While most FPs are modified from naturally occurring scaffolds, there is increasing interest to design man-made alternatives. In this study, I characterized novel photoactivatable reversible protein binders, designed from scratch by the Baker Lab, which are genetically

encodable and provided a guide for the measurement methods used (**Chapter 2**). To address the challenges of antibody penetration and thick specimen labeling, I optimized the use of commercially available fluorophores to label and penetrate thick biological sample in combination with organic-based optical clearing (**Chapter 3**). To reinvent the use of established probes in newly developed imaging techniques, I applied and optimized the application of these commercially available fluorescent probes to expanded specimens (**Chapter 3**). And finally, I included a detailed protocol and a discussion of some future directions for the method described in Chapter 3 (**Chapter 4**).

CHAPTER 2. PHOTOPHYSICAL PROPERTIES OF NOVEL FLUORESCENCE-ACTIVATING PROTEIN

2.1 Preface

This chapter is about a side collaboration project that I was involved in after facing immense challenges in fluorophore design and synthesis for SMLM. On hindsight, it was great that I was able to transfer and develop the skill that I learned, through characterizing some of my own synthesized organic fluorophores, into this project. I worked in collaboration with Dr. Jiayi Dou and Professor David Baker's lab on their purposefully designed genetically encoded protein binders. Dr. Jiayi Dou and Dr. Anastassia Vorobieva first sought out to design β-barrels from scratch. They then adopted the designing principles into designing a functional β-barrel that binds to a non-fluorescent small molecule DFHBI (3,5-difluoro-4-hydroxybenzylidene imidazolinone), which fluoresces upon binding. My contributions were focused on the photophysical measurements of these mini fluorescence-activating proteins (mFAPs) in their bound state and this chapter summarized my efforts in this project. I am glad that I was once a part of this exciting protein design project with Dr. Jiayi Dou. Although I faced new challenges in the measurements that many classic organic fluorophores do not pose, I learned a lot in the process and I hope this chapter will be a simple and general starting guide to such measurements in the future.

Some of the following material in this chapter is adapted and edited with permission from:

Jiayi Dou†; Anastassia A. Vorobieva†; William Sheffler; Lindsey A. Doyle; Hahnbeom Park; Matthew J. Bick; Binchem Mao; Glenna W. Foight; **Min Yen Lee**; Lauren A. Gagnon; Lauren Carter; Banumathi Sankaran; Sergey Ovchinnikov; Enrique Marcos; Po-Ssu Huang; Joshua C. Vaughan; Barry L. Stoddard; David Baker; "De novo design of a fluorescence-activating β-barrel", *Nature* **561**, 485 (2018). Copyright 2018 Nature Publishing Group.

† These authors contributed equally to the work.

2.2 Abstract

Fluorophores are molecules that can emit radiation of a longer wavelength upon absorption of light at one wavelength, and the excitation and emission processes utilize the same spin multiplicity (e.g. singlet to singlet). (**Fig. 1.1**) The resulting emitted light is red-shifted with respect to the excitation light due to the energy loss through non-radiative vibration relaxation (Stokes shift). Many of the photophysical properties depend on the molecule's chemical structure. (**Chapter 1.3.2**) For example, the LUMO (Lowest Unoccupied Molecular Orbital) and HOMO (Highest Occupied Molecular Orbital) gap of a more conjugated fluorescent molecule is smaller, thus resulting in the absorbance of lower energy light. The extinction coefficient (molar absorptivity constant) is a measure of how strongly the fluorophore absorbs light as a function of wavelength and the value can be determined by the relationship between absorbance and concentration in solution (commonly known as Beer's Law). Quantum yield is the efficiency of photon emission and mathematically defined by the ratio of the number of photons emitted to the number of photons absorbed, i.e. $\Phi = \frac{\text{no. of emitted photons}}{\text{no.of absorbed photons}}$. The product of the extinction coefficient and quantum yield then provides an indication of the brightness of a fluorophore. For example, fluorescein[121] has a reported quantum yield of 0.93 and a reported extinction coefficient of 76, 900 $M^{-1}cm^{-1}$, which gives a brightness of 71, 517 $M^{-1}cm^{-1}$. Here I present a method to measure these photophysical properties of fluorescent reversible protein binders.

2.3 Introduction

2.3.1 Green Fluorescent Protein (GFP)

Fluorescent proteins are genetically encoded fluorophores. (**Chapter 1.3.4**) Being a protein, their average physical size is much larger than typical synthetic organic fluorophores. However, the chromophore that results in fluorescence constitutes only a few amino acids. For example, in GFP, the formation of the chromophore is only possible through the proper folding and maturation of the protein. (**Fig. 2.1**) Once formed, the protein typically remains fluorescent until photobleaching occurs.

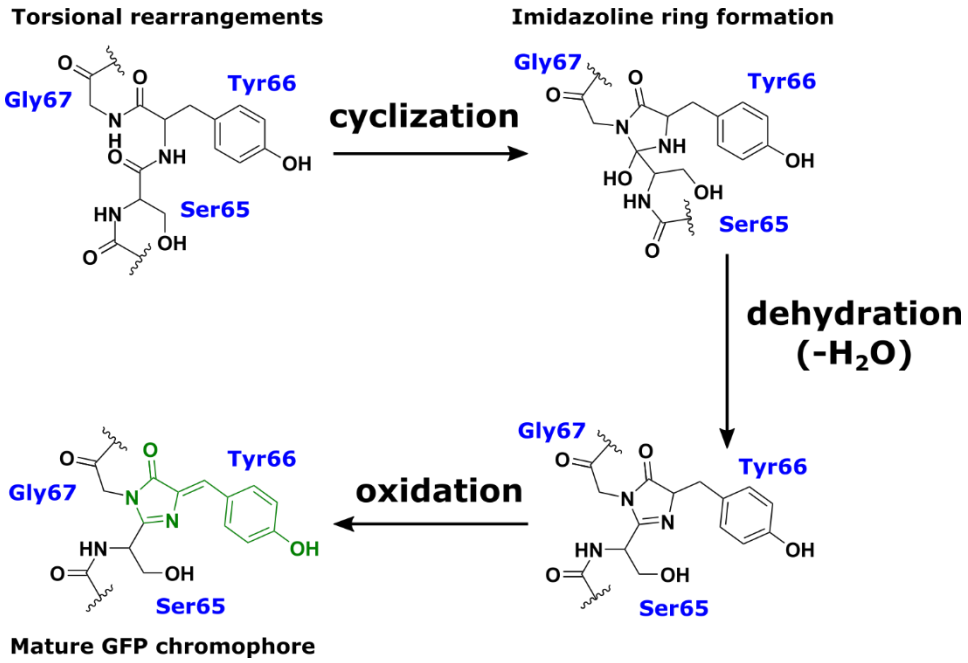

Fig. 2.1. Schematic of GFP chromophore maturation.

This schematic only showed one proposed reaction pathway towards the maturation of the Green Fluorescent Protein (GFP) chromophore (green).

2.3.2 Fluorescent Turn-on Probes and Proteins

Fluorescent turn-on probes can increase in fluorescence from a low-level fluorescence through specific chemical/light-induced reactions or interactive/binding processes. There have been many examples of such probes such as thiol-sensitive probes,[122–124] fluorescent molecular rotors for measuring cell viscosity,[125] and photoactivatable caged fluorophores. [126,127]

In 2011, Paige *et al.* designed RNA aptamers that bind non-fluorescent GFP chromophore-like small molecules.[128] The RNA-chromophore complex, called *Spinach*, can be imaged in live cells and is able to generate fluorescence brightness comparable to fluorescent proteins. They used a variety of small molecules, such as 3,5-difluoro-4-hydroxybenzylidene imidazolinone (DFHBI), to give a range of colors in the visible spectrum. In our case, instead of an RNA aptamer, fluorescence is activated upon binding of the non-fluorescent small molecule DFHBI to the newly designed β-barrel mFAP protein. (**Fig. 2.2**) DFHBI is non-fluorescent in solution due to non-

radiative processes resulting from the free rotation of the bond. (**Fig. 2.2b**) The binding of DFHBI into the mFAP1 protein forces the molecule into a planar form. (**Fig. 2.2c**) When the bounded DFHBI is excited by light, the rigidity causes the excited molecule to release the energy in the form of fluorescence emission instead. Compared to GFP, this newly designed protein is smaller (**Fig. 2.2a**) and the bound chromophore is replenishable, allowing longer imaging period to gather more information from the sample.

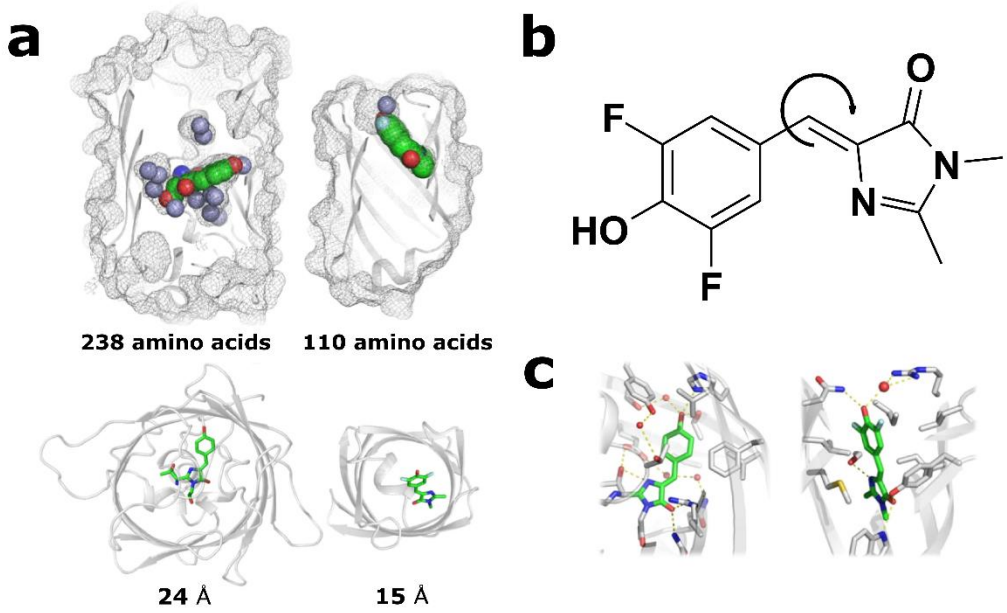

Fig. 2.2. Comparison of GFP and mFAP1.

a) Surface mesh and ribbon representations of structures of GFP (left, PDB ID: 1EMA) and the computationally designed mFAP1 (right) showing the locations where the chromophores (spheres), and resolved water molecules in the crystal structures (purple light spheres), are embedded in the protein. GFP has more than twice the number of residues, and a taller (top) and wider (bottom) barrel. b) Chemical structure of DFHBI with arrow indication of bond rotation or twisting. c) Chromophore interactions in GFP (left) and mFAP1 (right).

Novel fluorescence-activating proteins in the bound state can be characterized easily using a spectrophotometer or an integrating sphere. However, unlike regular fluorophores, their ability to bind the non-fluorescent small molecule reversibly (**Fig. 2.3**) can make measurements challenging and some related considerations are addressed in **Section 2.4**, depending on the type of measurement.

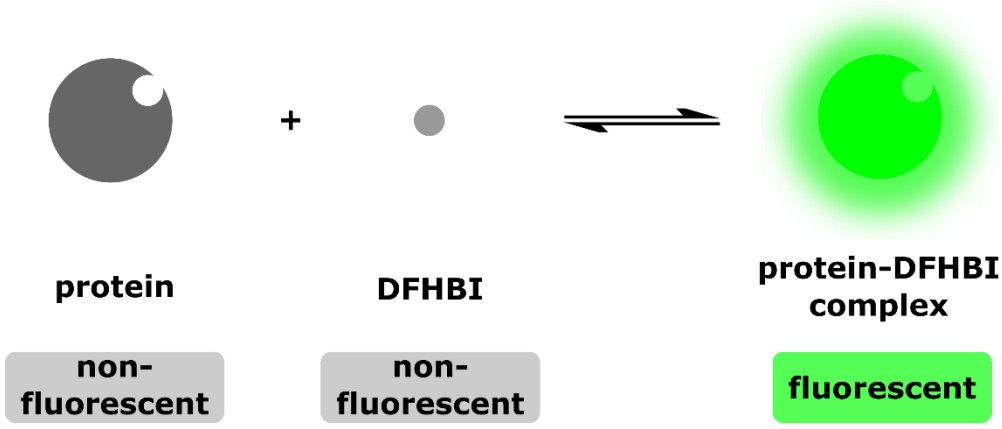

Fig. 2.3. Schematic of reversible protein binding

2.4 Method

2.4.1 General Considerations

Since the newly designed protein is a reversible binder, it is more reliable to ensure that >99% of the DFHBI molecules are bound through the addition of excess protein. This is so that the concentration of the non-fluorescent DFHBI is equivalent to the concentration of the fluorescent protein-DFHBI complex. Knowing the binding affinity (K_d) of the protein to DFHBI is highly beneficial in determining the concentration of the protein required to obtain a certain concentration of the protein-DFHBI complex. Other considerations for the measurement include the solubility of the protein. Fortunately, the solubility of the newly designed mFAP proteins are sufficient to drive the system towards the formation of the protein-DFHBI complex without causing precipitation, enabling data collection in the UV-Vis spectrophotometer using a quartz cuvette with 1 cm path length.

2.4.2 Absorbance Spectra

Absorbance spectra were measured using a Thermo Scientific BioMate 3S UV-vis spectrophotometer (1 nm interval, 800 nm/min).

To ensure accurate determination of the absorbance spectra, fluorophore solutions of concentrations that give peak absorbance that is less than 1 were prepared. A blank sample,

which was a cuvette containing the solvent that the fluorophores were dissolved in, was also prepared. The fluorophore solutions were then scanned after evaluating the blank sample.

2.4.3 Extinction Coefficients

2.4.3.1 General Considerations for Extinction Coefficient Measurements

Knowing the exact DFHBI concentration is important in accurately determining the extinction coefficient. Thus, volumetric flasks that are precise instruments to make stock solution of known concentrations were used.

There are two ways of obtaining the extinction coefficient as described below, for both uncomplexed DFHBI and the dye-protein complexes. For the uncomplexed small molecule, absorbances of varying concentrations were plotted and fitted with a line to determine the averaged extinction coefficient at a specific peak absorbance wavelength. For the dye-protein complexes, a single concentration was used to determine the peak extinction coefficient as the reversibility of binding made it difficult to create exact concentrations of the dye-protein complex. In most cases when exact concentrations of solutions can be easily made, it is recommended to use the former rather than the latter method.

2.4.3.2 Uncomplexed DFHBI

10 mg DFHBI solids were weighed out and dissolved in PBS (pH 7.4) using a 100 mL volumetric flask to make a stock solution of 10 mg/mL (~396 µM). This stock solution was then further diluted to make several stock solutions of concentrations ranging from 1-14 µM. After preparation of the solutions, the absorbance spectra of these solutions were measured using the spectrophotometer. The peak absorbance of each solution was plotted with respect to their concentration and fitted to a line whose slope, when divided by path length 1 cm, was the reported extinction coefficient.

2.4.3.3 Dye-protein Complexes

A solution was prepared containing 1 µM DFHBI and 10 µM of the β-barrel proteins mFAP1 or mFAP2 in PBS (pH 7.4) and allowed to equilibrate for at least 30 min, producing ~1 µM of mFAP1-DFHBI or mFAP2-DFHBI. The absorbance was measured for each solution, and the extinction coefficients were calculated using Beer's Law

$$A=\varepsilon bc$$

where A is peak absorbance, ε is extinction coefficient, b is path length (1 cm), and c is concentration (1 µM).

2.4.4 Fluorescence Spectra

A Perkin-Elmer LS-B Luminescence Spectrophotometer was used for obtaining the fluorescence spectra of the protein complexes and known standards (10 nm bandwidth, 1 nm interval, 100 nm/min).

To ensure accurate measurement of the fluorescence excitation and emission profile, solutions are prepared to have concentrations that give peak absorbance that was less than 1. The luminescence was then measured for each solution using the spectrophotometer. A blank sample (cuvette containing the solvent that the fluorophores were dissolved in), was also measured to enable subtraction of background.

In order to scan the excitation or emission spectra, one must excite the sample with an appropriate wavelength. The excitation wavelength used for obtaining the emission spectrum is 440 nm, a wavelength bluer than the peak of the excitation spectrum. The excitation wavelength used for obtaining the excitation spectrum is 520 nm, a wavelength redder than the peak of the emission spectrum.

2.4.5 Fluorescence Quantum Yield

2.4.5.1 General Considerations for Quantum Yield Measurements

First, to minimize reabsorption effects and inaccuracies in quantum yield measurements, the absorbance of the samples used for fluorescence quantum yield measurements should be less than 0.1. Reabsorption typically occurs at high concentration when the molecules are close enough to reabsorb the emitted photon at the region of absorbance and emission spectral overlap. Second, it is optimal to use an excitation wavelength that only the protein-DFHBI complex absorbs and to determine whether any other species fluoresce in the same region as the complex. Therefore, it is helpful to check for overlaps in the absorbance and fluorescence spectra for all three species: DFHBI, protein and protein-complexes. Third, it is beneficial that the binding affinity of the protein binder is high enough to ensure that the protein mostly stay bound to minimize any possible fluctuations in the measurements, and the solubility of the protein is high enough to drive the system towards the formation of the complex without causing precipitation, enabling data collection in the UV-Vis spectrophotometer using a quartz cuvette with 1 cm path length.

There are two types of quantum yield measurements: relative and absolute. Relative quantum yield measurements are determined from comparing the fluorescence emission intensity of the unknown sample to that of a standard sample. Absolute quantum yield measurements are determined from the collection of all the fluorescence emitted by the unknown sample using an integrating sphere. While the setup for absolute quantum yield is ideal, the ability to measure relative quantum yield is useful as the quantifications can be done using common spectrophotometer instruments. In this project, both absolute and relative quantum yield were measured, and both values helped corroborate each other.

For both relative and absolute quantum yield measurements, it is best to choose a known standard, which has similar excitation and emission properties as the unknown sample so that the same excitation wavelength can be used for both the standard and the new sample. For relative quantum yield, a known standard is necessary because the quantification of the unknown is based on the emission of a known standard. For absolute quantum yield, a known standard

can act as a control to evaluate the accuracy of the commercial integrating sphere quantum yield setup. Information on other considerations, such as oxygen sensitivity, and ways to troubleshoot can be found in the protocol paper published by Würth and coworkers.[129]

2.4.5.2 Relative Quantum Yield

The same spectrophotometer and settings in **Section 2.4.4** were used for obtaining the fluorescence spectra and the calculation of relative quantum yield.

The fluorescence emission spectra of complexes mFAP1-DFHBI and mFAP2-DFHBI (in PBS, pH 7.4) and reference dye Acridine Yellow G (in methanol) were measured. The quantum yield was calculated using the equation[129]

$$\Phi_c = \Phi_r \times \frac{1-10^{-A_r(\lambda_{ex})}}{1-10^{-A_c(\lambda_{ex})}} \times \frac{\int F_c(\lambda)d\lambda}{\int F_r(\lambda)d\lambda} \times \frac{n_c^2}{n_r^2}$$

where Φ is quantum yield, $A(\lambda_{ex})$ is absorbance at the excitation wavelength λ_{ex} (λ_{ex}=440nm), F is measured fluorescence emission, n is refractive index of the solution (1.335 for PBS and 1.3284 for methanol), and the subscripts 'c' and 'r' refer to the mFAP1-DFHBI or mFAP2-DFHBI complexes and the reference dye, respectively. A reference quantum yield value Φ_r=0.57 was used for Acridine Yellow G (in methanol). [130]

2.4.5.3 Absolute Quantum Yield

A Hamamatsu C9920-12 integrating sphere instrument was used for absolute quantum yield measurements (6 nm excitation bandwidth, 1 nm interval).

Absolute quantum yields were measured for solutions of 1 µM DFHBI and 10 µM of mFAP1 or mFAP2 in PBS (pH 7.4) that were allowed to equilibrate for at least 30 min, producing ~1 µM of mFAP1-DFHBI or mFAP2-DFHBI. Samples were excited at 440 nm and absolute quantum yields were calculated according to the equation

$$\Phi_c = \frac{f_{em}}{f_{abs}}$$

where f_{em} is the emitted photon flux and f_{abs} is the absorbed photon flux. A similar procedure was used to measure absolute quantum yields of two control samples (Acridine Yellow G and fluorescein) which agreed well with literature values. [121,130]

2.5 Results and Discussion

Using the methods described, the absorbance and fluorescence spectra were obtained (**Fig. 2.4-2.7**). Upon binding of DFHBI to either the mFAP proteins, the absorbance peak was red-shifted by ~50 nm from 418 nm to ~470-490 nm. (**Fig. 2.4**)

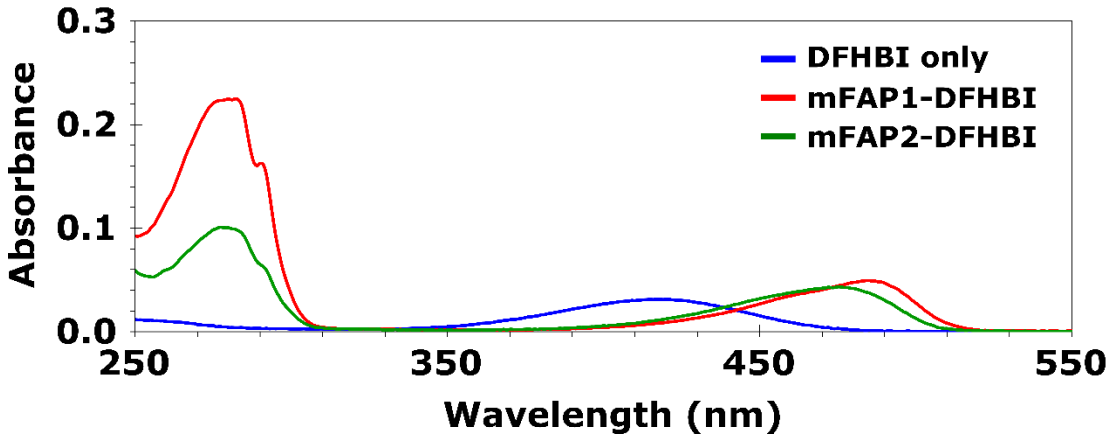

Fig. 2.4. Absorbance spectrum of DFHBI, mFAP1-DFHBI complex and mFAP2-DFHBI complex.

The extinction coefficient of the (unbound) small molecule DFHBI at 418 nm was determined from the slope of a well-correlated linear plot of absorbance against concentration (**Fig. 2.5**). The absorbance spectra and extinction coefficient of DFHBI were carefully repeated a few times for reproducibility, as the peak absorbance differed from previously published data for DFHBI[131].

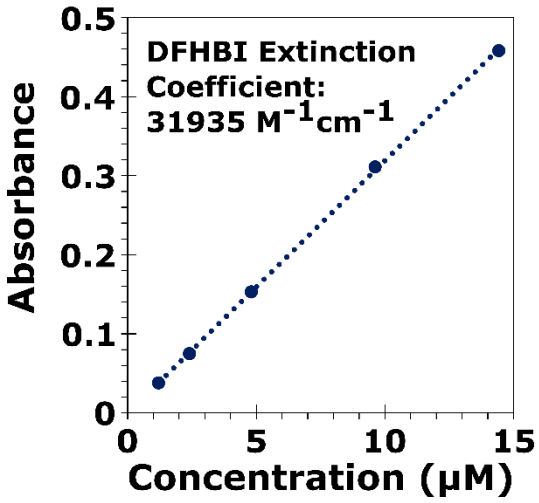

Fig. 2.5. Determination of DFHBI extinction coefficient at λ_{max}=418 nm.

The normalized fluorescence excitation and emission spectra of the protein-complexes were compared. Both the excitation and emission spectra of mFAP2-DFHBI complex were slightly more red-shifted than mFAP1-DFHBI complex. The Stokes shift for both complexes, however, was similar at ~20 nm. (**Fig. 2.6**)

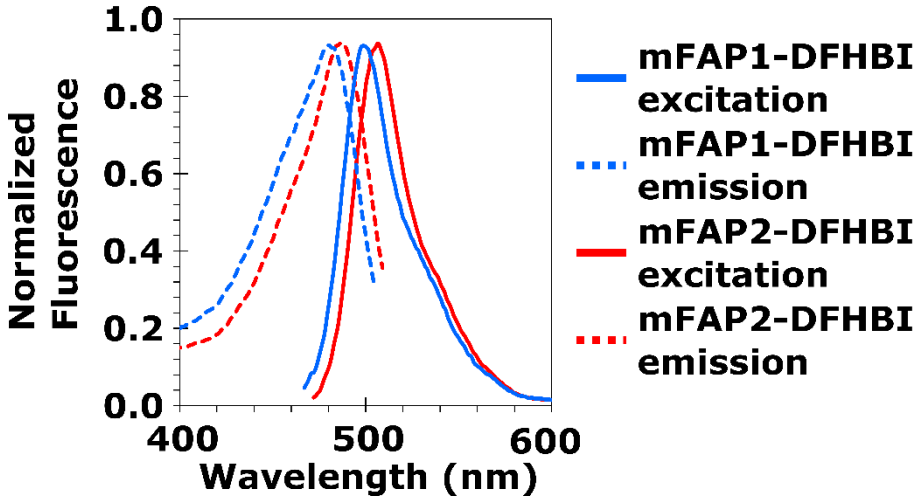

Fig. 2.6. Fluorescence spectra of both protein complexes.

Combined fluorescence excitation (dashed) and emission (solid) spectrum of mFAP1- DFHBI complex (red) and mFAP2-DFHBI complex (blue).

For each of the complexes, the absorbance and fluorescence spectra were plotted to compare their correlation. For both complexes, the absorbance and the excitation spectrum generally correlated well but the absorbance spectrum had a slightly broader profile. (**Fig. 2.7**)

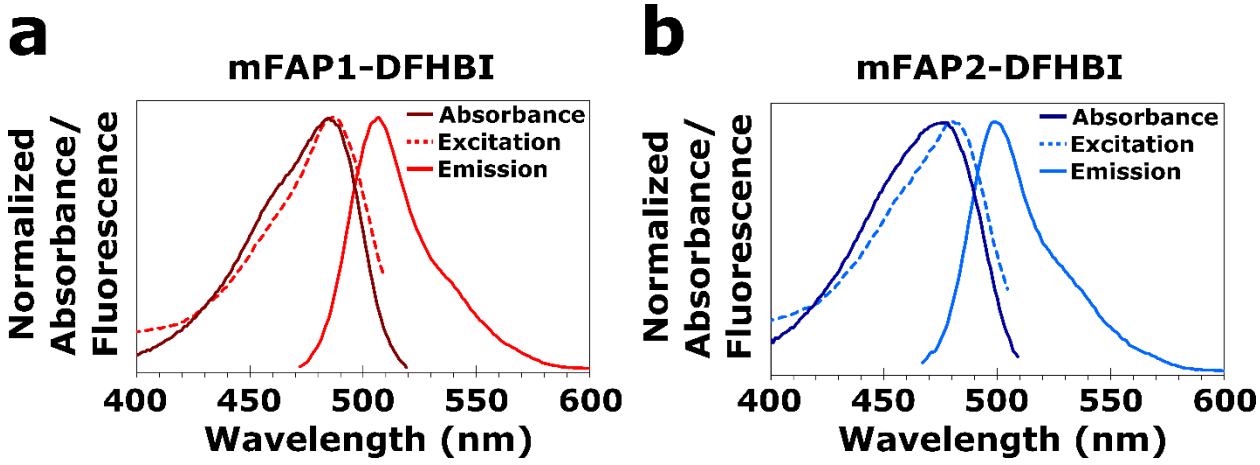

Fig. 2.7. Absorbance and Fluorescence spectra of each protein complex.

Combined absorbance and fluorescence excitation and emission spectrum of a) mFAP1-DFHBI and b) mFAP2-DFHBI.

The relative and absolute quantum yields obtained for each protein-DFHBI complex corresponded well with each other. The results of the photophysical measurements and comparisons were then summarized and published as in **Table 2.1**.

Table 2.1. Biophysical properties (absorbance or fluorescence spectra, quantum yield and binding affinity) of mFAP1 and mFAP2 in complex with DFHBI.

	λ_{abs}(nm)*	λ_{ex}(nm)*	λ_{em}(nm)*	Extinction Coefficient ($M^{-1}cm^{-1}$)	Brightness (extinction coefficient × QY)	Absolute Quantum Yield†	Relative Quantum Yield†	K_D(μM)
mFAP1-DFHBI	485	487	506	49,300	986 (34× dimmer than eGFP)	0.020	0.022	0.56 ± 0.07
mFAP2-DFHBI	476	480	500	43,200	907 (37× dimmer than eGFP)	0.021	0.021	0.18 ± 0.05
DFHBI	418	-	-	31,935	-	0.001	0.0007‡	
eGFP§		488	507	56,000	33,600		0.6	
Y-FAST:HBR‖	467		527	44,000	3,960		0.090	0.62 ± 0.05

Mean values from three biological replicates were used for the nonlinear regression to determine the K_d . The error estimates are the standard deviation from the fitting calculation. *λ_{abs} is peak absorbance wavelength, λ_{ex} is peak excitation wavelength and λ_{em} is peak emission wavelength. † Absolute quantum yield is measured with an integrating sphere; relative quantum yield is measured using acridine yellow and fluorescein as the standards. ‡Previously reported value.[128] §Taken from previously published work.[132] ‖Taken from previously published work.[133]

2.6 Conclusion

Although the brightness of this newly designed dye-protein complex is still much dimmer than wild type GFP, there are other advantages to the design. First, the designed protein is smaller and less bulky than wild-type GFP, which allows for tighter tagging of desired proteins. Second, the designed protein is a reversible binder unlike GFP, which allows for chromophore refreshing upon photobleaching, thus allowing for longer imaging times. In addition, this new design is a proof-of-principle that can potentially be further utilized and optimized for other specific uses, such as sensors or super-resolution fluorescence imaging.[134]

CHAPTER 3. FEATURE-RICH COVALENT STAINS FOR SUPER-RESOLUTION AND CLEARED-TISSUE FLUORESCENCE MICROSCOPY

3.1 Preface

Being in a microscopy lab, we frequently used antibodies to specifically target and fluorescently label biological structures. However, we often faced inconsistencies with antibodies, which are often attributed to antibody degradation or lot-to-lot variability. Additional challenges include long incubation times required for thick specimens without the use of specialized equipment. With this in mind, we aim to provide a robust and fast method of staining for Expansion Microscopy (ExM) and cleared tissue fluorescence microscopy. This chapter introduces a new alternative labeling technique that I developed and optimized along with my coworker Chenyi Mao. We refer this method as Fluorescent Labeling of Abundant Reactive Entities (FLARE); as the name suggests we target reactive chemical functional groups on amino acid residues or carbohydrates for fluorescent modification. My contribution here covers: 1) optimization of FLARE staining for expanded cell culture samples with antibodies or fluorescent proteins (**Section 3.4.1, Section 3.4.4**); 2) testing the sequence and effect of the staining procedure on expanded and unexpanded cells (**Section 3.4.4**); 3) optimization of FLARE staining for organic-solvent based cleared thick tissue (~500 µm and ~1 mm in depth) (**Section 3.4.2**); and 4) application of optimized FLARE staining on various cleared tissue including mouse intestine, mouse liver, human prostate and mouse muscle (**Section 3.4.3**). In particular, I would like to acknowledge my coworker Chenyi who has been a pleasure to work with and taught me a lot, as well as everyone on the team.

† These authors contributed equally to this work.

All material in this chapter has been reformatted to adapt to the style of this thesis.

3.2 Abstract

Fluorescence microscopy is a workhorse tool in biomedical imaging but often poses substantial challenges to practitioners in achieving bright or uniform labeling. In addition, while antibodies are effective specific labels, their reproducibility is often inconsistent, and they are difficult to use when staining thick specimens. We report the use of conventional, commercially available fluorescent dyes for rapid and intense covalent labeling of proteins and carbohydrates in super-resolution (expansion) microscopy and cleared-tissue microscopy. This approach, which we refer to as Fluorescent Labeling of Abundant Reactive Entities (FLARE), produces simple and robust stains that are modern equivalents of classic small-molecule histology stains. It efficiently reveals a wealth of key landmarks in cells and tissues under different fixation or sample processing conditions and is compatible with immunolabeling of proteins and in situ hybridization labeling of nucleic acids.

3.3 Introduction

Two of the most important developments in fluorescence microscopy over the past one to two decades are super-resolution microscopy, for imaging small features beneath the ~250 nm diffraction limit of visible light, and cleared tissue microscopy, for deep imaging of intact specimens [59,135–138]. Researchers are now able to routinely measure nanoscale molecule distributions, protein oligomerization or protein-protein interactions, and to determine the large-scale organization of biological specimens. Central to these efforts are a wide range of probes to fluorescently label the sample, with one of the most important classes being fluorescently labeled antibodies. While antibodies are powerful in their ability to specifically label specimens without need for genetic manipulation, they often suffer slow penetration in thick tissues, poor binding in specimens that have been heavily fixed or processed (e.g., formalin-fixed paraffin-embedded tissue), high cost, and inconsistent lot-to-lot reproducibility or commercial availability [37,139].

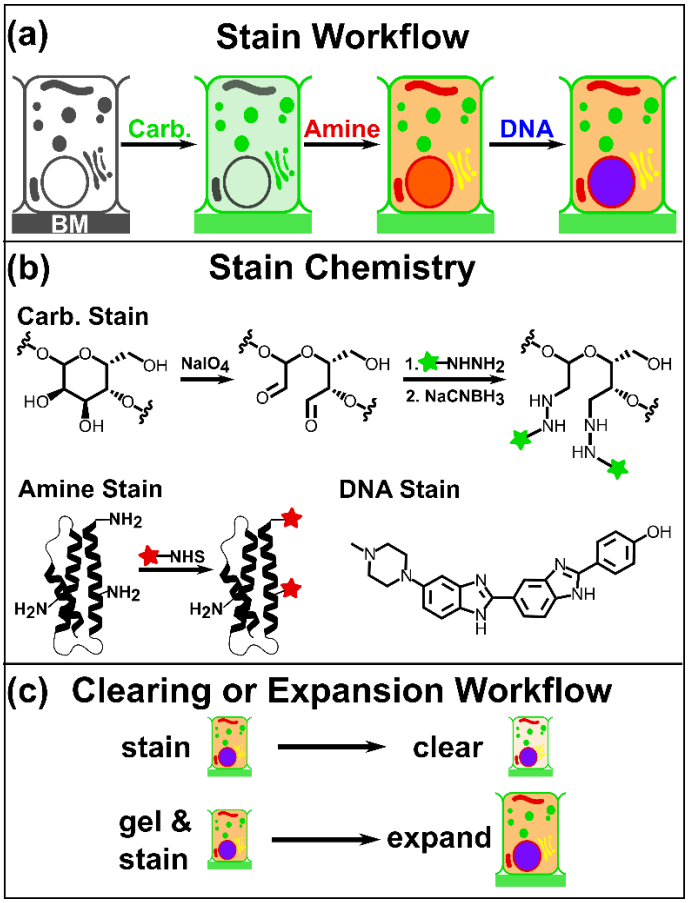

Fig. 3.1. Schematic illustration of FLARE staining of amines and carbohydrates, together with DNA staining, for super-resolution and cleared-tissue microscopy.

(a) Carbohydrates, amines, and DNA on cells or tissues are stained as the order shown. (b) Vicinal diols on carbohydrates are oxidized to aldehydes using sodium periodate, coupled to hydrazide-functionalized fluorophores (green), and then stabilized by reduction with sodium cyanoborohydride. Amines are labeled by reaction with an NHS-functionalized fluorophore (red). DNA is labeled non-covalently by incubation with a conventional DNA stain such as Hoechst or SYBR Green (blue). (c) Specimen processing workflow with respect to clearing and expansion.

Small-molecule histology stains such as H&E (hematoxylin and eosin) [140] are attractive potential alternative labels for super-resolution and cleared-tissue microscopy, but they pose several challenges [141]. First, many histology stains are affinity-based, rather than covalent, and produce uneven staining particularly for relatively thick specimens, whereas covalent labeling renders the labels compatible with a wider range of sample processing or clearing techniques. Second, nonfluorescent histology stains are poorly suited to volumetric imaging and fluorescence-based super-resolution microscopy methods. Third, classic histology stains have limited flexibility in their spectral properties whereas modern fluorescent dyes are available in

many forms across the visible and near infrared with high quantum yields and good resistance to photobleaching.

To partly address the limitations of antibodies and small-molecule histology stains, we developed simple procedures for using commercially-available small-molecule fluorophores to brightly label a wide variety of major organelles and landmark structures in cells and tissues for super-resolution microscopy and cleared-tissue microscopy. The idea is to use small molecules to covalently label abundant chemical functional groups on biological samples, instead of specific biomolecules, to reveal the general physiology of the sample. These include the use of amine-reactive fluorophores for measuring distributions of proteins and aldehyde-reactive fluorophores for measuring distributions of oxidized carbohydrates, although other abundant reactive groups (thiols, carboxylates, etc.) may also be suitable. We termed this approach Fluorescent Labeling of Abundant Reactive Entities (FLARE). While the underlying chemical reactions are well known [36,142–147], for instance when labeling purified proteins [36], specimen surfaces [148], or isolated live cells for subsequent tracking [149], the great utility of this simple labeling approach in super-resolution and cleared-tissue microscopy has not been previously recognized. For super-resolution microscopy, we used expansion microscopy (ExM), a recently developed technique that physically expands biological specimens embedded in a swellable polymer [83,98,100]. The physical expansion enables features closer than the ~250 nm diffraction limit of traditional light microscopy to be resolved in the expanded state on a conventional microscope. For cleared tissue microscopy with unexpanded specimens, we used a variant of the solvent-based tissue clearing method immunolabeling-enabled three-dimensional imaging of solvent-cleared organs (iDISCO) [150] that uses ethyl cinnamate (EC) for index matching [65].

3.4 Results

3.4.1 FLARE reveals key landmarks in hydrogel-expanded specimens.

We first tested the ability of FLARE to stain cultured human retinal pigment epithelium cells (RPE) that had been expanded five-fold using ExM. Using the labeling schematic in **Fig. 3.1**, we stained oxidized carbohydrates on the specimen with ATTO 565 hydrazide, amines with ATTO

647N NHS (*N*-hydroxysuccinimidyl) ester, and DNA (non-covalently) with SYBR Green (**Fig. 3.2, Fig. S3.1**). Mitochondria were densely labeled by the amine stain, while lysosomes and the plasma membrane were densely labeled by the carbohydrate stain, and perinuclear structures including portions of the Golgi were labeled by both amine and carbohydrate stains (**Fig. 3.2a-c, Fig. S3.1, Fig. S3.2**). The nucleus and nuclear envelope of interphase cells were clearly evident as were nuclear pores in both the amine and carbohydrate channels (**Fig. 3.2c, Fig. S3.2i-l**). In dividing cells (**Fig. 3.2d-f, Fig. S3.1**), kinetochores and centrosomes were also labeled well. Thus, the chemical stains efficiently report on many major landmark structures and components of the cell.

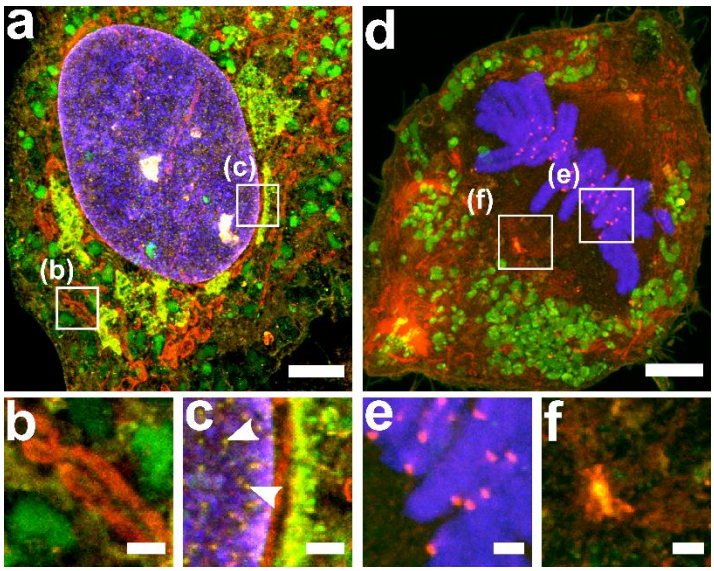

Fig. 3.2. **FLARE staining of hydrogel-expanded cultured cells.**

Confocal microscopy images of hydrogel-expanded RPE cells that have been covalently stained for amine (red) and carbohydrate (green) using FLARE along with a conventional noncovalent stain for DNA (blue). (a) Interphase cell showing various subcellular organelles including mitochondria (red), lysosomes (green), and perinuclear structures (yellow). (b-c) Zoomed-in views of boxed regions in a). Arrowheads in c) indicate nuclear pores. (d) Dividing cell showing various subcellular organelles. (e-f) Zoomed-in views of boxed region in d) showing kinetochores and centrosomes, respectively. All scale bars are in pre-expansion units. Scale bars are 3 µm (a,d), 500 nm (b-c, e-f).

FLARE can be straightforwardly combined with antibody labeling, which we used here to confirm the identities of some subcellular organelles or structures such as mitochondria, lysosomes, and the golgi apparatus (**Fig. S3.2**). However, we also realized that some features observed in the images are not easily identified, and some known structural features are difficult

to detect in the images. For instance, in dividing RPE cells, we frequently observed a swirling tuft of unknown amine-rich cytoskeletal filaments toward one end of the cell while at the same time, we were surprised that microtubules of the mitotic spindle were unlabeled (**Fig. 3.2d**). Nonetheless, results with cultured cells indicate that these relatively non-specific covalent stains together with the improved spatial resolution (~65 nm) attained using specimen expansion with confocal microscopy [83,98,100] can reveal a wealth of details but that more work will be required to better understand and possibly tune the specificity of labeling.

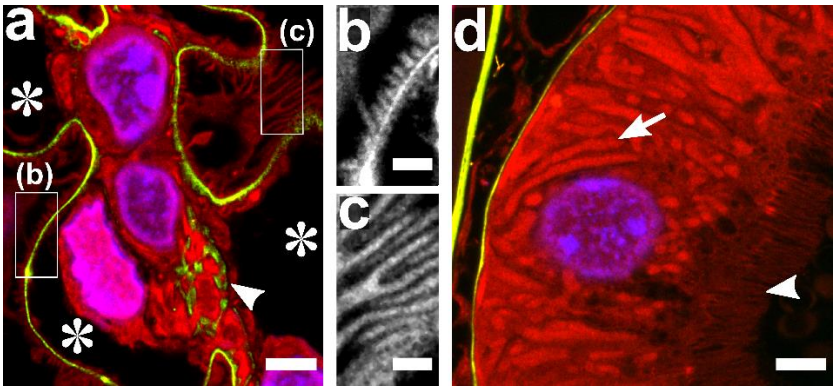

Fig. 3.3. **FLARE staining of hydrogel-expanded mouse kidney tissue.**

Confocal microscopy images of hydrogel-expanded mouse kidney that have been covalently stained for amines (red) and carbohydrates (green) using FLARE along with a conventional noncovalent stain for DNA (blue). (a) A region of a mouse kidney glomerulus in which carbohydrates are intensely labeled along the basement membrane of the capillary loops (stars) and within the mesangial matrix (arrowhead). (b-c) Zoomed-in views of amine channel for boxed regions in panel (a) showing interdigitated podocyte foot processes. (d) A region of a proximal convoluted tubule in which carbohydrates highlight tubular basement membrane and amines intensely label mitochondria (arrow) and microvilli (arrowhead). All scale bars are in pre-expansion units. Scale bars are 3 µm (a,d), 500 nm (b-c).

Beyond cultured cells, we found that FLARE also works well in hydrogel-expanded tissues, as we demonstrate using mouse kidney, a model specimen containing a diverse range of structures and cell types (**Fig. 3.3**). Within glomeruli, the filtration units of the kidney, the carbohydrate stain brightly labeled the basement membranes of the capillary loops and the mesangial matrix, while the amine stain efficiently outlined cell boundaries and other structures, including the intricate details of interdigitated podocyte epithelial cells that form a major component of the glomerular filtration barrier (**Fig. 3.3a-c, Video S3.10**). In proximal convoluted tubules of the kidney, the basement membrane was also labeled by the carbohydrate stain, and the amine stain revealed mitochondria, the nuclear envelope, and brush border microvilli (**Fig.**

3.3d). While we focus in this paper on a variation of ExM termed MAP (magnified analysis of the proteome) [100] that utilizes heat and detergent to dissociate tissue-hydrogel hybrids, rather than enzymatic digestion as in the original ExM method [98], we found that enzymatically digested mouse kidney tissue could also be covalently stained (**Fig. S3.3a-d**), indicating that the possible loss of material due to digestion was not prohibitive. Additionally, we found that FLARE is compatible with in-situ hybridization for detection of nucleic acids (**Fig. S3.3e-h**).

3.4.2 FLARE labels thick tissue samples rapidly and uniformly.

We next tested FLARE in various unexpanded specimens that were subsequently optically cleared using dehydration in a graded series of tetrahydrofuran (THF), followed by immersion in EC, a variant of the iDISCO clearing method [65,150]. The labeling protocol was approximately the same as for the labeling of tissue-hydrogel specimens with two important adjustments to help enhance the uniformity of the stains throughout the depth of the tissue. First, during both covalent labeling reactions, we dissolved dyes in a co-solvent mixture consisting of a 1:1 ratio of aqueous buffer to THF in order to increase the rate of diffusion through the specimen (**Fig. 3.4a-e, Fig. S3.4**). Second, for the amine-labeling reaction, we adjusted the pH to 6.0 to reduce the rate of the coupling reaction while also reducing the rate of hydrolysis of the ester that would render the dye unreactive [16,151]. These measures greatly improved the uniformity (**Fig. 3.4a-e**). For example, approximately uniform covalent amine-labeling of a ~500-µm-thick section of mouse kidney could be achieved in ~2 hours, whereas the same tissue section when labeled with antibodies for 6 days was only stained at a depth of <50 µm at each surface of the tissue section (**Fig. 3.4e**). We then used this procedure to stain and clear a relatively large volume of mouse kidney (~4 mm by ~3.5 mm by ~1 mm) and imaged it using a recently published open-top light sheet microscope [152] at a resolution of ~2 µm (**Fig. 3.4f-h, Fig. S3.5a-d**). We were able to observe renal tubules over long distances with characteristic segment-specific stain distributions for proximal tubules, distal tubules, loop of Henle, etc., that provide bearing on the location of the tubule within the nephron. We validated the identities of these key features in mouse kidney using covalent amine and carbohydrate labeling concurrent with a triple immunostain against

cytokeratin (CK8+18, enriched on collecting ducts), aquaporin (AQP-1, enriched on proximal tubules) and podocalyxin (PODXL, enriched on glomeruli) (**Fig. S3.6**).

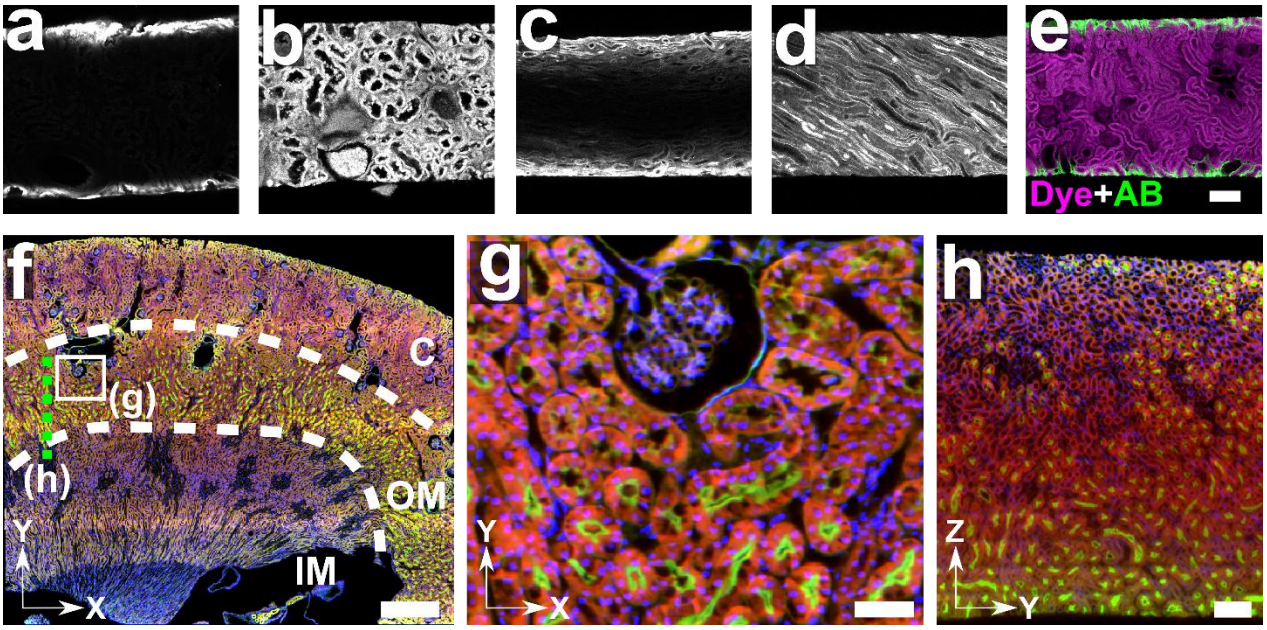

Fig. 3.4. **FLARE staining of thick, cleared tissue specimens.**

(a-e) 500 µm thick kidney sections were covalently stained, cut perpendicular to the section face, and imaged to measure stain intensity as a function of depth. Staining using an aqueous buffered solution produced uneven surface stains for (a) ATTO 647N-NHS and (c) ATTO 565-hydrazide, but labelling with an aqueous/THF co-solvent mixture greatly improved the uniformity, as shown in (b) and (d), respectively. (e) Comparison of stain uniformity for immunolabeling of collagen (AB, green) for 6 days and amine labelling (Dye, magenta) with ATTO 647N-NHS for 2 hours. (f) Open-top light sheet microscopy images of ~1 mm thick mouse kidney sections in which amines (red) and carbohydrates (green) show distinct distributions among the cortex (C), outer medulla (OM), and inner medulla (IM) regions. (g) Zoom-in view of panel (f) taken from outer medullar region which contains various tubular architectures. (h) Cross-sectional view of the optically cleared mouse kidney sections along the dashed green line in panel (f). Scale bars are 100 µm (a-e, h), 50 µm (g), 0.5 mm (f).

3.4.3 FLARE is applicable to a wide range of tissues.

Besides kidney tissue, FLARE also revealed an abundance of physiological details in a diverse range of other specimens (**Fig. 3.5, Fig. S3.5e-x**). For instance, mouse intestine exhibited clear staining of intestinal villi, crypts, sub-epithelial cells, specialized cells (goblet cells, Paneth cells), lymphatic vessels, and muscle cell boundaries; mouse liver revealed glycogen-rich hepatocytes with a strongly anticorrelated sub-cellular distribution of amine-reactive and carbohydrate-reactive domains; mouse sperm exhibited distinct developmental patterns of

carbohydrates within seminiferous tubules of the testis; and human prostate gland and connective tissue from stroma are distinctly labeled and well distinguished from each other. Even FFPE human kidney tissue was straightforwardly labeled using FLARE, a notable capability because FFPE tissue processing often leads to loss of antigenicity for immunolabeling, whereas primary amines and carbohydrates remain quite reactive. We further compared FLARE with traditional histological staining by treating consecutive 10-µm-thick mouse kidney FFPE sections to either H&E or FLARE (**Fig. S3.7**). By converting the DNA and amine channels of the FLARE-stained sections to a simulated H&E image using the procedure of Giacomelli et al. [153] we found that the FLARE and H&E tissues are qualitatively quite similar, although the standard fluorescence display of the DNA, amine, and carbohydrate signals of the FLARE data provided much greater detail (**Fig. S3.7**).

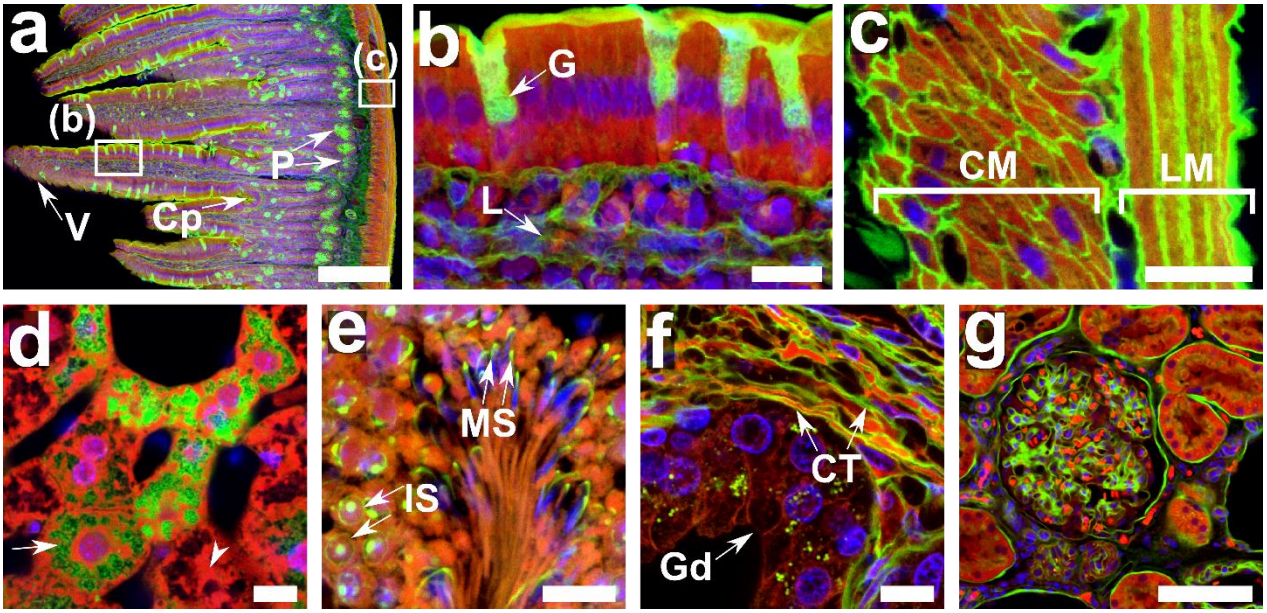

Fig. 3.5. **FLARE staining of a variety of cleared tissue specimens.**

Fluorescence microscopy images of optically cleared tissue specimens that were covalently stained for amines (red) and oxidized carbohydrates (green) along with a conventional noncovalent stain for DNA (blue). (a-c) mouse intestine, in which villi (V), crypt (Cp), Paneth cells (P), goblet cells (G), lymphatic vessels (L), circular muscle (CM), and longitudinal muscle (LM) layers are evident in the carbohydrate channel. (d) mouse liver where carbohydrate-rich and amine-rich regions are indicated with arrow and arrowhead, respectively. (e) mouse testis, in which immature spermatocytes (IS) and mature spermatocytes (MS) are evident and contain distinct carbohydrate distributions in the carbohydrate channel. (f) human prostate, where gland (Gd) and connective tissue (CT) from stroma are distinctly labeled. (g) formalin-fixed, paraffin-embedded human kidney. Scale bars are 100 µm (a, g), 10 µm (b-f).

3.4.4 Order of processing for FLARE is flexible.

While there is considerable flexibility in the order of processing for FLARE in both expanded and non-expanded samples, some care is required (see **Methods** and **Supplementary Table S3.1**). First, the sodium periodate oxidation reaction used in carbohydrate labeling bleaches fluorophores already on the sample and tended to produce cracks in the expanded kidney tissue specimen if the oxidation step was done before sample gelation. As a result, we performed carbohydrate labeling before amine labeling, in general, and after expansion for kidney specimens (**Fig. 3.3, Fig. 3.4f-h, Fig. S3.1, Fig. S3.5a-d, Fig. S3.6** and **Fig. S3.7e-f**). Second, although covalent modification of the sample via FLARE has the potential to perturb epitope antigenicity necessary for antibody binding, we found that antibody labeling generally works quite well after FLARE. Out of a panel of 16 antibodies, 14 antibodies were able to effectively stain mouse kidney tissue (**Fig. S3.8**) or RPE cells (**Fig. S3.9**) after covalent labeling of carbohydrates and amines. Among the two impacted antibody stains, we found that the carbohydrate staining step partially blocked antibody staining of agrin on mouse kidney and fully blocked the antibody staining GM130 on RPE cells, but that both of these antibodies bound their targets well after covalent labeling of amines. This may indicate that we only labeled a small fraction of available amines, such that most amines on epitopes are unmodified, but that carbohydrate oxidation and/or fluorophore labeling may be more complete. We found that it was straightforward to change the order of labeling in cases like anti-GM130 (**Fig. S3.2m-q**) in order to immunolabel prior to covalent staining, although it is possible that a milder oxidation step may help better preserve antigenicity.

3.5 Discussion and Conclusion

One might initially expect that the indiscriminate labeling of primary amines and carbohydrates in cells and tissues would yield little contrast because of the high abundance of these species. However, the resulting feature-rich labeling we obtained likely results from an interplay between the uneven distribution of these groups throughout the specimen [154,155], the reactivity of those groups (which can vary depending on the amine pKa [156] or other local factors), and earlier reactions with the specimen, such as may have occurred during aldehyde fixation and

would consume some available reactive groups. Some known structures that were difficult to detect in expanded RPE cells, such as the endoplasmic reticulum or kinetochore fibers of the mitotic spindle, likely result from the above considerations and from the possibility that relatively weak labeling of these structures may be difficult to detect clearly due to the presence of many other brightly labeled structures within the specimen.

Here we have shown that simple amine-reactive and carbohydrate-reactive covalent stains, together with established DNA-stains, are versatile tools in super-resolution fluorescence microscopy and cleared-tissue fluorescence microscopy. Although we recently published a preliminary application of the use of amine-reactive fluorophores for rapid (<5 min) surface labeling of unexpanded and uncleared clinical specimens for rapid diagnosis [157,158], the versatility of FLARE for super-resolution microscopy and cleared-tissue microscopy was not explored. In addition, FLARE can be easily combined with different staining modalities (e.g., fluorescence in situ hybridization labeling of nucleic acids and immunolabeling of proteins (**Fig. S3.3e-h, Fig. S3.8-9**)), is compatible with a large selection of excellent fluorophores across the visible and near infrared, and reveals abundant details in a wide range of samples and sample processing methods. While the contrast provided by these non-specific stains allows researchers to identify a range of features and key landmarks, the highlighted features vary between types of specimens and the utility of the stains are therefore somewhat dependent on the specific application. In the future, we look toward expanding the palette of covalent probes for FLARE by developing stains that target a wider range of chemical groups and by developing probes that target more specific subsets of proteins or carbohydrates. FLARE, together with newly developed custom probes against lipids[159] or other groups, will provide a versatile toolset that complements molecule specific probes such as antibodies and FISH probes.

3.6 Materials and Methods

Chemicals and reagents

Primary antibodies were purchased as follows: goat anti-podocalyxin (R&D Systems, Inc., AF1556), rabbit anti-collagen IV (Abcam, ab6586), mouse anti-alpha smooth muscle actin

(BioLegend, Inc., 904601), rabbit anti-aquaporin 1 (Abcam, ab15080), guinea pig anti-cytokeratin 8+18 (Abcam, ab194130), mouse anti-agrin (DSHB, Inc., 6D2), rabbit anti-podocin (Sigma Aldrich, P0372), rabbit anti-TOMM20 (Santa Cruz Biotechnology, sc-11415), rabbit anti-LAMP-1 (Abcam, 24170), anti-GM130 (BD Biosciences, 610822), rabbit anti-GFP conjugated with Alexa Fluor 488 (Thermo Fisher Scientific, A-21311), rabbit anti-GFP conjugated with Alexa Fluor 647 (Thermo Fisher Scientific, A-31852), rabbit anti-H3K27ac (Active Motif, 39133), rabbit anti-H3K4me3 (Active Motif, 39159), rat anti-alpha tubulin (Invitrogen, MA1-80017), goat anti-nogo N-18 (Santa Cruz Biotechnology, sc-11027), rabbit anti-PMP70 (Thermo Fisher Scientific, PA1-650), anti-vimentin V9 (Invitrogen, 18-0052). Unconjugated secondary antibodies were purchased as follows: donkey anti-goat (Jackson Immunoresearch, 705-005-151), donkey anti-rabbit (Jackson Immunoresearch, 712-545-150), donkey anti-mouse (Jackson Immunoresearch, 715-005-151), donkey anti-guinea pig (Jackson Immunoresearch, 706-001-003), donkey anti-rat (Jackson Immunoresearch, 712-005-153). Donkey anti-rabbit conjugated with Alexa Fluor 488 (711-545-152) and donkey anti-mouse conjugated with Alexa Fluor 488 (715-545-150) was purchased from Jackson Immunoresearch. Fluorescent dyes were purchased as follows: Alexa Fluor 750 NHS ester (Thermo Fisher Scientific, A20011), Alexa Fluor 546 NHS ester (Thermo Fisher Scientific, A2002), ATTO 647N NHS ester (Sigma-Aldrich, 18373-1MG-F), ATTO 565 NHS ester (Sigma-Aldrich, 72464-1MG-F), ATTO 565 hydrazide (ATTO-TEC GmbH, AD 565-121), AFdye 405 NHS ester (Fluoroprobes, 1061-1). Hoechst 33258 (Sigma-Aldrich, B2883-25MG), SYBR Green I (Invitrogen, S7563). 50% glutaraldehyde (GA, 16320) was purchased from Electron Microscopy Sciences. Reagents for polymerization were purchased as follows: 32% paraformaldehyde (PFA) aqueous solution (Electron Microscopy Sciences, RT15714), 40% acrylamide (AA) aqueous solution (Bio-Rad Laboratories, 1610140), 2% Bis-acrylamide (BA) aqueous solution (Bio-Rad Laboratories, 14101420), 97% sodium acrylate (SA) powder (Sigma-Aldrich, 408220), VA-044 initiator (Thermo Fisher Scientific, NC0471397), ammonium persulfate (APS, Thermo Fisher Scientific, 17874), Tetramethylethylenediamine (TEMED, Thermo Fisher Scientific, 17919), 97% 4-hydroxy-2,2,6,6-tetramethylpiperadin-1-oxyl (TEMPO, Sigma-Aldrich, 176141). Reagents for enzymatic digestion were purchased as follows: proteinase K (Thermo Fisher Scientific, EO0491), 10× Tris-acetate-EDTA (TAE buffer, Fisher Bioreagents, BP2434-4), 10× Phosphate Buffered Saline (PBS buffer,

Fisher Bioreagents, BP399-1), guanidine hydrochloride (Sigma-Aldrich, G3272), collagenase (F type blend, Sigma Aldrich, C7926), Hank's Balanced Salt Solution (HBSS, 1×, Corning). Tris Base (BP-152), calcium chloride ($CaCl_2$, S25223), sodium chloride (NaCl, S271500), d-glucose (D16-1) and sodium acetate (NaOAc, BP333-500) powders were purchased from Thermo Fisher Scientific. Sodium dodecyl sulfate (SDS, L3771), sodium periodate ($NaIO_4$, 311448), sodium cyanoborohydride ($NaCNBH_3$, 156159), ethyl cinnamate (EC, 112372), methacrylic acid NHS (MA-NHS, 730300), 4-(1,1,3,3-tetramethylbutyl)phenyl-polyethylene glycol (Triton X-100, X100), 4-morpholineethanesulfonic acid (MES, M3671), Piperazine-1,4-bis(2-ethanesulfonic acid) disodium salt (PIPES disodium salt, P3768), ethylene glycol-bis(2-aminoethylether)-N,N,N',N'-tetraacetic acid (EGTA, E4378), magnesium chloride ($MgCl_2$, M8266), sodium borohydride ($NaBH_4$, 213462), sodium azide (NaN_3, S2002) and poly-L-lysine (P8920), trolox (238813), glucose oxidase (G2133-50KU), catalase (C100) were purchased from Sigma-Aldrich. Sodium bicarbonate ($NaHCO_3$, 470302) was purchased from VWR Scientific. Bovine serum albumin (BSA, BAS-50) was purchased from Rockland Immunochemicals Inc. Reagents for DNA fluorescence in situ hybridization (FISH) were purchased as follows: Formamide (Fisher Chemical, F84-1), 20× Saline Sodium Citrate (SSC Buffer, Sigma-Aldrich, S6639), 50% OmniPur Dextran Sulfate (EMD Millipore, 3730), Tween 20 (Sigma-Aldrich, P9416). Major Satellite and ATTO 647N conjugated reporter oligonucleotides were obtained from IDT.

Cell Culture

H-tert Retinal Pigment Epithelium Cells (RPE) were obtained and authenticated from ATCC and were used without further authentication. RPE cells were tested negative for mycoplasma with 4',6-diaminodino-2-phenylindole dihydrochloride. RPE cells were cultured in Dulbecco's Modified Eagle Medium (DMEM, Gibco, 11995-065) supplemented with 100 Units/mL Penicillin Streptomycin (Gibco, 15140-122), 1% non-essential amino acids (NEAA, Gibco, 11140-050) and 10% fetal bovine serum (FBS, Gibco, 26140079), and grown to ~70-90% confluency. The cells were then trypsinized with 0.25% Trypsin-EDTA (Gibco, 25200056) and seeded (~50,000 cells/well) on #1.5 round coverslip (~12 mm) in 24-well culture plates. 24 hours later, the cells were fixed with either 3.2% PFA and 0.1% GA or 4% PFA in PEM buffer (100 mM aqueous PIPES,

1 mM EGTA, 1 mM $MgCl_2$, pH 7) for 10 minutes at room temperature. In some cases, cells were extracted with 0.5% Triton X-100 in PEM buffer for 30 secs before fixation with 3.2% PFA and 0.1% GA in PEM buffer (see **Table S3.1** for details). Fixed cells were stored in 1× Phosphate Buffer Saline with 3mM sodium azide (1× PBS azide) at 4°C prior to use.

Transfection of cultured cells

Trypsinized RPE cultured cells (~1 to 2 x 106 cells) were pelleted down by centrifugation (150 g for 5 min) and resuspended in nucleofection solution (Lonza Kit V, VACA-1003) with 2 µg plasmid mEmerald-Golgi-7, and electroporated following manufacturer's (Lonza Amaxa Nucleofector I/II) X-001 pulse program. mEmerald-Golgi-7 was a gift from Michael Davidson's Lab (Addgene plasmid #54108; http://n2t.net/addgene:54108; RRID:Addgene_54108). pAc-GFPC1-Sec61β was a gift from Tom Rapoport (Addgene plasmid #15108; http://n2t.net/addgene:15108; RRID:Addgene_15108). Transformed cells (transfection efficiency ~70%) were then seeded (~80,000 cells/well) on #1.5 round coverslips (~12 mm) in 24-well culture plates and allowed to recover for 24 hours before fixation with 3.2% PFA and 0.1% GA in PEM buffer for 10 minutes at room temperature. Fixed cells were stored at 4 °C in 1× PBS azide until use.

Preparation of fluorophore-labeled secondary antibodies

NHS ester functionalized dyes were used to conjugate with secondary antibodies. In brief, 40 µL of secondary antibody, 5 µL of 1M $NaHCO_3$, and 1-2 µg of fluorophore were mixed. The reaction mixture was protected from light and was completed in 30 minutes. The fluorophore-conjugated secondary antibody was purified and collected from the crude reaction mixture via a disposable NAP-5 column (GE Healthcare Life Sciences, 17085301), and further characterized by UV/Vis absorption spectroscopy.

Mouse organ dissection and preparation

All protocols and methods involving animals in this work were approved by the Institutional Animal Care and Use Committee (IACUC) at University of Washington.

Two-month old C57BL/6 male mice were anesthetized by isoflurane/oxygen mixture followed by cardiovascular perfusion with 1× PBS for 3 minutes followed by 4% PFA solution in 1× PBS for 5 minutes. Kidneys were then collected, and the renal capsules were removed. Other organs such as intestine and testis were also collected. Organs were fixed for 1-6 hours in 4% PFA solution in 1× PBS (see **Table S3.1** for details). Then they were washed by 1× PBS solution three times and sliced by a vibratome to 100 µm thick. Due to the softness of testis and intestine, agarose gel was used to embed them while slicing. All slices were stored in 1× PBS azide at 4 °C until use.

For the comparison of H&E and FLARE stains (**Fig. S3.7**), mouse kidney tissue was collected from healthy Balb/c male mice at 12 weeks of age. Kidneys were perfused with PBS to remove blood cells, fixed in 10% buffered formalin, and then embedded in paraffin. FFPE kidney tissue was sliced into sections of ~10 µm, deparaffinized and stained with hematoxylin and eosin (H&E) by Pathology Research Services Laboratory at University of Washington. The stained tissue sections were then imaged with an Aperio ScanScope AT2 digital whole slide scanner at the Harborview Medical Center (HMC) Digital Pathology Facility.

Human kidney and prostate preparation

A deidentified formalin-fixed and paraffin-embedded (FFPE) human kidney tissue block was obtained from NW BioTrust under approval from University of Washington Institutional Review Board with de-identification. Sections of ~60 µm thickness were prepared using a microtome. In order to deparaffinize the section, the section was soaked in xylene solution for 10 min. Then, the section was rehydrated by incubation in a series of ethanol/water mixtures with descending ethanol concentration (100%, 95%, 85%, 70%, 50%, 0%). Eventually, rehydrated slices were stored in 1× PBS at 4 °C until further use. Deidentified, freshly-fixed human prostate samples were received from the University of Washington Genitourinary Biorepository with patient consent and, stored at 4 °C, and 100 µm sections were prepared with a vibratome. Approval was obtained from the University of Washington Institutional Review Board.

Cell gelation, denaturation and expansion

The MAP (magnified analysis of the proteome) sample preparation used here for cells was adapted from Ku et al [100]. Fixed cells on 12 mm round coverslips were treated with 10 mM aqueous $NaBH_4$ solution for 10 min, washed with 1× PBS, and then incubated in monomer solution (20% (wt/wt) AA, 10% (wt/v) SA, 0.05% (wt/wt) BA, 4% (v/v) PFA, 0.67% (v/v) TEMED) overnight at room temperature before gelation with 0.2% (wt/v) APS at room temperature for at least 30 min. After polymerization, the cell-embedded hydrogel on the coverslip was cleared in denaturing solution (200 mM SDS, 200 mM NaCl, 50 mM Tris Base, pH 9.3) for 1 hr at 90 °C. The denatured cell-embedded hydrogel was then sequentially washed by PBST (1× PBS, 0.1% (wt/v) Triton X-100, and 0.02% (wt/v) NaN_3) and 1× PBS before placing into DI water for sample expansion.

Tissue gelation, denaturation/digestion, and expansion

The MAP sample preparation used here for expanded mouse kidney tissues was adapted from Unnersjö et al [112]. Fixed kidney sections were soaked in monomer solution (20% (wt/wt) AA, 10% (wt/v) SA, 0.05% (wt/wt) BA, 4% (v/v) PFA, 0.1% (wt/v) VA-44) overnight at 4 °C. Gelation was done at 45 °C for 2 hr. The polymerized gel was carefully peeled off, trimmed, and then transferred into denaturing solution (200 mM SDS, 200 mM NaCl, 50 mM Tris, pH 9.3). The expanded mouse kidney tissue was processed in a similar way but with denaturation at 70 °C for 24 hours followed by 90 °C for another 24 hours. The sample was then thoroughly washed by PBST before placing into DI water to expand.

The ExM sample preparation for **Fig. S3.3** was adapted from Chozinski et al [98]. Immunostained fixed mouse kidney sections were first incubated in 1 mM MA-NHS in 1× PBS at room temperature, followed by incubation in monomer solution (1× PBS, 2 M NaCl, 2.5% (wt/wt) AA, 0.15% (wt/wt) BA, 8.625% (wt/wt) SA) for at least an hour in 4 °C. Gelation of the kidney section was then done at 37 °C for 1.5-2.5 hr with monomer solution containing 0.2% (wt/wt) APS, 0.2% (wt/wt) TEMED and 0.01% (wt/wt) TEMPO. The hydrogel-embedded kidney sample was digested overnight with 8 units/mL proteinase K in proteinase digestion buffer (1× TAE buffer, 0.5% Triton X-100, 0.8 M guanidine hydrochloride) at 37 °C. The sample was then further digested

with 5 mg/mL collagenase in collagenase digestion buffer (1× HBSS with 0.7 mM $CaCl_2$) overnight at 37 °C.

General covalent staining procedure for hydrogel samples and cleared tissues

All samples were stained in the same sequence: carbohydrates, amines, and lastly, DNA. For carbohydrate staining, the samples were first oxidized with $NaIO_4$, then incubated with fluorescent dye ATTO 565-hydrazide after washing off excess $NaIO_4$. $NaCNBH_3$ was then used to reduce the hydrazone bond formed for better stability. The samples were then incubated with fluorescent dye ATTO 647N-NHS for the staining of amines in proteins after washing off excess $NaCNBH_3$. Lastly, fluorescent DNA dye (Hoechst 33258 or SYBR Green I) was added for nuclei staining. Samples were either expanded (for hydrogel samples) or refractive index matched with EC (for organic cleared samples) before imaging. A summary of the various reagents, buffers, quantities, and conditions for all data in this paper is listed in **Table S3.1**.

Immunostaining procedures

All non-transfected samples covalently stained prior to gelation were processed in this sequence: carbohydrates, amines, antibodies, gelation and lastly, DNA. For carbohydrate, amine, and DNA staining, see above section on General Covalent Staining Procedure. For general immunostaining of cell samples prior to gelation, the sample was incubated first in block and permeabilization solution (BP, 0.3% (wt/v) BSA, 0.5% (wt/v) Triton X-100, 1× PBS) for 30 min, followed by primary antibodies in BP for 90 min, and lastly, secondary antibodies in BP for 45 min. Samples were post-fixed with 0.25% GA in 1× PBS for 5 min. For general immunostaining of tissue samples, the same procedure was followed but with different incubation conditions (see Table S3.1 for details). After immunolabeling, samples for hydrogel expansion were treated for 1 hr with freshly-prepared 1 mM MA-NHS in 1× PBS.

All non-transfected cell samples covalently stained post-gelation were proceeded in this sequence: antibodies, gelation, carbohydrates, and lastly, amine. For post-gelation carbohydrate and amine staining, in order to immunostain prior to gelation, the procedure requires the use of secondary antibodies conjugated to biotin instead of a fluorescent dye because the mild

oxidation used in carbohydrate staining step later may chemically bleach fluorophores on the secondary antibodies.

For the transfected cell sample in **Fig. S3.2r-v**, immunostaining with anti-GFP Alexa Fluor 488 was performed after the post-gelation covalent stains. The immunostain on the hydrogel sample was performed in BP for 15 hr at room temperature. Samples were either expanded (for hydrogel samples) or refractive index matched with EC (for organic cleared samples) before imaging. A summary of the various reagents, buffers, quantities, and conditions for all data in this paper is listed in **Table S3.1**.

DNA fluorescence in situ hybridization

The DNA-FISH procedure was adapted from Beliveau et al. [160] FLARE-stained and MAP-expanded mouse kidney samples were first incubated in 0.5% Triton X-100 in 1× PBS for 2 hr. Samples were washed once in 1× PBS, then in 2× SSCT (0.1% Tween 20 in 2× SSC), and last in hybridization buffer (50% formamide, 0.1% Tween 20 in 2× SSC) for 10 minutes each time. Samples were incubated in fresh hybridization buffer for 30 min at 60 °C. The hybridization mixture (50% formamide, 10% dextran sulfate, 0.1% Tween 20, 3 mM sodium azide, 100 nM MaSat oligo probe, 100nM oligo reporter in 2× SSC) was pre-heated to 92.5 °C for 5 minutes, then added to each sample at an approximate 2:1 volume ratio. Samples were denatured at 92.5 °C for 10 minutes and hybridized at 37 °C overnight. Samples were washed three times in 2× SSCT, first at 60 °C, second at 37 °C and finally at room temperature, 15 minutes each time. Samples were stored in 0.2× SSCT at 4 °C for at least 1 hour or until needed for imaging (within a week). Before imaging, samples were fully expanded by replacing the sample buffer at least twice with water every ten minutes at 4 °C.

The MaSat oligo probe (5'-GGAATATGGC GAGAAAACTG AAAATCACGG AATGATACGG CGACCACCGA ACTGCTACAG-3') contains 30 nucleotides of the mouse Major satellite repeat DNA sequence (obtained from Lehnertz et al.[161]) and 30 nucleotides complimentary to the fluorophore conjugated oligo reporter (5'-/5ATTO647NN/ CTGTAGCAGT TCGGTGGTCG CCGTATCATT-3').

Organic solvent clearing

Stained tissue specimens were dehydrated using solutions of THF/H2O with ascending THF (v/v) concentrations (50%, 80%, 100%) as follows. Stained 100 µm thick tissue specimens were first incubated in 50% THF for 10 min, then in 80% THF twice for at least 15 min each, and lastly, in 100% THF twice for at least 15 min each. Stained 500-800 µm thick tissue specimens were first incubated in 50% THF for 30 min, then in 80% THF twice for at least 1 hr each and lastly in 100% THF twice for at least 1 hr each. After THF dehydration, 100% dichloromethane (DCM) was then added and incubated until the specimen sank. DCM was removed and 100% ethyl cinnamate oil (EC) was added to the sample followed by incubation for 2 hours or more. For thicker specimens, EC was exchanged a few times to ensure good index-matching.

Sample mounting

EC-cleared samples were transferred onto a rectangular #1.5 coverslip (Fisher Scientific, #12544E, 24 x 50 mm) using a paintbrush. A piece of double-sided tape was attached to the surface of the coverslip along the each of the short edges of the coverslip, then a drop of EC was added on sample surface to prevent it from drying, and a second coverslip was pressed onto the first to form a sandwich structure held together by the double-sided tape. For the fully expanded hydrogel-embedded samples, the gel was adhered to a poly-L-lysine coated coverslip and imaged immediately.

Fluorescence microscopy and imaging

All data, except for 1 mm EC cleared mouse kidney and **Supplementary Fig. S3.6-9**, were acquired using a Leica SP5 inverted confocal point scanning microscope at the University of Washington Biology Imaging Facility. The objective lenses used on the confocal microscope were a HC Plan Apo CS 63× 1.2 NA water-immersion objective, a HC Plan APO CS 63× 1.4 NA oil-immersion objective, a HC Plan Apo CS 20× 0.7 NA air objective, and a HC Plan Apo CS 10× 0.4 NA air objective. A summary of the various imaging conditions used for each data set can be found in Table S3.1.

Supplementary Fig. S3.7-9 were acquired with a conventional wide-field epifluorescence inverted Nikon Ti-S microscope. The objective lenses used on the wide-field microscope were CFI Plan Apo VC 60× 1.2 NA (Nikon, Melville, NY, USA) water-immersion objective, CFI S Plan Fluor 20× 0.45 NA (Nikon) air objective, and CFI Plan Apo λ 4× 0.2 NA (Nikon) air objective. The illumination source was a four-channel light emitting diode (LED4D251, Thorlabs, Newton, NJ, USA) that used a quad-band filter set (Chroma 89402). The detection unit used to capture the images was a ZWO-AS174MM-COOL CMOS camera (ZWO, Suzhou, China). When applicable, for single-channel observations, single-band emission filters (Chroma ET 525/50, ET 605/70, or ET700/75) were used.

Supplementary Fig. S3.6 was acquired with a homebuilt spinning disk confocal microscope using a Nikon CFI S Plan Fluor 20× 0.45 NA (Nikon) air objective lens. This microscope will be the subject of a future publication.

3D volumetric imaging of the 1 mm EC cleared mouse kidney was acquired using a recently published open-top light sheet microscope.[152] Briefly, illumination light is coupled into the system by a single-mode fiber from a four-channel (405, 488, 561, and 638 nm) laser package (Skyra, Cobolt Lasers). The light is scanned using a galvanometer, GM (6210H, Cambridge Technology) to create a digital light sheet with a numerical aperture of ~0.06. Fluorescence is collected by a multi-immersion objective (#54-10-12, Special Optics, distributed by Applied Scientific Instrumentation). This objective provides <1 µm in-plane resolution for clearing media with a usable refractive index range of 1.33 – 1.56. The collected fluorescence is focused onto a 2048×2048 pixel sCMOS camera (ORCA-Flash4.0 V2, Hamamatsu) by a tube lens, TL2 (TTL165, Thorlabs, f = 165 mm) which provides a sampling of ~0.45 µm/pixel at n = 1.56 which satisfies the Nyquist criterion. This results in a horizontal field of view of ~0.9 mm over the 2048 pixels of the camera. The vertical field of view is reduced to 256 pixels (113 µm) to closely match the depth of focus of the illumination light sheet (~110 µm). The 256 pixels are oriented parallel to the rolling shutter readout direction of the camera, which provides an exposure time of 1.25 ms and a frame rate of 800 Hz. 3D imaging is achieved using a combination of stage-scanning and lateral/vertical tiling with a motorized XY stage and Z actuators (FTP-2050-XYZ, Applied Scientific Instrumentation).

3.7 Acknowledgements

We would like to thank the Biology Imaging Facility at the University of Washington for imaging assistance, R. D. Palmiter and H. Y. Kueh (University of Washington, Seattle, WA) for providing mice for this study, M. Davidson for providing mEmerald-Golgi-7 plasmids (Addgene), T. Rapoport for providing pAc-GFPC1-Sec61β plasmids (Addgene, Watertown, MA), and C. E. Alpers and R. O. L. Wong (University of Washington, Seattle, WA) for access to tissue-sectioning instruments.

3.8 Supplementary Materials

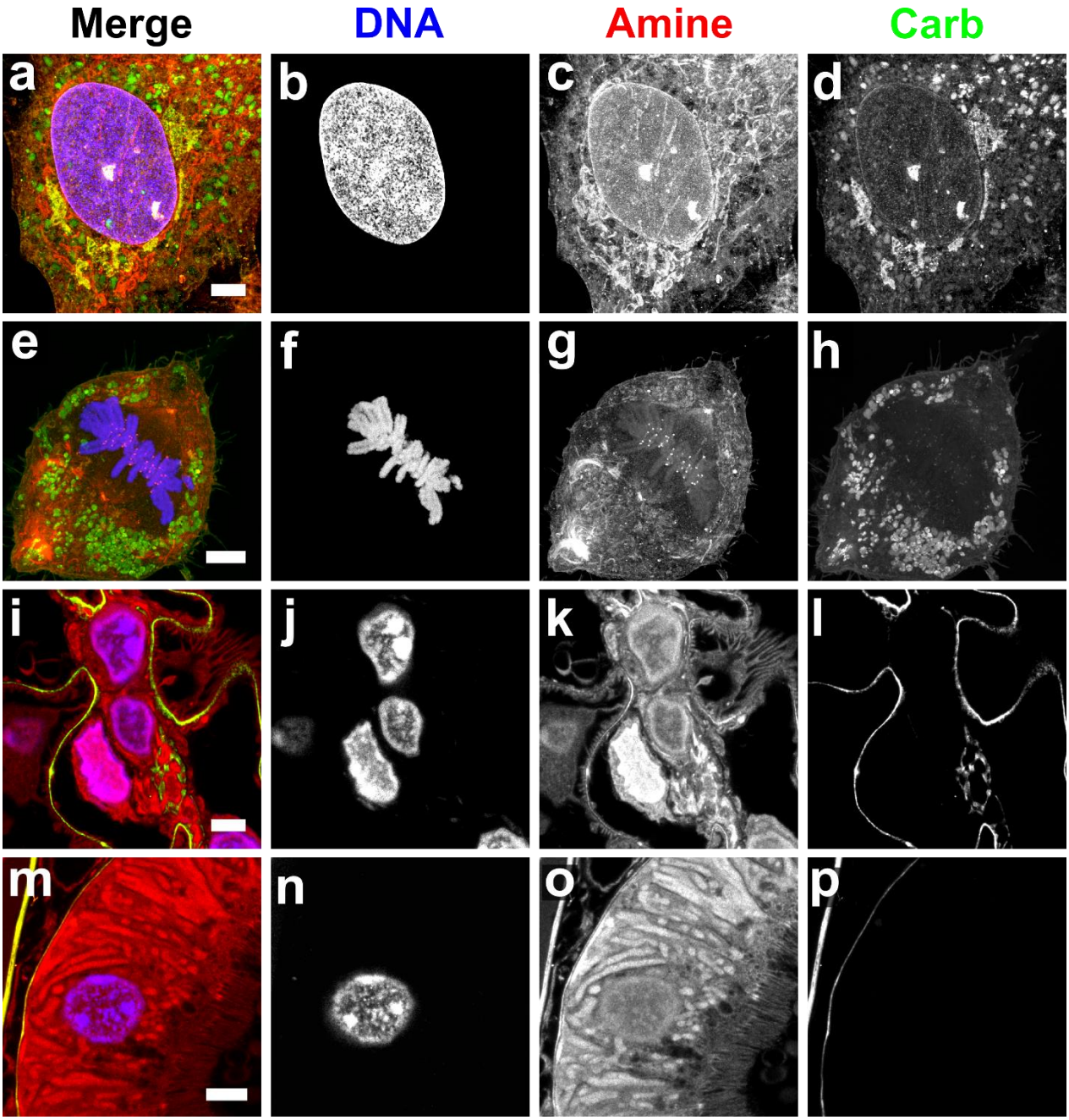

Fig. S3.1. Single-channel images from the multichannel data in Fig. 2 and 3.

Confocal microscopy images of expanded specimens stained for carbohydrates, amines, and DNA (see also **Fig. 2** and **Fig. 3**), together with their respective individual channels. These include (**a-d**) a single interphase RPE cell, (**e-h**) a single dividing RPE cell, (**i-l**) a region of a mouse kidney glomerulus, and (**m-p**) a region of a mouse kidney proximal convoluted tubule. Scale bars are 3 µm and are in pre-expansion units.

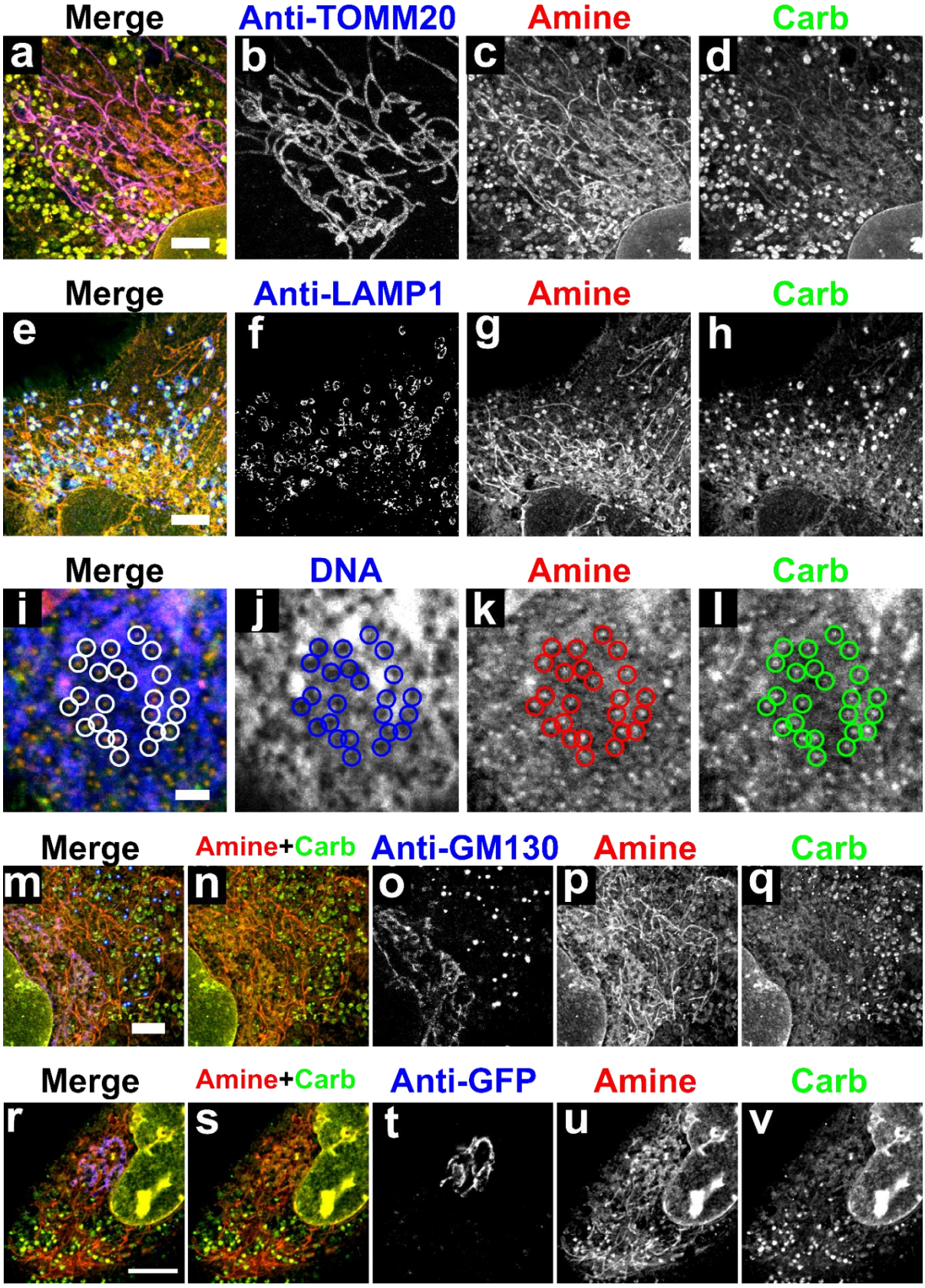

Fig. S3.2. Validation of sub-cellular features identified by FLARE staining in expanded RPE cells.

Confocal microscopy images of expanded RPE cells showing that mitochondria, lysosomes, nuclear pores, and parts of the Golgi apparatus are readily identifiable from covalent stains of amines and carbohydrates. (**a-d**) An immunostain against the mitochondrial protein TOMM20 colocalizes extensively with the filamentous structures in the amine channel. (**e-h**) An immunostain against the lysosomal protein LAMP1 colocalizes extensively with bright punctae in the carbohydrate channel. (**i-l**) In this zoom-in view of a region of a nucleus, heterochromatin voids in the DNA channel colocalize with punctae in the amine and carbohydrate channels and are indicative of nuclear pores (same cell as in **Fig. 2a**, but here a projection of a thin volume near the bottom of the nucleus). (**m-q**) An immunostain against cis-Golgi matrix protein GM-130 partially colocalizes with a distinct perinuclear signal coming from amine and carbohydrate channels. **(r)** Multichannel, maximum intensity projection of an expanded transfected RPE cell that was labeled with anti-GFP, (**s**) corresponding combined amine and carbohydrate channels, and (**t-v**) corresponding single-channel images. All scale bars are in pre-expansion units. Scale bars, 3 μm (**a**, **e**, **m,** **r**), 500 nm (**i**).

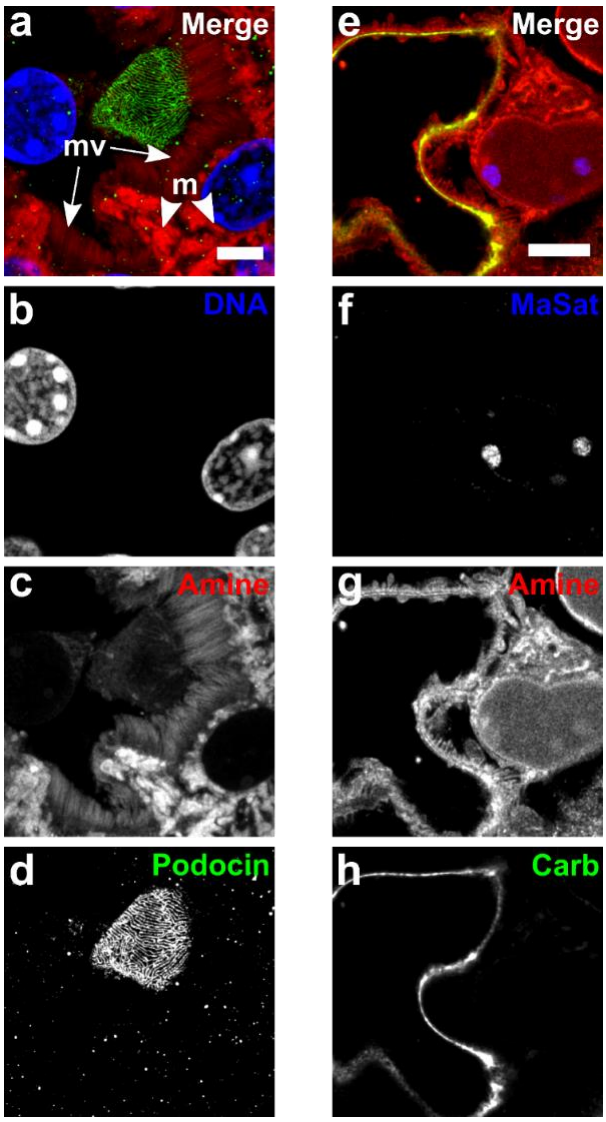

Fig. S3.3. Use of FLARE staining with enzymatic digestion expansion protocol or DNA FISH protocol mouse kidney tissue.

(a-d) Confocal microscopy images of expanded mouse kidney. Prior to covalent labeling, tissue was processed with an expansion microscopy (21) (ExM) procedure that uses enzymatic digestion, rather than a magnified analysis of the proteome (20) (MAP) procedure that uses heat and detergent to dissociate tissues as was done for all other expansion data in this paper (see **Materials and Methods** and **Supplementary Table 1**). Prior to gelation, the sample was immunolabeled against podocin and covalently stained for amines. After gelation, the sample was homogenized using enzymatic digestion, expanded, and stained with the DNA-binding dye Hoechst (see **Materials and Methods** and **Supplementary Table 1**). (**a**) Maximum intensity projection of a region showing interdigitated podocytes (green, podocin) on a glomerulus as well as a proximal convoluted tubule lined with microvilli ('mv') and containing abundant mitochondria ('m'). (**b-d**) corresponding single-channel images. (**e-h**) Confocal microscopy images of an expanded mouse kidney tissue that was stained for carbohydrates, amine, and then DNA FISH against pericentromeric major satellite (MaSat) DNA. (**e**) Multichannel, maximum intensity projection and (**f-h**) corresponding single channel images. Scale bars are 3 µm and are in pre-expansion units.

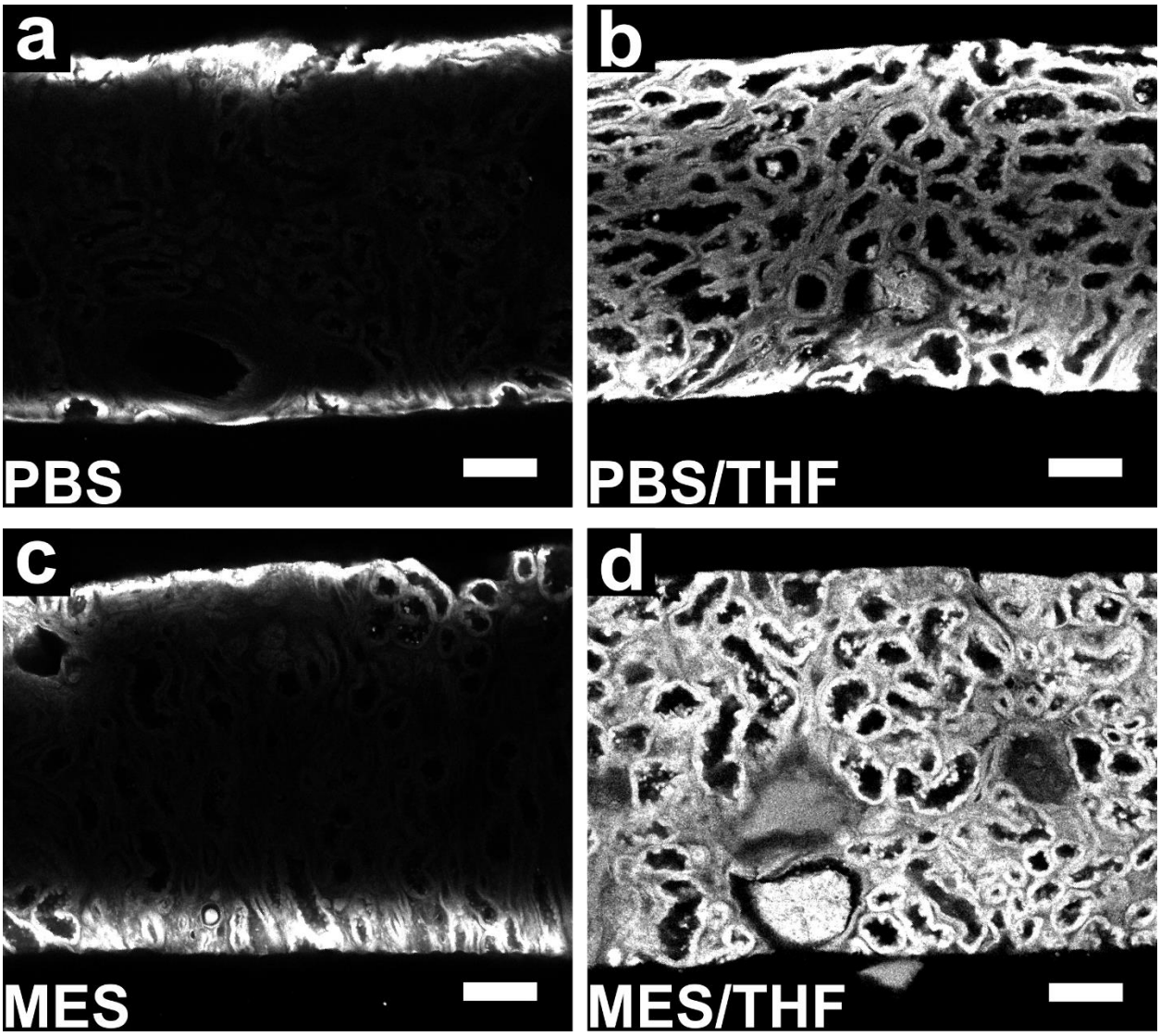

Fig. S3.4. Enhancement of FLARE stain uniformity in unexpanded thick tissue.

Comparison of stain uniformity for amine labeling of ~500 µm thick human kidney sections stained for 15 hours with 1 µg/mL ATTO 647N-NHS (see also **Fig. 4** for panel c and d). Sections were stained, cut perpendicular to the section face, and imaged on a confocal microscope to measure the stain intensity at different depths for (**a**) a pH 7.4 1×PBS solution, (**b**) a pH 7.4 1×PBS:THF (1:1) mixture, (**c**) a pH 6.0 MES buffer solution, and (**d**) a pH 6.0 MES:THF (1:1) mixture. Scale bars are 100 µm.

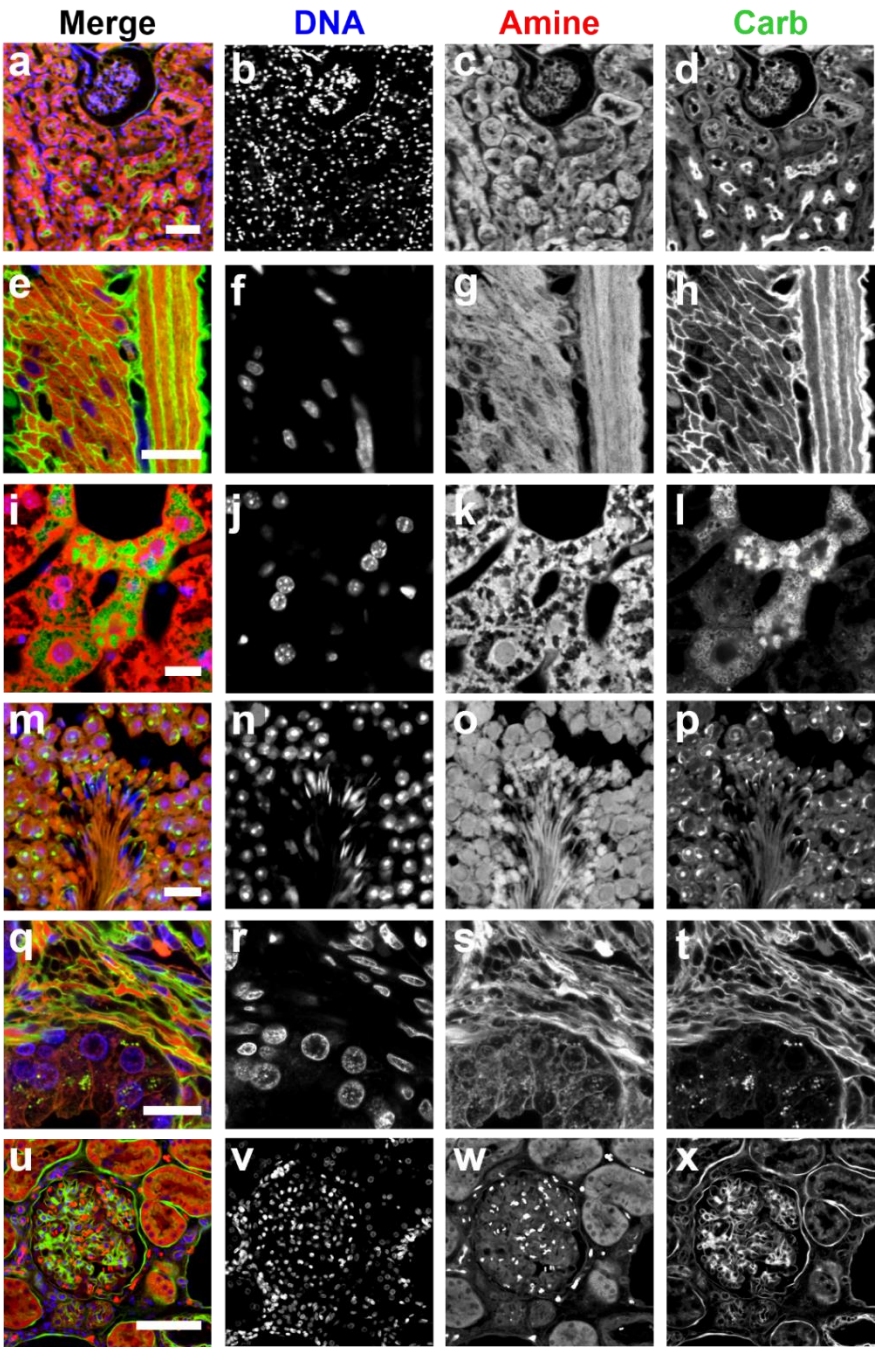

Fig. S3.5. Single-channel images from the multichannel data in Fig. 4 and 5.

Confocal microscopy images of unexpanded, optically cleared tissue specimens that were FLARE-stained for carbohydrates, amines, and DNA (see also **Fig. 4** and **Fig. 5**), together with their respective individual channels, including (**a-d**) a region of mouse half kidney tissue, (**e-h**) circular and longitudinal muscle from mouse intestine, (**i-l**) mouse liver, (**m-p**) mouse testis, (**q-t**) human prostate, and (**u-x**) a formalin-fixed, paraffin-embedded (FFPE) human kidney. All images are maximum intensity projections as described in Supplementary Table 1. Scale bars are 50 µm (**a**), 10 µm (**e**, **i**, **m**, **q**), and 100 µm (**u**).

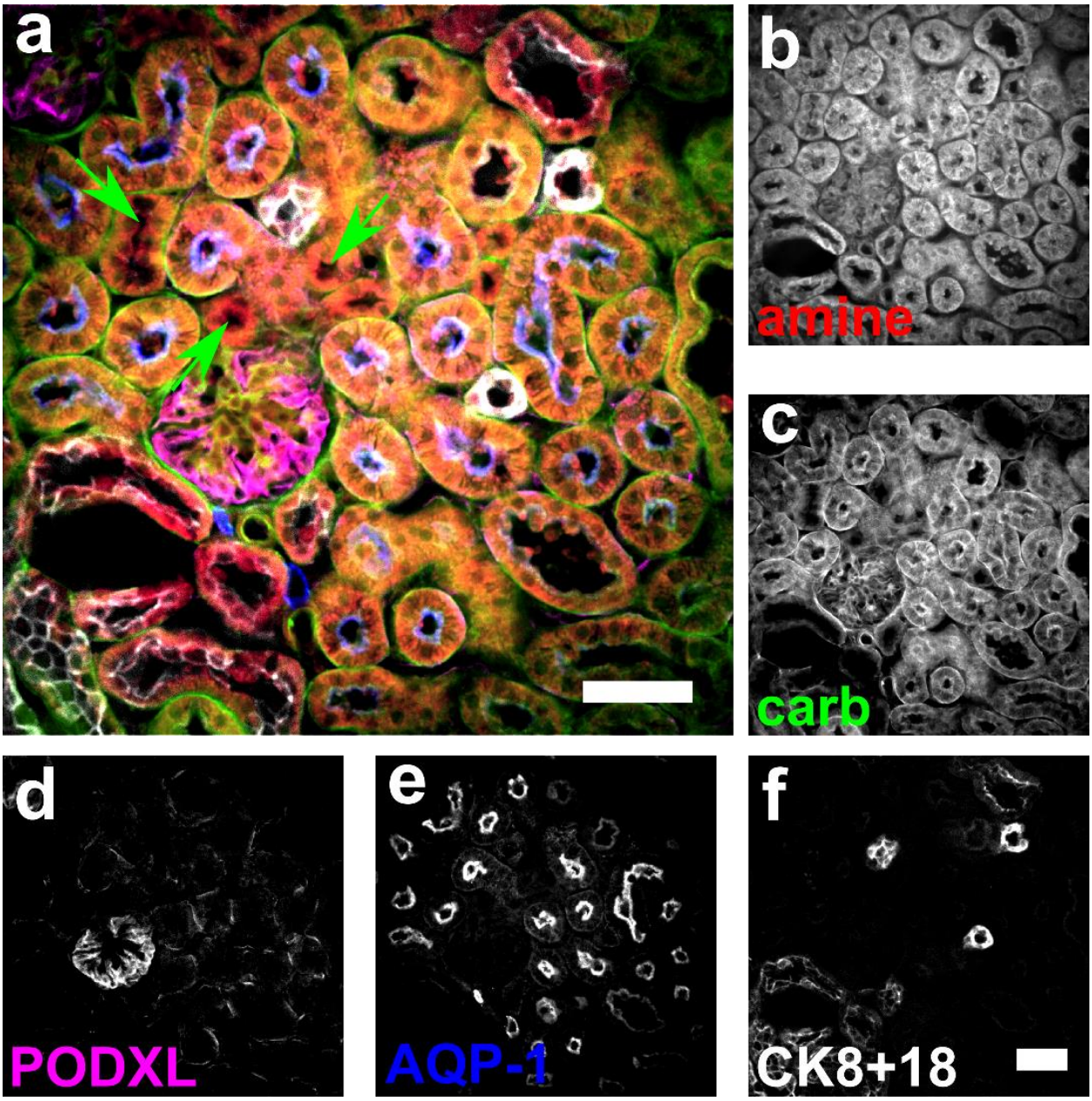

Fig. S3.6. Concurrent use of FLARE staining with immunostaining to identify general features in mouse kidney.

(**a**) Confocal microscopy image of a mouse kidney tissue section that was stained for carbohydrates and amines, and then immunostained for podocalyxin (PODXL, labels glomeruli), aquaporin-1 (AQP-1, labels proximal tubules), and cytokeratin 8+18 (CK8+18, labels collecting ducts). Renal tubules that lack antibody signals here are most likely distal convoluted tubules and are indicated by green arrows. (**b**-**f**) Corresponding single-channel images of the specific channels indicated. Scale bars are 50 µm.

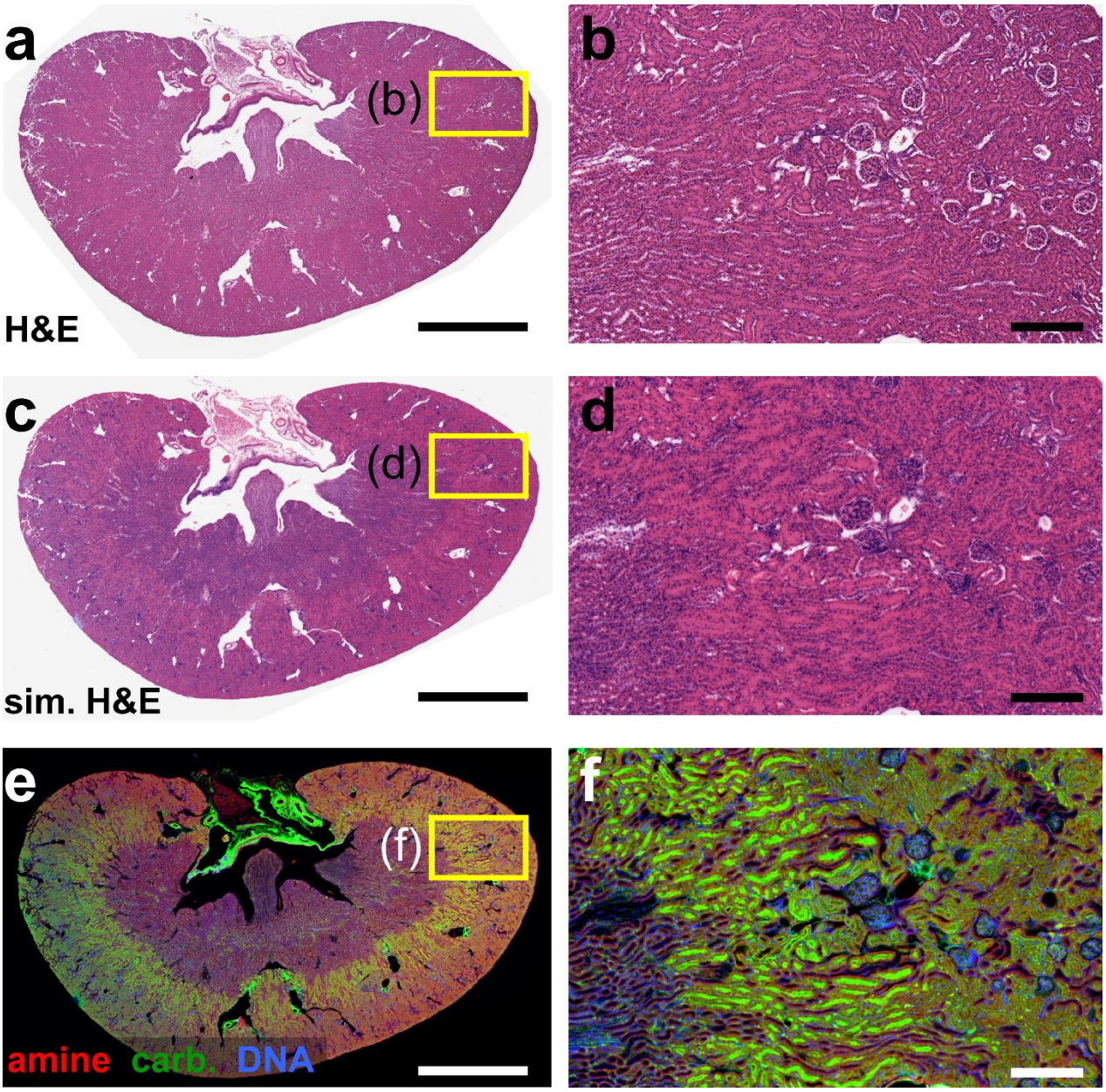

Fig. S3.7. Side-by-side comparison of H&E and FLARE stains on FFPE mouse kidney sections.

Two consecutive 10 µm thick mouse kidney FFPE sections were used for (**a-b**) H&E and (**c-f**) FLARE stains, respectively. The FLARE stain DNA and amine channels were converted to a simulated (sim.) H&E image **(c-d)**, showing a similar pattern as for H&E. However, the molecular distribution and general features are substantially more informative in (**e-f**) the standard fluorescence display. Scale bars are 2 mm (**a, c, e**), 200 µm (**b, d, f**).

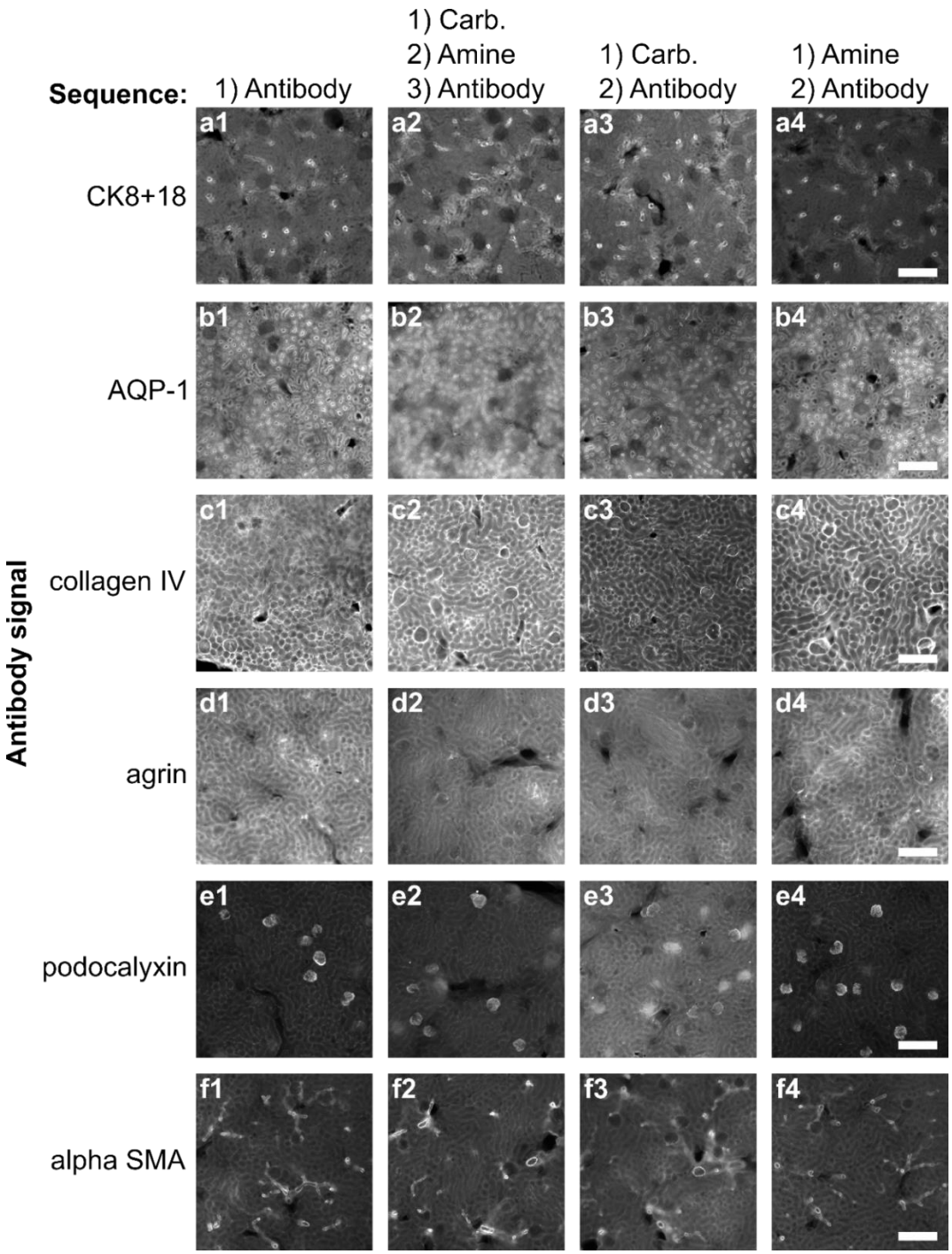

Fig. S3.8. Effect of FLARE staining on antibody binding for unexpanded mouse kidney tissue.

Unexpanded mouse kidney tissue was labeled with various covalent reactions (or none) as indicated in the column headings, immunostained against the protein indicated in each row, and then imaged by widefield fluorescence microscopy. None of the six immunostains were perturbed by the covalent labeling of amines (compare columns 1 and 4) but agrin immunostaining was partially perturbed by covalent labeling of carbohydrates (compare columns 1 and 3). Scale bars are 200 μm.

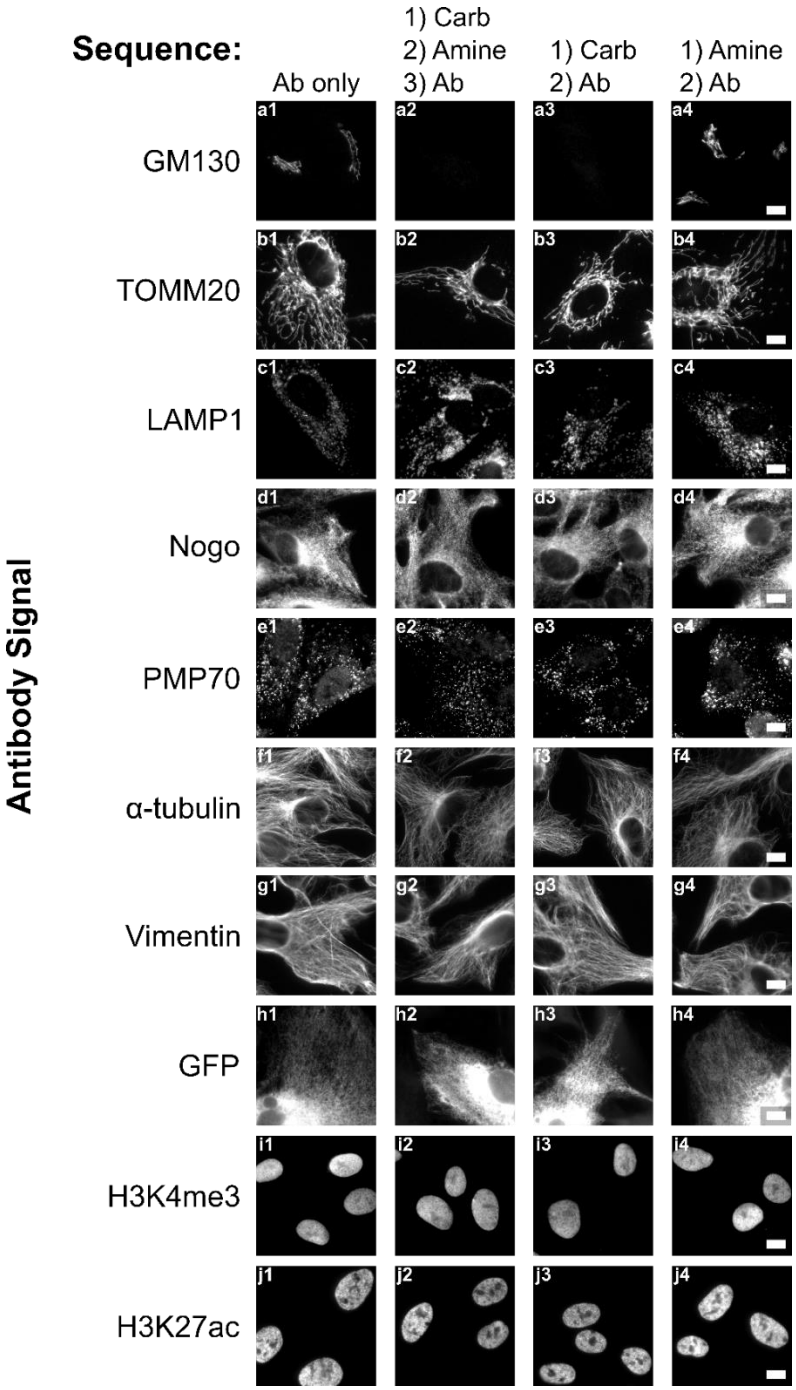

Fig. S3.9. Effect of FLARE staining on antibody binding for unexpanded RPE cells.

Unexpanded RPE cells were labeled with various covalent reactions (or none) as indicated in the column headings, immunostained against the protein indicated in each row, and then imaged by widefield fluorescence microscopy. None of the ten immunostains were perturbed by the covalent labeling of amines (compare columns 1 and 4) but GM130 immunostaining was disrupted by covalent labeling of carbohydrates (compare columns 1 and 3). Scale bars are 10 µm. Ab = antibody; Carb = carbohydrate covalent stain; Amine = amine covalent stain.

Table S3.1. Summary of sample preparation and imaging conditions.

Fig.	Sample	Fixation	Tissue Sectioning	Carbohydrate Stain	Amine Stain	Other Stain(s) and Stain Order	Expansion or Clearing	Imaging
2	RPE cell	PFA/GA 10min	---	1hr, 20mM $NaIO_4$ in 100mM NaOAc with 1M NaCl, pH5; then 3hr, 6.65μM hydrazide-AT565 in 100mM NaOAc, pH5; then 30 min, 50mM $NaBH_3CN$ in 100mM NaOAc, pH5.	1hr, 3.0μM NHS-AT647N in PBS.	DNA: 30min, 1.96μM SYBR Green in DI water Order: gel, covalent stains, expand, DNA.	Expansion	Confocal, 63× 1.2NA water lens. Image thickness: a) 738nm, b) 462nm, c) 738nm, d) 1.85μm, e) 1.57μm, f) 462nm. Filter: none.
3	Mouse kidney	PFA 1hr	100μm vibratome sections	Same as **Fig. 2**.	6hr, 5.9μM NHS-AT647N in 100mM MES, pH6.	DNA: 30min, 1.87μM Hoechst 33258 in PBS, pH7.4. Order: gel, covalent stains, DNA, expand.	Expansion	Confocal, 63× 1.2NA water lens. Image thickness: 92.3nm. Filter: 2.
4a-b	Human kidney	PFA 1hr	500μm vibratome sections (resliced after labeling)	---	1.2μM NHS-AT647N, 15hr in a) MES, b) MES:THF (1:1).	---	Clearing	Confocal, 10× 0.4NA air lens. Image thickness: 1.52μm. Filter: none.
4c-d	Mouse kidney	PFA 1hr	500μm vibratome sections (resliced after labeling)	4hr, 100mM $NaIO_4$ in 100mM NaOAc, pH5; then 15hr, 1.2μM hydrazide-AT565 in c) NaOAc and d) THF:NaOAc (1:1); then 30min, 50 mM $NaBH_3CN$ in THF:NaOAc (1:1).	---	---	Clearing	Confocal, 10× 0.4NA air lens. Image thickness: 1.52μm. Filter: none.
4e	Mouse kidney	PFA 1hr	500μm vibratome sections	---	2 hr, 17.7μM NHS-AT647N in THF: MES (1:1).	Immuno: Rb×Collagen 5 μg/mL 72hr; D×Rb AT488 10μg/mL, 72hr; at 4°C. Order: immuno, covalent stain, clear.	Clearing	Confocal, 10× 0.4NA air lens. Image thickness: 1.52μm. Filter: none.
4f-h	Mouse kidney block	PFA 1hr	1mm vibratome section	6hr, 100mM $NaIO_4$ in 100mM NaOAc, pH5; then 6hr, 3.33μM hydrazide-AT565 in THF:NaOAc (1:1); then 1hr, 100mM $NaBH_3CN$ in THF:NaOAc (1:1).	8hr, 5.9μM NHS-AT647N in THF: MES (1:1).	DNA: 15hr, 20μM SYBR green in H_2O: PBS (1:1). Order: covalent stains, DNA, clear.	Clearing	Light sheet microscope, 20× 0.43NA oil lens. Image thickness: f-h) 446nm. Filter: none.
5a-f	Mouse intestine, liver, testis, human prostate	PFA 1hr, intestine, testis; PFA 6hr, liver; formalin 20hr, prostate	100μm vibratome sections	30min, 100mM $NaIO_4$ in 100mM NaOAc, pH 5; then 2hr, 3.33μM hydrazide-AT565 in THF:NaOAc (1:1); then 30min, 100mM $NaBH_3CN$ in THF:NaOAc (1:1).	2hr, 5.9μM NHS-AT647N in THF: MES (1:1).	DNA: 30min, 1.87μM Hoechst 33258 in THF: PBS (1:1). Order: covalent stains, DNA, clear.	Clearing	Confocal, a) 20× 0.7NA air lens, b-f) 63× 1.4NA oil lens. Image thickness: a) 8.06μm, b) 2.26μm, c) 377nm, d) 377nm, e) 1.89μm, f) 377nm. Filter: a-e) none, f) 2.
5g	Human FFPE kidney	Formalin 24hr	60μm microtome sections	Same as **Fig. 5a-f.**	Same as **Fig. 5a-f.**	Same as **Fig. 5a-f.**	Clearing	Confocal, g) 20× 0.7NA air lens. Image thickness: 1 μm. Filter: 2.
S1a-h	RPE cell	Same as **Fig. 2**	---	Same as **Fig. 2.**	Same as **Fig. 2.**	Same as **Fig. 2.**	Expansion	Same as **Fig. 2.**
S1i-p	Ms. kidney	Same as **Fig. 3**	---	Same as **Fig. 3.**	Same as **Fig. 3.**	Same as **Fig. 3.**	Expansion	Same as **Fig. 3.**
S2a-d	RPE cell	Same as **Fig. 2**	---	Same as **Fig. 2.**	Same as **Fig. 2.**	Immuno: Rb×TOMM20 2μg/mL 90min; D×Rb biotin 3μg/mL 45min; streptavidin AF488 5μg/mL in PBS 15hr; at −20°C. Order: immuno, gel, covalent stains, streptavidin, expand.	Expansion	Confocal, 63× 1.2NA water lens. Image thickness: a-d) 646nm. Filter: none.
S2e-h	RPE cell	Same as **Fig. 2**	---	30min, 20mM $NaIO_4$ in 100mM NaOAc with 1M NaCl, pH5; then 1.5hr, 2.66μM hydrazide-AT565 in 100mM NaOAc, pH5; then 15min, 50mM $NaBH_3CN$ in 100mM NaOAc, pH5.	1hr, 1.2μM NHS-AT647N in PBS.	Immuno: Rb×LAMP1 4μg/mL 90min; D×Rb AF488 5μg/mL 45min; at −20°C. Order: covalent stains, immuno, gel, expand.	Expansion	Confocal, 63× 1.2NA water lens. Image thickness: e-h) 923nm. Filter: none.
S2i-l	RPE cell	Same as **Fig. 2**	---	Same as **Fig. 2.**	Same as **Fig. 2.**	DNA: Same as **Fig. 2.** Order: Same as **Fig. 2.**	Expansion	Confocal, 63× 1.2NA water lens. Image thickness: i-l) 277nm. Filter: none
S2m-q	RPE cell	Same as **Fig. 2**	---	Same as **Fig. 2.**	Same as **Fig. 2.**	Immuno: Ms×GM130 2μg/mL 90min; D×Ms biotin 3 μg/mL 45min; streptavidin AF488 5μg/mL in PBS 15hr; at −20°C. Order: immuno, gel, covalent stains, streptavidin, expand.	Expansion	Confocal, 63× 1.2NA water lens. Image thickness: m-q) 1.15μm. Filter: none.
S2r-v	RPE cell transfected	Same as **Fig. 2**	---	Same as **Fig. 2.**	Same as **Fig. 2.**	Immuno: Rb×GFP-AF488 4μg/mL 15hr; at −20°C. Order: gel, covalent stains, immuno, expand.	Expansion	Confocal, 63× 1.2NA water lens. Image thickness: f-j) 185nm. Filter: none.
S3a-d	Mouse kidney	PFA 1hr	100μm vibratome sections	---	1hr, 3.0μM NHS-AF546 in PBS.	DNA: Same as **Fig. 3a-d**. Immuno: Rb×Podocin 5μg/mL 18hr; D×Rb AT488 5μg/mL 18hr; at 4°C. Order: immuno, covalent stain, gel, expand, then DNA.	Expansion	Confocal, 63× 1.2NA water lens. Image thickness: 1.04μm. Filter: none.
S3e-h	Mouse kidney	PFA 1hr	100μm vibratome sections	Same as **Fig. 3.**	Same as **Fig. 3.**	DNA FISH: denature 10min at 92.5°C; hybridize 18hr at 37°C with 100nM MaSat oligo + 100nM AT647N oligo. Order: gel, covalent stains, DNA FISH, then expand	Expansion	Confocal, 63× 1.2NA water lens. Image thickness: 92nm. Filter: 2.
S4	Human kidney	PFA 1hr	500μm vibratome sections	---	1.2μM NHS-AT647N, 15hr in: a) PBS, b) PBS:THF (1:1), c) MES, d) MES:THF (1:1).	---	Clearing	Confocal, 10× 0.4NA air lens. Image thickness: 1.52μm. Filter: none.
S5a-d	Mouse kidney	PFA 1hr	1mm vibratome section	Same as **Fig. 4g**	Same as **Fig. 4g**	Same as **Fig. 4g**	Clearing	Same as **Fig. 4g**
S5e-x	Same as for **Fig. 5a-g**	Same as **Fig. 5a-g**	Same as **Fig. 5a-g**	Same as **Fig. 5a-g**	Same as **Fig. 5a-g**	Same as **Fig. 5a-g**	Clearing	Confocal, e-t) 63× 1.4NA oil lens, u-x) 20× 0.7NA air lens. Image thickness: Same as **Fig. 5a-g** Filter: e-l) none, m-t) 2, u-x) none.
S6	Mouse kidney	PFA 1hr	100μm vibratome sections	30min, 100mM $NaIO_4$ in 100mM NaOAc, pH 5; then 1hr, 3.33μM hydrazide-Al568 in NaOAc; then 30min, 100mM $NaBH_3CN$ in NaOAc.	1hr, 3.0μM NHS-AT647N in 1× PBS	Immuno: 2μg/mL G×PODXL, Rb×AQP-1, Gp×CK8+18 18h; 2μg/mL D×G-AFdye405, D×Rb-AF488, D×Gp-AF750 18h; at −4°C. Order: covalent stains, immuno	Neither	Homebuilt spinning-disk confocal, 20× 0.45NA air lens; imaging cocktail was tris 200mM pH8.0, 10% glucose, 1mM Trolox, 0.4mg/mL glucose oxidase, 0.2% catalase. Image thickness: single plane Filter: none
S7a-b	Mouse kidney	Formalin 24hr	10μm microtome sections	---	---	---	Neither	Aperio ScanScope AT2 digital whole slide scanner for H&E.
S7c-f	Mouse kidney	Formalin 24hr	10μm microtome sections	Same as **Fig. S6**	Same as **Fig. S6**	Immuno: 2μg/mL primary ab. 18h; 2μg/mL secondary ab. (AF 488 conjugates) 18h; at −4°C. Order: covalent stains, immuno	Neither	Widefield, 20× 0.45NA air lens. Image thickness: single plane. Filter: none.
S8	Mouse kidney	Same as **Fig. 3**	100μm vibratome sections	Same as **Fig. S6**	Same as **Fig. S6**	Immuno: 2μg/mL primary ab. 18h; 2μg/mL secondary ab. (AF488 conjugates) 18h; at −4°C. Order: covalent stains, immuno	Neither	Widefield, 4× 0.2NA air lens. Image thickness: single plane. Filter: none.
S9 a-e	RPE cell	PFA/GA 10min	---	30min, 20mM $NaIO_4$ in 100mM NaOAc with 1M NaCl, pH5; then 1.5hr, 2.66μM hydrazide-AT565 in 100mM NaOAc, pH 5; then 15min, 50mM $NaBH_3CN$ in 100mM NaOAc, pH5.	1hr, 1.2μM NHS-AT647N in PBS.	Immuno: 2μg/mL primary ab. 90min; 2μg/mL secondary ab. (AF488 conjugates) 45min; at −20°C. Order: covalent stains, immuno	Neither	Widefield, 60× 1.2NA water lens. Image thickness: Single plane. Filter: none.
S9 h	RPE cell	PFA/GA 10min	---	Same as **Fig. S9 a-e**	1hr, 1.2μM NHS-AT565 in PBS.	Immuno: 2μg/mL of Rb×GFP-AF647 90min; at −20°C. Order: covalent stains, immuno	Neither	Same as **Fig. S9 a-e**
S9 f-g	RPE cell	0.5% Triton-x100 extraction 30sec, PFA/GA 10min	---	Same as **Fig. S9 a-e**	Same as **Fig. S9 a-e**	Same as **Fig. S9 a-e**	Neither	Same as **Fig. S9 a-e**
S9 i-j	RPE cell	4% PFA 10min	---	Same as **Fig. S9 a-e**	Same as **Fig. S9 a-e**	Immuno: permeabilize 10min with 0.1% Triton-x100 in PBS; 2μg/mL primary ab. 18h at −4°C; 2μg/mL secondary ab. (AF488 conjugates) 2hr at ~20°C. Ab. incubations in 10% (w/v) BSA in PBS. Order: covalent stains, immuno	Neither	Same as **Fig. S9 a-e**

Acronyms: Ab=antibody; AF=Alexa Fluor; AT=ATTO-TEC; DI=deionized; FFPE=formalin-fixed, paraffin-embedded; NA=numerical aperture; RPE=retinal pigment epithelium cell line.

Additional notes: median filter indicates number of pixels used for application of 3D median filter if used on confocal data sets. Image thickness refers to the thickness of the data displayed in terms of the pixel sizes of the data set, where distances are in pre-expansion units for expanded tissues.

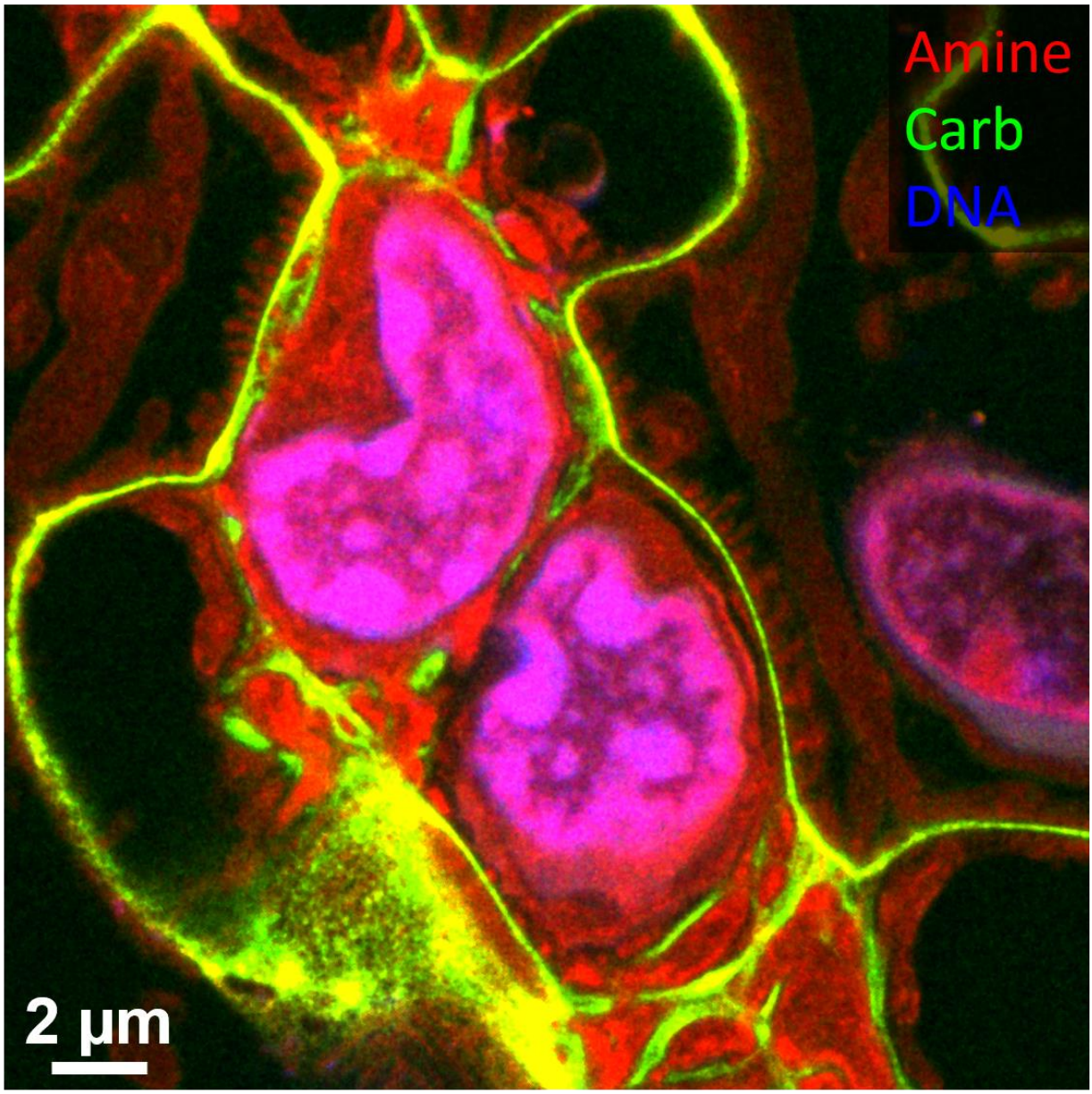

Fig. S3.10 Animation of FLARE-stained expanded mouse kidney.

Shown is the first frame from an animation of an expanded mouse kidney section that focuses on a small volume of a glomerulus. The animation shows successive z-slices of the confocal stacks, and highlights the basement membrane of capillary loops and mesangial matrix (green) as well as the fine details of the interdigitated podocyte epithelial cells (red). The same data set was used to create Fig. 3a-c. The animation covers a depth of 12.1 µm. All distances are in pre-expansion units.

CHAPTER 4. FLARE PROTOCOL AND TROUBLESHOOTING

4.1 Preface

The previous chapter described a method, named FLARE (Fluorescent Labeling of Abundant Reactive Entities), that used established reactive fluorophores to label a variety of biological specimens that were either expanded or cleared. These fluorophores target chemical groups on the specimens; NHS-ester fluorophores target amines on the sample while hydrazide fluorophores target oxidized carbohydrates on the sample. We showed that many key features and landmarks were visibly well-contrasted despite the relative abundance of these chemical groups in the samples. The labeling process is easy and robust. However, there are many factors that must be considered when determining the best procedure for the various types of sample. Therefore, in this chapter, I include protocols specifically for either expanded (**Section 4.3**) or organic-solved based cleared specimens (**Section 4.4**), with a focus on ways to troubleshoot some known issues that I encountered while developing the method (**Section 4.5**).

4.2 Introduction

Histological staining produces labels that are bright and reproducible but suffer from certain drawbacks. The dyes used are limited spectrally and because the stains are mostly affinity-based, they are easily removed with washing and are not suitable for techniques such as expansion microscopy which requires sample to be highly processed and washed in large volumes of water.[162] (**Chapter 3**) Immunolabeling is a powerful routine method of visualizing specific proteins in a biological specimen. However, there are challenges as well, such as poor penetration through thick complex specimens and lot-to-lot variability.[37,163] Thus, FLARE aims to address the challenges of histological staining and immunolabeling by producing bright and reproducible stains that could be used for expansion microscopy and be tuned for thick specimen labeling, while revealing a variety of highly contrasted features with the fluorescence microscope. The utility in a variety of tissues and sample types were highlighted in **Chapter 3**.

FLARE uses established reactive fluorophores to target different types of abundant chemical groups in biological specimens, such as amines and carbohydrates. (**Fig. 3.1**) The reactions are well-known and were selected for mildness, even though chemical modifications on a sample may induce slight difficulties in combination with other labeling methods such as immunolabeling (**Fig. S3.8-9**). (**Section 3.4.4**, **Section 4.6**) This newly developed labeling method was used for imaging techniques such as expansion microscopy (**Chapter 1.5.4**) and cleared tissue imaging (**Chapter 1.4**). With the combination of these various labeling and imaging techniques, there were bound to be challenges that required troubleshooting (**Section 4.5**) and these details are described in this chapter.

4.3 Protocol 1: Small-molecule Staining of Expanded Cultured Cells and Tissues

The following protocol was optimized for fixed Retinal Pigment Epithelium Cells (H-tert RPE-1) and for fixed mouse kidney specimens. Several modifications in the protocol are necessary when applying FLARE to expanded tissue specimens. In this case, the modifications pertaining to expanded kidney specimens appear in solid boxes in the following text. The gelation procedure prior to or after chemical staining in this protocol is adapted and modified from "Multiplexed and scalable super-resolution imaging of three-dimensional protein localization in size-adjustable tissue" (doi:10.1038/nbt.3641).[100] The bold numbers in brackets denote the quantities used during the experiment.

Cell culture fixation followed standard procedures as briefly described here: H-tert RPE-1 were grown to ~70–90% confluency and seeded (~30,000–70,000 cells/well) on #1.5 round coverslip in 24-well culture plates. After 24 hours, the cells were fixed with 3.2% PFA and 0.1% glutaraldehyde in PEM buffer (100 mM aqueous PIPES disodium salt, 1 mM $MgCl_2$, 1 mM EGTA) for 10 minutes at room temperature (~20 °C). Fixed cells were stored in 1× phosphate buffered saline with 3 mM sodium azide (1× PBS azide) at 4 °C prior to use. Tissue fixation followed standard procedures that are briefly described in Protocol 2 (**Section 4.4**).

Other tissues or fixation conditions may require adjustment of the procedure.

4.3.1 Chemical reagents

- 10× PBS, pH 7.4 (e.g., Fisher Bioreagents # L-5400)
- Sodium Azide (NaN_3, Fisher Scientific #S227I)
- Sodium acetate, anhydrous (NaOAc, Fisher Scientific #S209)
- Sodium chloride (NaCl, Fisher Scientific #271)
- 4-Morpholineethanesulfonic acid (MES, Sigma-Aldrich, #M8250)
- Sodium periodate ($NaIO_4$, Sigma-Aldrich, #311448)
- Sodium cyanoborohydride ($NaCNBH_3$, Sigma-Aldrich, #156159)
- ATTO 647N NHS ester (AT647N-NHS, Sigma-Aldrich, #18373)
- ATTO 565 hydrazide (AT565-$NHNH_2$, ATTO-TEC GmbH, #AD565)
- Hoechst 33258 (Sigma-Aldrich, #B2883)
- SYBR Green 1 (Invitrogen, S7563)
- Deionized water (DI water)
- Ammonium persulfate (APS, Bio-Rad Laboratories, #161-0700)
- Tetramethylethylenediamine (TEMED, Bio-Rad Laboratories, #161-0800)
- 32% Paraformaldehyde (PFA, Electron Microscopy Sciences, #RT15714)
- 50% glutaraldehyde (GA, Electron Microscopy Sciences, #16300)
- Sodium borohydride ($NaBH_4$, Fisher Scientific, #AC189300050)
- 40% Acrylamide (AA, Bio-Rad Laboratories, #161-0140)
- 2% bis-acrylamide (BA, Bio-Rad Laboratories, #161-0142)
- Sodium acrylate (SA, Sigma-Aldrich, #408220)
- Triton X-100 (Sigma-Aldrich, #X100)
- Poly-Lysine (Sigma-Aldrich, #P8920)
- Sodium dodecyl sulfate (SDS, Sigma-Aldrich, #L3771)
- Tris base (Tris, Fisher Scientific, #BP152-500)

Caution: Researchers should consult the safety data sheets (SDSs) for these chemicals prior to use. Procedures using $NaCNBH_3$, PFA, GA, AA, and BA should be performed in a fume hood and researchers are advised to be cautious.

4.3.2 Other Materials

- Coverslip #1.5 (Fisher Scientific, #12544E, 24 x 50 mm)
- 12 mm round coverslip (Electron Microscopy Sciences, #72230-01)
- Forceps (Electron Microscopy Sciences, #78318-3)
- Parafilm M Bemis (VWR, #52858)
- Razor blade (American Line, #66-0089)
- 12 well-plate (Pipette, #712011)
- 6 well-plate (Pipette, #229106)
- Scintillation vial (Wheaton, #986546)

4.3.3 Stock solutions

- 1× PBS (pH 7.4)
- NaOAc buffer: 100 mM NaOAC, 1 M NaCl in DI water, pH 5.
    - 246 mg NaOAC + 1.75 g NaCl in 25 mL of DI water, adjust pH with 1 M HCl, adjust final volume to 30 mL with additional DI water.
    - Store at room temperature. It should be stable for at least two weeks.
- MES buffer: prepare 100 mM MES, 150 mM NaCl in DI water, pH 6.
    - 586 mg MES + 263 mg NaCl in 25 mL of Di water, adjust pH with 1 M NaOH, adjust final volume to 30 mL with additional DI water.
    - Store at room temperature.
- AT565-$NHNH_2$ master stock with concentration of 5 mg/mL (6.65 mM).
    - Add 200 µL of anhydrous DMSO to 1 mg of AT565-$NHNH_2$.
    - Store at -20 °C until use.
- AT647N-NHS ester master stock with a concentration of 5 mg/mL (5.93 mM).
    - Add 200 µL of anhydrous DMSO to 1 mg of AT647N-NHS.

    - Store at -20 °C until use.
- SYBR green master stock with a concentration of 10 mg/mL (19.6 mM).
    - Add 100 µL of anhydrous DMSO to 1 mg of SYBR green.
    - Store at -20 °C until use.
- Monomer solution: 20% (w/v) AA + 10% (w/v) SA + 0.05% (w/v) BA + 4% (w/v) PFA + 0.67% (w/v) TEMED.
    - 2 mL 40% AA + 400 mg SA + 0.1 mL BA + 0.5 mL 32% PFA + 26.8 µL TEMED, adjust final volume to 4 mL with 1× PBS.
    - Store at 4 °C for up to 1 week, protected from light.
- Denaturing solution: 200 mM SDS + 200 mM NaCl + 50 mM Tris, pH 9.3.
    - 1.73 g SDS + 350 mg NaCl + 182 mg Tris base in 20 mL of DI water, adjust pH with 0.1 M HCl, adjust final volume to 30 mL with additional DI water.
    - Store at 37 °C until use.
- PBST solution: 1× PBS + 0.1% Triton X-100 + 0.02% NaN_3.
    - 13 mg NaN_3 + 1 mL Triton X-100 in 1 L 1× PBS.
    - Store at room temperature until use.

4.3.4 Procedures

Reduction (for samples fixed with GA to quench remaining aldehydes from the fixation process and to lower the amount of GA induced fluorescence; otherwise may omit)

1. Prepare a fresh, aqueous 10 mM $NaBH_4$ solution **[4 mg $NaBH_4$ in 10 mL DI H_2O].**
2. Incubate the fixed cells in the $NaBH_4$ solution for 10 min **[~0.5mL per well].**
3. Wash cells with 1×PBS **[0.5mL per well, repeat three times].**

4. **Monomer solution infusion.** Add the monomer solution to each well and incubate at room temperature (RT) overnight **[0.5mL per well].** Protect the solution from light during the incubation.

Tissue sample monomer infusion procedure: The monomer solution recipe is slightly different for tissue samples (20% AA, 10% SA, 0.05% BA, 4% PFA, 0.1% VA-044, 1× PBS) and requires the use of a heat-sensitive initiator VA-044. The sample is incubated in monomer solution overnight at 4 °C while protected from light.

Gelation

5. Prepare a fresh, aqueous 10% (w/v) APS solution **[10 mg APS in 90 µL DI H_2O].** Keep the solution on ice until use.
6. Pipette 98 µL of monomer stock solution into a microcentrifuge tube.
7. Pipette 2 µL of 10% APS solution into the microcentrifuge tube, quickly mix, and add 70 µL of mixed solution onto a piece of Parafilm (~5 cm × 5 cm).
8. Use the forceps to carefully take out the round coverslip with fixed cells from the well, and carefully place the coverslip with cells facing down onto the solution prepared from the previous step.
9. Wait 30 min for the solution to polymerize at RT. Protect the solution from light during polymerization. Note that any solution left in the microcentrifuge tube can be used to judge the progress of the gelation process.

Tissue Sample Gelation: Using a paint brush, spread a 100 µm section of tissue on a rectangular #1.5 coverslip, place two stacked small pieces of #1.5 coverslip on either side of the sample to act as spacers, add one drop of monomer solution **[99 µL of fresh monomer solution + 1 µL of 10% VA-44]** on the tissue surface, and place another rectangular #1.5 coverslip on top to create a tissue gelation chamber. The drop of monomer solution should cover the entire sample area (up to ~ 1 cm^2). Put the sample in a glass chamber and purge with nitrogen before shutting the airtight lid., Incubate the chamber at 45 °C for 2 hr.

10. Use a ruler to measure the gel size to obtain the pre-expansion size for calculation of expansion factor later in step 22.

Denaturation

11. Use a razor blade to peel off the gel from the Parafilm. Avoid peeling the gel off the coverslip at this point as this could damage the cells.
12. Transfer the gel attached to the round coverslip into a scintillation vial containing denaturing solution **[10 mL solution each sample]**.
13. Denature the cell sample for 60 minutes at 95 °C. Note that the hydrogel will typically expand ~2× during this process. The heating process can be done using heat blocks on an orbital shaker.
14. Transfer the gel to a large volume of PBST solution to wash out denaturing reagents. This wash step should be repeated three times for 30 min each time. After which, 1× PBS is used to wash all detergents out prior to chemical staining.

Tissue Sample denaturation: For mouse kidney tissue samples, incubate in denaturing solution at 70 °C for 24 hours first, and then at 90 °C for an additional 24 hours. For more details, refer to "Confocal super-resolution imaging of the glomerular filtration barrier enabled by tissue expansion" (doi: 10.1016/ j.kint.2017.09.019). [112]

The following covalent chemical staining is done in this general order: carbohydrates, amines, then DNA. Due to the possible chemical bleaching of fluorophores by sodium periodate in the oxidation step (to oxidize carbohydrates to form aldehydes), it is preferable to stain carbohydrates first, before applying other fluorescent labels.

Carbohydrate stain

15. **Oxidation (converts carbohydrate vicinal diols to aldehydes)**
    a) Prepare a fresh, aqueous 20 mM $NaIO_4$ solution **[43 mg $NaIO_4$ in 10 mL NaOAc buffer]**.

b) Cut a piece of hydrogel to a suitable size (e.g., 1×1 cm^2) and transfer into 20 mM $NaIO_4$ solution in a 6-well plate.

c) Let the oxidation reaction run for one hour while gently agitating the container on an incubator shaker at 37 °C. Protect the solution from light during reaction.

16. **Hydrazone formation (couples hydrazide dye to oxidized carbohydrate aldehydes)**

    a) Remove the solution and wash the sample with NaOAc buffer at room temperature **[10 mL per wash, repeat three times]**.

    b) Transfer the hydrogel sample into a well of a 12-well plate.

    c) Dilute AT565-$NHNH_2$ master stock in NaOAc buffer to final concentration 5 µg/mL and add to the well containing sample **[1 µL dye in 1 mL NaOAC buffer, for 6.66 µM final concentration]**.

    d) Let the reaction run for 3 hours with gentle agitation on an orbital shaker.

17. **Reduction (converts imine bond to a more stable amine bond)**

    a) Prepare a fresh 100 µL of 5 M $NaCNBH_3$ solution **[31.4 mg $NaCNBH_3$ in 100 µL NaOAc buffer]**. **Note:** $NaCNBH_3$ should be stored in an inert condition. $NaCNBH_3$ is a milder reductant than $NaBH_4$. $NaBH_4$ may turn off certain fluorophores (such as cyanines).

    b) Add 20 µL of the $NaCNBH_3$ solution directly to the sample well of step 15c.

    c) Allow the sample to react for 30 min with gentle agitation.

    d) Wash the sample with NaOAc buffer for 15 min **[2 mL each, repeated twice]**. Then allow the sample to remain in the NaOAc buffer overnight.

    e) Wash the sample with 2 ml of 1× PBS solution **and finally** store in 1× PBS for later use.

Amine stain (couples NHS dye to primary amine)

18. Prepare 2.5 µg/mL AT647N-NHS from master stock **[add 1 µL dye to 2 mL 1× PBS for 2.97 µM final concentration]**.

19. Incubate sample with AT647N-NHS solution for 1 hr with gentle agitation and while covered to protect from light.
20. Wash the sample twice with 2 ml of 1× PBS. Then store in 1× PBS for further use.

Tissue Sample amine labeling: Use 100 mM MES buffer pH 6.0, instead of PBS, as the buffer when labeling of tissue in order to slow down the hydrolysis and coupling reactions to help ensure a uniform stain. A concentration of 5.9 µM AT647N-NHS in MES with a reaction time of 6 hr gave good stains for the expanded kidney tissue. Faster stains can be achieved with a higher concentration of dye and a shorter reaction time.

Expansion

21. Transfer the sample in an excess volume of DI H_2O enough to cover a 100 mm Petri Dish (~30 mL) and let it expand for at least 1 hr. Frequent DI H_2O changes speeds up the expansion process. Note that the sample should sink completely.
22. Remove water and use a ruler to measure the post-expansion size and divide the value by the pre-expansion size (found in step 10) to obtain the approximate expansion factor. **Note:** This is the macroscopic expansion factor and is the same as the microscopic expansion factor when done properly. However, there may be discrepancies and one should keep an eye out for such discrepancies especially in new specimens that were not previously validated.

DNA stain and mounting

23. Prepare 10 µg/mL SYBR green solution from the master stock **[add 1 µL dye to 1 mL DI H_2O]**.
24. Apply the solution directly to the surface of the gel containing the cells and incubate for 20 minutes.
25. Rinse the sample three times with an excess of DI H_2O to remove unbound SYBR green.
26. Temporarily transfer the gel to an untreated coverslip and remove excess liquid by wicking the edges with a Kimwipe. To eliminate drift during imaging, carefully

slide the gel onto a poly-l-lysine coated coverslip to create strong adhesion between the gel and the poly-l-lysine surface. Excess water beneath the gel may hinder the adhesion and add unnecessary imaging depth. It is best to image the sample immediately. **Note:** The poly-L-lysine coated coverslips for imaging may be prepared ahead of time and are stable for weeks. Evenly spread 2-3 µL of a 1 mg/mL poly-l-lysine solution on the surface of a hydrophilic coverslip and allow it to dry. Exposing the coverslip to an air plasma in a plasma cleaner for ~1 minute is the preferred way to render the slides hydrophilic prior to spreading the poly-L-lysine solution, but not required.

4.4 Protocol 2: Small-molecule Staining and Clearing of Unexpanded Tissue Sections

This protocol is designed for 100 µm thick tissue vibratome sections. The bold numbers included in brackets are the quantities used during the experiment.

Tissue fixation and slicing following standard protocol are as briefly described here: mouse tissue specimens are typically obtained by cardiac perfusion with 1× PBS for 3 minutes followed by 4% PFA solution in 1× PBS for 5 minutes (7mL/min); after removal of the organ of interest, the tissue is further fixed in 4% PFA at 4 °C depending on the thickness of the tissue (e.g., adult mouse kidney was immersion-fixed in 4% PFA for 1 hour, while adult mouse liver was fixed for 6 hr.). The fixed tissue was then sliced on a vibratome into ~100 µm sections and were stored in a multiwell plate in 1× PBS buffer (pH 7.4) at 4 °C until ready for further processing.

Sections of different size, as well as FFPE or cryosections, may require further optimization. For example, thicker specimens (> 100 µm) will require longer incubation times for staining and clearing.

4.4.1 Chemical reagents

- 10× PBS, pH 7.4 (Fisher Bioreagents # L-5400)
- Sodium acetate anhydrous (NaOAc, Fisher Scientific #S209)
- Sodium chloride (NaCl, Fisher Scientific #271)

- 4-Morpholineethanesulfonic acid (MES, Sigma-Aldrich, #M8250)
- Sodium periodate ($NaIO_4$, Sigma-Aldrich, #311448)
- Sodium cyanoborohydride ($NaCNBH_3$, Sigma-Aldrich, #156159)
- Tetrahydrofuran (THF, Fisher Scientific, #T425)
- Dichloromethane (DCM, Fisher Scientific, #D37)
- Ethyl cinnamate (EC, Sigma-Aldrich, #112372)
- ATTO 647N NHS ester (AT647N-NHS, Sigma-Aldrich, #18373)
- ATTO 565 hydrazide (AT565-$NHNH_2$, ATTO-TEC GmbH, #AD565)
- Hoechst 33258 (Sigma-Aldrich, B2883)
- Deionized water (DI water)

Caution: Researchers should consult the safety data sheets (SDSs) for these chemicals prior to use. THF and DCM are volatile and flammable. $NaCNBH_4$ is toxic. All procedures involving using these chemicals should be performed in a fume hood and researchers are advised to be cautious.

4.4.2 Other Materials

- Rectangular #1.5 glass coverslip (Fisher Scientific, #12544E)
- Paint brush (Black Art Materials, #05130-1000)
- Scintillation vial, large enough (~28 mm diameter) to hold tissue section (Wheaton, #986546)

4.4.3 Stock solutions

- 1× PBS (pH 7.4)
- NaOAc buffer: 100 mM NaOAC, in DI water, pH 5.
    - 246 mg NaOAC in 25 mL of DI water, adjust pH with 1 M HCl, adjust final volume to 30 mL with additional DI water.
    - Store at room temperature.
- MES buffer: prepare 100 mM MES, 150 mM NaCl in DI water, pH 6.

    - 586 mg MES + 263 mg NaCl in 25 mL of DI water, adjust pH with 1 M NaOH, adjust final volume to 30 mL with additional DI water.
    - Store at room temperature.
- AT565-$NHNH_2$ master stock with concentration of 5 mg/mL (6.65 mM).
    - Add 200 µL of anhydrous DMSO to 1 mg of AT565-$NHNH_2$.
    - Store at -20 °C until use.
- AT647N-NHS ester master stock with a concentration of 5 mg/mL (5.93 mM).
    - Add 200 µL of anhydrous DMSO to 1 mg of AT647N-NHS.
    - Store at -20 °C until use.
- Hoechst 33258 master stock with a concentration of 10 mg/mL (19.6 mM).
    - Add 100 µL of anhydrous DMSO to 1 mg of Hoechst 33258.
    - Store at -20 °C until use.
- THF/NaOAc solution: to prepare, mix equal volumes of THF and NaOAc buffer.
    - Prepare fresh from stocks.
- THF/MES solution: to prepare, mix equal volume of THF and MES buffer.
    - Prepare fresh from stocks.
- THF/PBS solution: to prepare, mix equal volume of THF and 1× PBS buffer.
    - Prepare fresh from stocks.

4.4.4 Procedures

The following covalent chemical staining is done in this general order: carbohydrates, amines, then DNA. Due to the possible chemical bleaching of fluorophores by sodium periodate in the oxidation step (to oxidize carbohydrates to form aldehydes), it is preferable to stain carbohydrates first, before applying other fluorescent labels.

Carbohydrate Stain

1. **Oxidation (converts vicinal alcohols on carbohydrates to aldehydes)**
    a. Prepare a fresh, aqueous 100 mM $NaIO_4$ in pH 5.0 NaOAc buffer **[214 mg $NaIO_4$ in 10 mL NaOAc buffer]**.

b. Use a paint brush to gently transfer a tissue section into the above solution in a scintillation vial. Note that having the tissue section float, initially, at the surface of the solution in the well plate makes the transfer to a scintillation vial easier and helps avoid damage to the tissue section.
c. Let the reaction run for 30 minutes while gently agitating the sample on an orbital shaker or rocker. Protect the solution from light during reaction.

2. **Hydrazone formation (couples hydrazide dye to oxidized carbohydrate aldehydes)**
    a. Remove the solution and wash the sample with NaOAc buffer **[10mL per wash, repeat three times]**.
    b. Dilute AT565-$NHNH_2$ master stock in fresh THF/NaOAc solution to final concentration 2.5 µg/mL **[1 µL dye in 2 mL THF/NaOAc solution, for 3.33 µM final concentration]**.
    c. Incubate on orbital shaker for 2 hours.

3. **Reduction (converts imine bond to a more stable amine bond)**
    a. Prepare 100 µL of fresh 5 M $NaCNBH_3$ solution **[31.4 mg $NaCNBH_3$ in 100 µL NaOAc buffer]**. **Note:** $NaCNBH_3$ should be stored in an inert condition. $NaCNBH_3$ is a milder reductant than $NaBH_4$. $NaBH_4$ may turn off certain fluorophores (such as cyanines).
    b. Add 10 µL of $NaCHBH_3$ solution directly into the reaction mixture in 2b.
    c. Allow the sample to react for 30 minutes on an orbital shaker.
    d. Wash the sample with fresh THF/NaOAc solution **[10 mL per wash, repeat two times]**.
    e. Wash the sample with 10 mL of fresh THF/MES solution then store in THF/MES solution for later use.

Amine Stain (couples NHS dye to primary amine)

4. Prepare 2.5 µg/mL AT647N-NHS from master stock **[add 1 µL dye to 2 mL THF/MES solution, for 2.97 µM final concentration]**.

5. Incubate sample with AT647N-NHS solution for 2 hours with gentle rocking and protect from light.
6. Wash the sample with fresh THF/MES solution **[10 mL per wash, repeat two times]**.
7. Transfer the sample into 10 mL of fresh THF/PBS solution and store for further use.

DNA stain

8. Prepare 5 µg/mL Hoechst 33258 solution **[add 1 µL dye to 2 mL THF/PBS solution]**.
9. Allow the sample to react for 30 minutes with gentle rocking and while covered to protect from light.
10. Briefly wash the sample with fresh THF/PBS solution **[10 mL per wash, repeat two times]**.

Dehydration and refractive index matching

11. Transfer the sample into fresh 50% (v/v) THF in DI water **[4 mL]**.
12. Incubate sample for 30 minutes with gentle rocking and protect from light.
13. Incubate sample for 30 minutes in 80% THF (v/v) in DI water **[3.2 mL THF and 0.8 mL DI water]**.
14. Incubate sample for 30 minutes in 100% THF **[4 mL THF]**.
15. Soak the sample into DCM until it sinks **[4 mL DCM]**.
16. Finally, incubate sample with EC to match refractive index **[1 mL EC]**. The duration of the dehydration and index matching step will depend on the type of tissue and its thickness, but ~2 hours is a good starting point. It may be necessary to refresh the EC solution multiple times for thicker samples to ensure good index-matching. The clarity of the cleared tissue is easy to judge by the unaided eye.

Sample mounting

17. Use a paint brush to transfer the sample onto a rectangular #1.5 coverslip. Note that at this point, the sample is now rigid due to dehydration and thus would not entangle with the brush and can be easily transferred.
18. Attach a piece of double-sided tape to the surface of each of the two short edges of the coverslip.

19. Add one drop of EC to fully cover the sample.
20. Press a second rectangular #1.5 coverslip onto the first to form a sandwich structure held together by the double-sided tape.

4.5 Sample Preparation Troubleshooting

4.5.1 Issues with Expansion

Poor or uneven expansion is easily visualized by sample tearing or pinch points in the nuclei distribution and is usually caused by inadequate denaturation or digestion of the sample. (**Fig. 4.1**) This may be remedied by extending the denaturation period and/or repeating the denaturation step at a higher temperature. In the case of proteolytic digestion, an addition of another category of enzyme may help with digestion.[108] (**Fig. 4.1**)

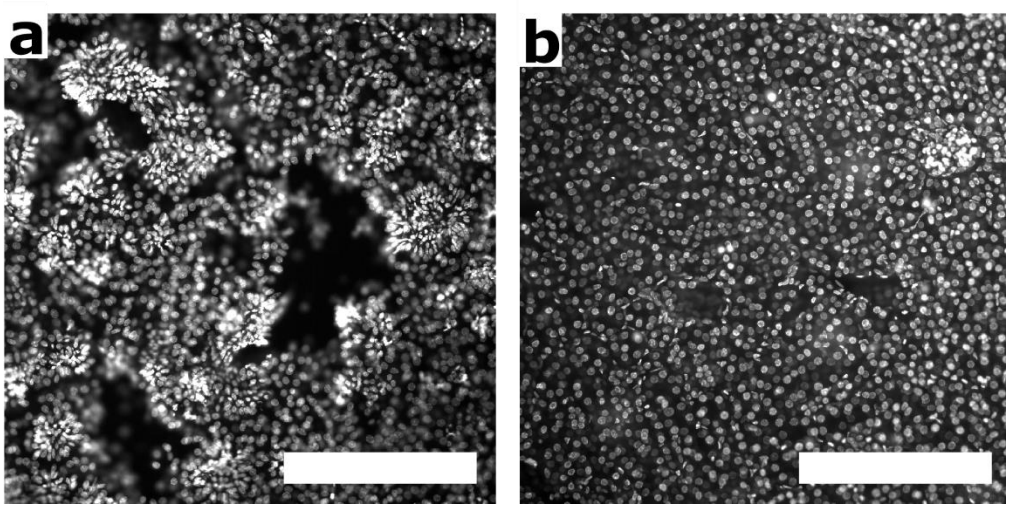

Fig. 4.1. Epifluorescence images showing DNA stained with Hoechst in expanded 100 µm mouse kidney that were digested differently.

DNA distribution can be an indication of adequate digestion. Both mouse kidney tissues were treated with MA-NHS for protein linkage to hydrogel. (a) Mouse kidney tissue digested with proteinase K only results in abundant tears (empty areas) and under-expanded regions (pinch points) showing relatively small or stretched nuclei. (b) Mouse kidney tissue that was digested first with proteinase K followed by an additional enzyme, collagenase, results in uniform sample homogenization and a reduction in obvious distortions observed in the expanded state. Scale bars (pre-expansion): 200 µm (a,b). Figure and caption adapted from Chozinski *et al*.[108] Scientific Reports. Copyright Nature Publishing Group. Creative Commons License can be found here.

4.5.2 Issues with No Signal

Lack of signal can arise due to several reasons. First, researchers should check that their microscope settings are appropriate to the fluorophores with a suitable positive control. Second, researchers should make sure that the hydrogel polymerization is done on the coverslip side coated with cells as it can be easy to lose track of which side of a coverslip the cells are adhered to. (**Fig. 4.2a**) Third, it is possible that the gel is upside down, and the surface of the hydrogel containing the sample is outside the working distance of the objective lens. (**Fig. 4.2b**) Fourth, the $NaIO_4$ oxidation step will chemically bleach many fluorophores and adequate removal of the $NaIO_4$ by thorough washing is required prior to the hydrazide dye incubation. Importantly, the hydrazide labeling step should be performed before the NHS-dye coupling reaction, or any other fluorescent labeling reactions.

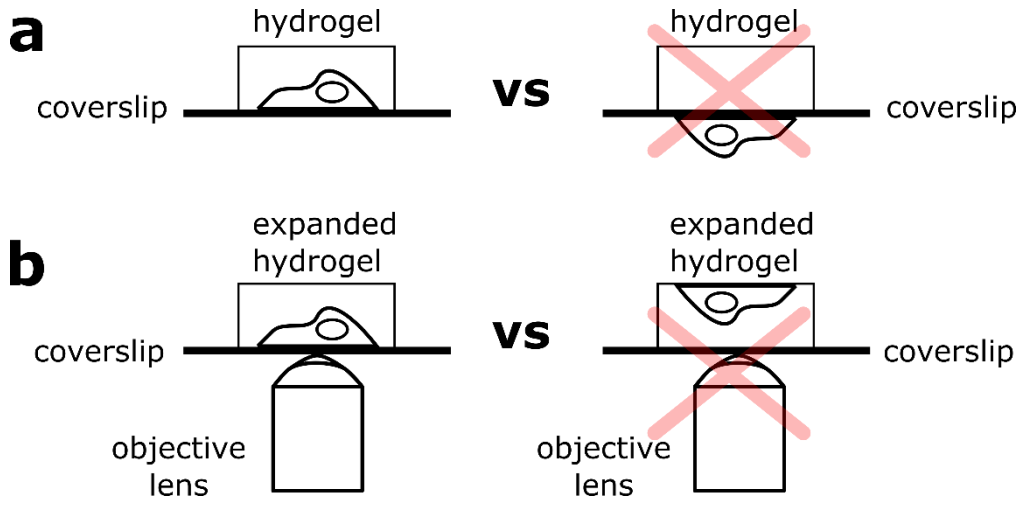

Fig. 4.2. **Figure showing cell sample orientation in hydrogel.**

a) Hydrogel polymerization on the side coated with cells (left) vs polymerization on the incorrect side (right). If the polymerization was done on the side without the cells, then the subsequent hydrogel would not have any cells embedded resulting in zero signal under the microscope. b) Expanded hydrogel mounted on poly-lysine coated coverslip, where cell sample in the working distance of the objective (left) and the cell sample on the opposite side of coverslip (right). If the hydrogel is mounted as seen on the right, the cell sample might not be in the working distance of the objective lens.

4.5.3 Issues with Dim Signal

Dim signals can arise due to several reasons. First, reagent degradation can result in an inefficient reaction. If the carbohydrate stain is dim, it could indicate that $NaCNBH_3$, which can become deactivated with prolonged exposure to moist air, has been hydrolyzed, leaving the hydrazide-dye conjugated to the specimen by a relatively labile hydrazone bond. If the amine channel is dim, it could indicate that the NHS groups on the NHS-dye have been hydrolyzed and thus the dyes were not efficiently coupled to the sample. In either of these cases, researchers can repeat the procedure using fresh aliquots or newly purchased reagents. In addition, proper storage can help slow down the degradation of these reagents. Second, the sample staining intensity can be tuned to produce brighter signals by increasing the concentration of the reactive fluorophores used in the labeling reactions. Third, with respect to hydrogel-embedded sample, make sure that the hydrogel surface containing the sample is placed face-up in a container during the labeling reaction, or the dyes may have a harder time accessing the sample resulting in dim signals. (**Fig. 4.3**) Fourth, it is essential to carefully choose the correct objective lens for a given type of sample: water-immersion objective lenses are well-suited to imaging specimens in hydrogels, whereas oil-immersion lenses are well-suited to imaging organic cleared oil refractive index matched EC specimens. The use of wrong immersion lenses may lead to optical aberrations and loss of signal at substantial depths. Lastly, dim signal may at times be a result of inner filter effect. (see **Section 4.5.4**)

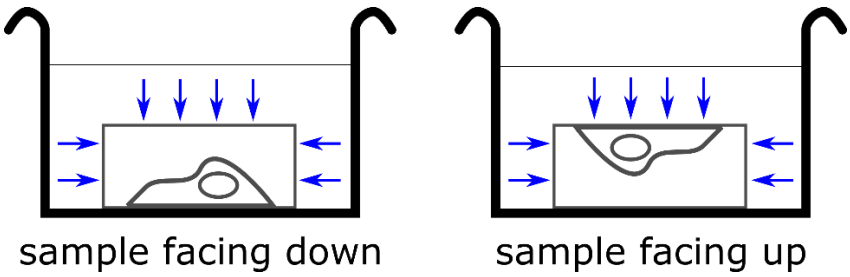

Fig. 4.3. **Figure showing the orientation of hydrogel in dye incubation container.**

If the cell sample is facing down (left), the dyes have lower accessibility to the sample (blue arrows), resulting in dimmer stains. If the cell sample is facing up (right), the dyes have higher accessibility to the sample (blue arrows), resulting in brighter stains.

4.5.4 Issues with Uneven Signal

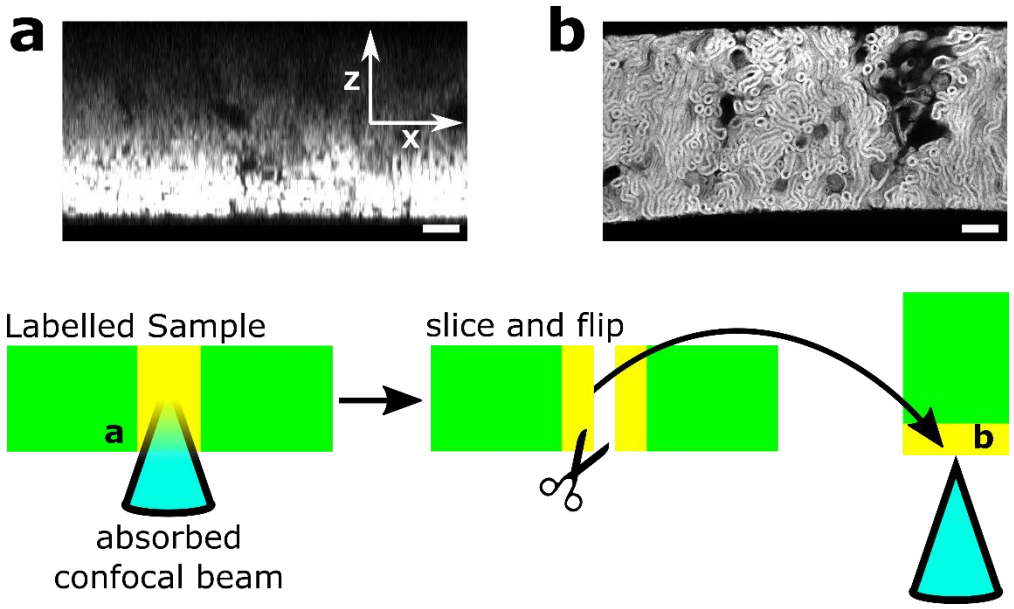

Fig. 4.4. Confocal images of densely labeled 500 µm human kidney stained with AT647N-NHS ester in MES/THF co-solvent showing prominent Inner Filter Effect, with a figure showing imaging procedure.

a) Cross-sectional view of kidney slice z-stack showing strong signal close to the coverslip with decaying intensity at depth (increasing z distance). The kidney slice was then cut, flipped on edge, and b) reimaged to show the newly revealed surface. The revealed face showed that the stain was uniform across the sample depth (~500 µm), confirming that the artifact in **a** was indeed the Inner Filter Effect. Scale bar: 100 µm (a,b).

Uneven signal is mostly an issue with thick sample labeling and could be a result from excess dye during a labeling reaction. A thick sample can be labeled so strongly at the surface that the excitation light in the microscope is substantially attenuated within the interior of the sample, producing a very bright surface but an apparent dimmer interior, even if the sample itself is in fact labeled uniformly. The researcher can section the hydrogel or the thick sample and image the cross-section to assess the sample uniformity without this complication. (**Fig. 4.4**) If the stain is indeed uniform, the researcher can stain a new sample with a more dilute dye to produce a dimmer stain that avoids this so-called “inner filter effect”. (**Fig. 4.4**) If the stain is in fact enriched at the surface, the researchers should confirm that the NHS-dye coupling reaction is performed at the proper pH of 7.4 or could consider preparing the NHS-dye stock in ~100 mM MES buffer at pH 6.0 to slow down the hydrolysis and coupling reactions while also providing

more time for the labeling reaction and dye penetration. In addition, to aid in the penetration of the dye through the negatively charged hydrogel, researchers can consider using NaCl to act as shield to improve charged reactants diffusion into the gel. Researchers should also make sure that the tissue sample is not attached to the surface of the container during incubation (**Fig. 4.3**) and to ensure continuous sample displacement and exposure to incubation solution during gentle agitation. Using a lower concentration of dye may also help improve the uniformity of labeling, but possibly at the cost of decreasing the brightness of the stain.

4.5.5 Issues with Overly Bright Signal

Crosstalk from an overly bright signal in a channel could swamp a weaker signal from a different spectral channel. In addition, an overly bright signal can produce inner filter effect. (**Section 4.5.4**) Overly bright signals can arise due to several reasons. First, insufficient washing could prevent unconjugated dyes from being removed from the sample resulting in very bright signals. Washing the sample extensively can fix this problem and improve contrast. Second, if the dye concentration is too high, an overly bright sample may be produced and lowering the concentration of dye(s) in the coupling reaction(s) can help tune the signal.

4.5.6 Issues with Poor Transparency

Poor transparency can be caused by improper or insufficient tissue clearing. First, this may be caused by inadequate dehydration prior to incubation with ethyl cinnamate (EC) or other common refractive index oil. A thorough dehydration is crucial to achieve a uniform refractive index match throughout the entire specimen thickness and extending the dehydration periods at each stage may help improve the clarity. Second, this may also be caused by insufficient incubation with EC, and the researcher can try to refresh the EC a couple of times, followed by waiting ~30-60 minutes or more (depending on the size of the tissue) for the tissue to become fully cleared and index-matched.

4.6 Discussion and Future Directions

4.6.1 Optimize oxidation to immunolabeling perturbation

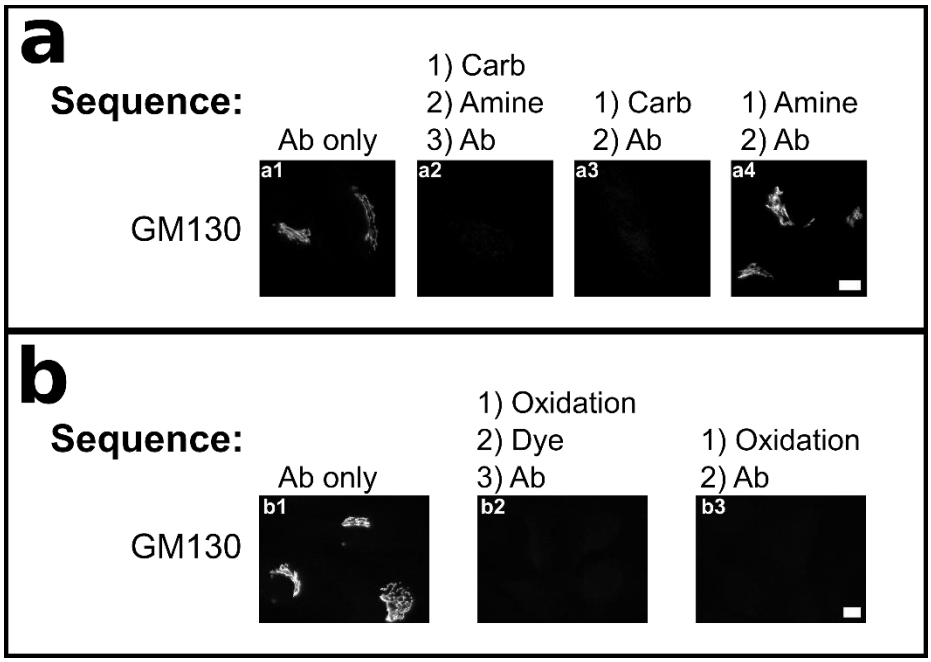

Fig. 4.5. Figure showing the effect of chemical stains on anti-GM130 antibody labeling on unexpanded RPE cells.

a) Effect of carbohydrate and amine stains on anti-GM130 labeling. b) Effect of carbohydrate oxidation and hydrazide-fluorophore labeling on anti-GM130 labeling. Scale bar: 10 µm (a1-a4,b1-b4). Figure a adapted from Mao *et al*.[165] Science Advances. Copyright AAAS Publishing Group. Creative Commons License can be found here.

Previously in Chapter 3, it was shown that a small fraction of antibodies are unable to efficiently bind their targets when immunostaining after the carbohydrate stain (**Fig. S3.8-3.9**), such as the anti-GM130 antibody that specifically targets the golgi apparatus. (**Fig. 4.5a**) Further tests of the carbohydrate labeling step on anti-GM130 antibodies and revealed that the periodate oxidation step in particular significantly reduced this antibody's affinity. (**Fig. 4.5b**) It is likely then that the breaking of carbohydrates using periodate oxidation caused the failure of the antibody to recognize the targeted site, and not the presence of the fluorophore obstructing the antibody binding. In order to reduce the disruption of antibody labeling, one could potentially try reducing the amount of oxidant used or selecting an even milder oxidant, but further validation

is required. Another solution could be to change the labeling sequence of the stains (**Section 4.6.2**).

4.6.2 Stain labeling sequence

In general, the preferred sequence for covalent chemical stains was: carbohydrate, amine, antibody. Because of the potential chemical bleaching of fluorophores by the periodate oxidation in the carbohydrate labeling step, it was preferable to do this step prior to amine or immunolabeling. In the unlikely case that the oxidation step interferes with a certain antibody binding, it would be preferable to do the carbohydrate labeling after the immunostain. In such cases, an oxidation-resistant label on the secondary antibodies such as biotin instead of a fluorophore would be useful, and a post fluorophore-conjugated streptavidin labeling can be done. The flexibility of the sequence was tested on expanded RPE cells and described in **Chapter 3**.

However, despite the flexibility, it was noted that the permeabilization step required for immunolabeling might induce some minor changes in the staining if all the chemical staining and immunolabeling were performed before gelation and expansion. For example, smaller details such as the nuclear pores by chemical stains may be not be as prominent if the chemical stains were done after immunolabeling. It could be a slight increase in accessibility by the dyes to other proteins after membrane disruption by detergent such as Triton X-100, resulting in higher background thus reducing contrast. While the effect is minor, researchers are recommended to be cautious. On another note, this observation could lead to potential further optimization on stain differentiation using a combination of different dye (hydrophilic versus hydrophobic), solvent and sample conditions (pH, metals, organic solvents), even though initial analysis did not show any significant differences in the resulting stain between using a hydrophilic and a hydrophobic dye.

4.6.3 Effects of fixatives

One feature of FLARE is that it shows the general physiology of the sample extremely well so any perturbation in the sample processing is shown prominently. Thus, this staining method

is effective in informing researchers about the physical outcome of a certain kind of sample preparation. The following example shows the result of using different fixation chemistry. (**Fig. 4.6**) Most of the expanded cell sample in **Chapter 3** uses either 4% PFA or a combination of 3.2% PFA+0.1% GA (**Fig. 4.5a-d**). A change in fixative process to a glyoxal[164] cocktail provides a different cell image even though the expansion and staining process were the same. (**Fig. 4.5e-h**)

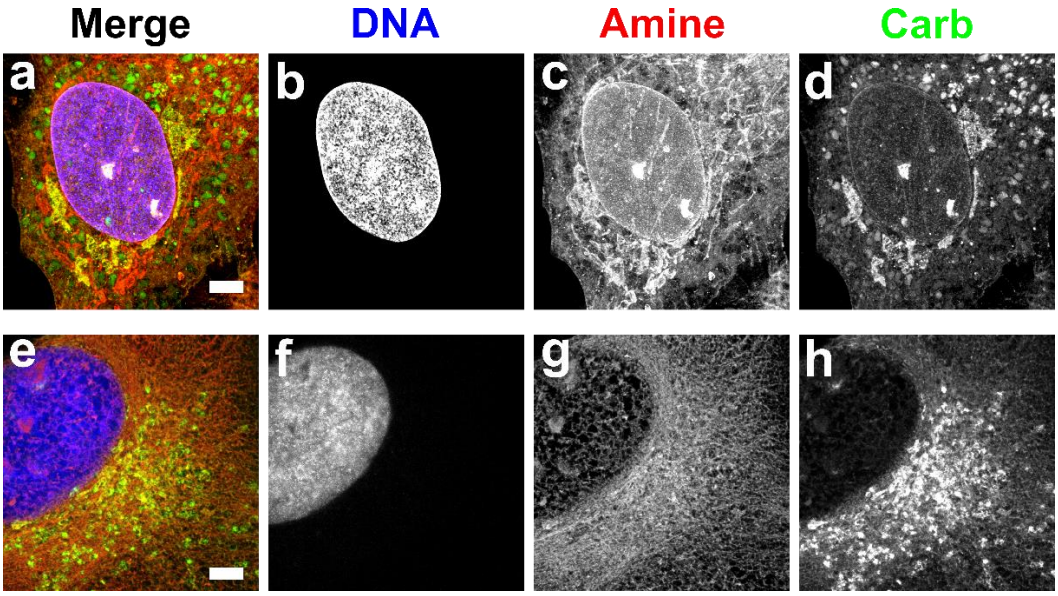

Fig. 4.6. Comparison of FLARE stained expanded RPE cells.

a-d) RPE cells fixed with 3.2% PFA and 0.1% GA which retained cytoskeletal and membrane organelles well. e-h) RPE cells fixed with a glyoxal cocktail which did not retain certain membrane organelles properly, such as mitochondria, but allowed NHS-ester to stain certain structures more prominently such as endoplasmic reticulum and looked visibly different from the cell in a-d. Scale bar (pre-expansion): 3 µm (a-h). Figure a-d adapted from Mao *et al*.[165] Science Advances. Copyright AAAS Publishing Group. Creative Commons License can be found here.

4.6.4 Expand range of chemical targets and chemistry used

FLARE demonstrated the utility in targeting amines and oxidized carbohydrates that are highly abundant in biological specimens. The utility of this amine labeling method was also corroborated by recently published work.[103,115] In particular, M'Saad and Bewersdorf[103] further showed that using maleimide to target cysteines enabled nanoscale visualization of the golgi complex in an double expandable hydrogel that can be expanded ~13-21 fold, instead of the regular ~4 fold. Although amine labeling has been used and validated with NHS-esters, there are

a variety of chemistry reactions developed to target amines,[166] such as isothiocyanates. For example, these various amine chemistries have different coupling and hydrolysis rates[167] and exploration of a variety of such chemistries might yield a better labeling technique than the NHS-ester which tends to be relatively quick and can be harder to control.

The carboxylic acid is also another possible functional group to target but could pose difficulties as the swellable polymer used in expansion contains a high density of carboxylic acids. Any potential chemical modification that could be applied to amino acid side chains and uses mild reagent and conditions are ideal candidates. Exploration of reactions beyond organic reactions, such as inorganic reactions, could yield potentially interesting outcomes. In addition, while challenging, developing mild reactions that could selectively target different types of carbohydrates would improve the stain contrast.

4.6.5 Turn-on probes and Cleavable linkers

The current method used stable covalent bonds and probes that were inherently fluorescent, which may have some potential drawbacks. Firstly, a perpetually fluorescent probe requires adequate washing to ensure that all unattached probes are sufficiently removed. Secondly, stable covalent attachment to a certain fluorophore limits the number of channels that can be used, resulting in inflexibility. The ability to design a turn-on probe, such as rhodamine-based fluorogenic aldehyde sensor,[168] would remove the need for a wash step, thus speeding up the staining process. The power of using cleavable linkers, such as the established disulfide cleavable linker, would allow multiple rounds of imaging using the same channel for different targets, enhancing multiplexing capabilities.

4.7 Conclusion

FLARE has proven valuable in the fluorescence labeling toolkit that produces reliable and bright well-contrasted stains. The staining procedure is simple, and the probes used are easily obtainable commercially. While most of the difficulties faced are easy to troubleshoot, some require further investigation. This method of covalently targeting chemical functional groups on

biological samples is now established, but there remains considerable room for further exploration, improvement, and applications.

REFERENCES

1. Abbe, E. Beiträge zur Theorie des Mikroskops und der mikroskopischen Wahrnehmung: I. Die Construction von Mikroskopen auf Grund der Theorie. *Arch. Für Mikrosk. Anat.* **9**, 413–418 (1873).
2. Zernike, F. How I Discovered Phase Contrast. *Science* **121**, 345–349 (1955).
3. Zernike, G. F. Phase Contrast, A New Method for the Microscopic Observation of Transparent Objects. *Physica* **9**, 686–698 (1942).
4. Schmidt, W. J. Doppelbrechung der Kernspindel und Zugfasertheorie der Chromosomenbewegung. *Chromosoma* **1**, 253–264 (1939).
5. Nomarski, G. & Weill, A. R. Application à la métallographie des méthodes interférentielles à deux ondes polarisées. *Rev. Métallurgie* **52**, 121–134 (1955).
6. Heimstädt, O. Das Fluoreszenzmikroskop. *Z. Für Wiss. Mikrosk. Mikrosk. Tech.* **28**, 330–337 (1911).
7. Ploem, J. S. The use of a vertical illuminator with interchangeable dichroic mirrors for fluorescence microscopy with incident light. *Z. Für Wiss. Mikrosk. Mikrosk. Tech.* **68**, 129–142 (1967).
8. Stokes, G. G. XVI. On the Change of Refrangibility of Light - No. II. *Philos. Trans.* **143**, 385–396 (1853).
9. Valeur, B. & Berberan-Santos, M. N. A Brief History of Fluorescence and Phosphorescence before the Emergence of Quantum Theory. *J. Chem. Educ.* **88**, 731–738 (2011).

10. Titford, M. Progress in the Development of Microscopical Techniques for Diagnostic Pathology. *J. Histotechnol.* **32**, 9–19 (2009).

11. Baeyer, A. Ueber eine neue Klasse von Farbstoffen. *Berichte Dtsch. Chem. Ges.* **4**, 555–558 (1871).

12. McKAY, I. C. & Forman, D. A comparison of fluorescein isothiocyanate and lissamine rhodamine (RB 200) as labels for antibody in the fluorescent antibody technique. 12.

13. Grimm, J. B. *et al.* A general method to improve fluorophores for live-cell and single-molecule microscopy. *Nat. Methods* **12**, 244–250 (2015).

14. Grimm, J. B. *et al.* A general method to fine-tune fluorophores for live-cell and in vivo imaging. *Nat. Methods* **14**, 987–994 (2017).

15. Hamer, F. M. The cyanine dyes. *Q. Rev. Chem. Soc.* **4**, 327 (1950).

16. Mujumdar, R. B., Ernst, L. A., Mujumdar, S. R., Lewis, C. J. & Waggoner, A. S. Cyanine dye labeling reagents: sulfoindocyanine succinimidyl esters. *Bioconjug. Chem.* **4**, 105–111 (1993).

17. Waggoner, A. & Mujumdar, R. Rigidized trimethine cyanine dyes.

18. Ernst, L. A., Gupta, R. K., Mujumdar, R. B. & Waggoner, A. S. Cyanine dye labeling reagents for sulfhydryl groups. *Cytometry* **10**, 3–10 (1989).

19. Southwick, P. L. *et al.* Cyanine dye labeling reagents—carboxymethylindocyanine succinimidyl esters. *Cytometry* **11**, 418–430 (1990).

20. Mujumdar, S. R., Mujumdar, R. B., Grant, C. M. & Waggoner, A. S. Cyanine-labeling reagents: sulfobenzindocyanine succinimidyl esters. *Bioconjug. Chem.* **7**, 356–362 (1996).

21. Dempsey, G. T., Vaughan, J. C., Chen, K. H., Bates, M. & Zhuang, X. Evaluation of fluorophores for optimal performance in localization-based super-resolution imaging. *Nat. Methods* **8**, 1027–1036 (2011).

22. Treibs, A. & Kreuzer, F.-H. Difluorboryl-Komplexe von Di- und Tripyrrylmethenen. *Justus Liebigs Ann. Chem.* **718**, 208–223 (1968).

23. Loudet, A. & Burgess, K. BODIPY Dyes and Their Derivatives: Syntheses and Spectroscopic Properties. *Chem. Rev.* **107**, 4891–4932 (2007).

24. Squeo, B. M. & Pasini, M. BODIPY platform: a tunable tool for green to NIR OLEDs. *Supramol. Chem.* **32**, 56–70 (2020).

25. Fan, G., Yang, L. & Chen, Z. Water-soluble BODIPY and aza-BODIPY dyes: synthetic progress and applications. *Front. Chem. Sci. Eng.* **8**, 405–417 (2014).

26. Rampersad, S. N. Multiple Applications of Alamar Blue as an Indicator of Metabolic Function and Cellular Health in Cell Viability Bioassays. *Sensors* **12**, 12347–12360 (2012).

27. Fan, Y., Hao, R., Han, C. & Zhang, B. Counting Single Redox Molecules in a Nanoscale Electrochemical Cell. *Anal. Chem.* **90**, 13837–13841 (2018).

28. Lavis, L. D. & Raines, R. T. Bright Building Blocks for Chemical Biology. *ACS Chem. Biol.* **9**, 855–866 (2014).

29. Cordes, T., Vogelsang, J. & Tinnefeld, P. On the mechanism of trolox as antiblinking and antibleaching reagent. *J. Am. Chem. Soc.* **131**, 5018–5019 (2009).

30. Rasnik, I., McKinney, S. A. & Ha, T. Nonblinking and long-lasting single-molecule fluorescence imaging. *Nat Meth* **3**, 891–893 (2006).

31. Vogelsang, J. *et al.* A Reducing and Oxidizing System Minimizes Photobleaching and Blinking of Fluorescent Dyes. *Angew. Chem. Int. Ed.* **47**, 5465–5469 (2008).

32. Harada, Y., Sakurada, K., Aoki, T., Thomas, D. D. & Yanagida, T. Mechanochemical coupling in actomyosin energy transduction studied by in vitro movement assay. *J. Mol. Biol.* **216**, 49–68 (1990).

33. Swoboda, M. *et al.* Enzymatic Oxygen Scavenging for Photostability without pH Drop in Single-Molecule Experiments. *ACS Nano* **6**, 6364–6369 (2012).

34. Longin, A., Souchier, C., Ffrench, M. & Bryon, P. A. Comparison of anti-fading agents used in fluorescence microscopy: image analysis and laser confocal microscopy study. *J. Histochem. Cytochem.* **41**, 1833–1840 (1993).

35. Coons, A. H., Creech, H. J. & Jones, R. N. Immunological Properties of an Antibody Containing a Fluorescent Group. *Exp. Biol. Med.* **47**, 200–202 (1941).

36. Hermanson, Greg. *Bioconjugate Techniques, 2nd Edition*.

37. Bradbury, A. & Plückthun, A. Reproducibility: Standardize antibodies used in research. *Nature* **518**, 27–29 (2015).

38. Shimomura, O., Johnson, F. H. & Saiga, Y. Extraction. Purification and Properties of Aequorin, a Bioluminescent Protein from the Luminous Hydromedusan. Aequorea'. *J. Cell. Comp. Physiol.* **59**, 223–239 (1962).

39. Chalfie, M., Tu, Y., Euskirchen, G., Ward, W. W. & Prasher, D. C. Green fluorescent protein as a marker for gene expression. *Science* **263**, 802–805 (1994).

40. Heim, R., Prasher, D. C. & Tsien, R. Y. Wavelength mutations and posttranslational autoxidation of green fluorescent protein. *Proc. Natl. Acad. Sci.* **91**, 12501–12504 (1994).

41. Campbell, R. E. *et al.* A monomeric red fluorescent protein. *Proc. Natl. Acad. Sci.* **99**, 7877–7882 (2002).

42. Shaner, N. C. *et al.* Improved monomeric red, orange and yellow fluorescent proteins derived from Discosoma sp. red fluorescent protein. *Nat. Biotechnol.* **22**, 1567–1572 (2004).

43. Wiedenmann, J. *et al.* A far-red fluorescent protein with fast maturation and reduced oligomerization tendency from Entacmaea quadricolor (Anthozoa, Actinaria). *Proc. Natl. Acad. Sci.* **99**, 11646–11651 (2002).

44. Merzlyak, E. M. *et al.* Bright monomeric red fluorescent protein with an extended fluorescence lifetime. *Nat. Methods* **4**, 555–557 (2007).

45. Shcherbo, D. *et al.* Bright far-red fluorescent protein for whole-body imaging. *Nat. Methods* **4**, 741–746 (2007).

46. Kredel, S. *et al.* mRuby, a Bright Monomeric Red Fluorescent Protein for Labeling of Subcellular Structures. *PLoS ONE* **4**, e4391 (2009).

47. Rodriguez, E. A. *et al.* The Growing and Glowing Toolbox of Fluorescent and Photoactive Proteins. *Trends Biochem. Sci.* **42**, 111–129 (2017).

48. Dickson, R. M., Cubitt, A. B., Tsien, R. Y. & Moerner, W. E. On/off blinking and switching behaviour of single molecules of green fluorescent protein. *Nature* **388**, 355–358 (1997).

49. Habuchi, S. *et al.* Evidence for the Isomerization and Decarboxylation in the Photoconversion of the Red Fluorescent Protein DsRed. *J. Am. Chem. Soc.* **127**, 8977–8984 (2005).

50. Andresen, M. *et al.* Structure and mechanism of the reversible photoswitch of a fluorescent protein. *Proc. Natl. Acad. Sci. U. S. A.* **102**, 13070–13074 (2005).

51. Patterson, G. H. & Lippincott-Schwartz, J. A Photoactivatable GFP for Selective Photolabeling of Proteins and Cells. *Science* **297**, 1873–1877 (2002).

52. Toga, A. W., Ambach, K. L. & Schluender, S. High-Resolution Anatomy from in Situ Human Brain. *NeuroImage* **1**, 334–344 (1994).

53. Minsky, M. Memoir on inventing the confocal scanning microscope. *Scanning* **10**, 128–138 (1988).

54. Siedentopf, H. & Zsigmondy, R. Uber Sichtbarmachung und Größenbestimmung ultramikoskopischer Teilchen, mit besonderer Anwendung auf Goldrubingläser. *Ann. Phys.* **315**, 1–39 (1902).

55. Voie, A. H., Burns, D. H. & Spelman, F. A. Orthogonal-plane fluorescence optical sectioning: Three-dimensional imaging of macroscopic biological specimens. *J. Microsc.* **170**, 229–236 (1993).

56. Huisken, J. Optical Sectioning Deep Inside Live Embryos by Selective Plane Illumination Microscopy. *Science* **305**, 1007–1009 (2004).

57. Huisken, J. & Stainier, D. Y. R. Selective plane illumination microscopy techniques in developmental biology. *Development* **136**, 1963–1975 (2009).

58. Chen, B.-C. *et al.* Lattice light-sheet microscopy: Imaging molecules to embryos at high spatiotemporal resolution. *Science* **346**, 1257998–1257998 (2014).

59. Richardson, D. S. & Lichtman, J. W. Clarifying Tissue Clearing. *Cell* **162**, 246–257 (2015).

60. Iwadare, T., Mori, H., Ishiguro, K. & Takeishi, M. Dimensional changes of tissues in the course of processing. *J. Microsc.* **136**, 323–327 (1984).

61. Dodt, H.-U. *et al.* Ultramicroscopy: three-dimensional visualization of neuronal networks in the whole mouse brain. *Nat. Methods* **4**, 331–336 (2007).

62. Becker, K., Jährling, N., Saghafi, S., Weiler, R. & Dodt, H.-U. Chemical Clearing and Dehydration of GFP Expressing Mouse Brains. *PLoS ONE* **7**, e33916 (2012).

63. Renier, N. *et al.* iDISCO: A Simple, Rapid Method to Immunolabel Large Tissue Samples for Volume Imaging. *Cell* **159**, 896–910 (2014).

64. Azaripour, A. *et al.* A survey of clearing techniques for 3D imaging of tissues with special reference to connective tissue. *Prog. Histochem. Cytochem.* **51**, 9–23 (2016).

65. Klingberg, A. *et al.* Fully Automated Evaluation of Total Glomerular Number and Capillary Tuft Size in Nephritic Kidneys Using Lightsheet Microscopy. *J. Am. Soc. Nephrol.* **28**, 452–459 (2017).

66. Ertürk, A. *et al.* Three-dimensional imaging of solvent-cleared organs using 3DISCO. *Nat. Protoc.* **7**, 1983–1995 (2012).

67. Meglinski, I. V., Bashkatov, A. N., Genina, E. A., Churmakov, D. Y. & Tuchin, V. V. The Enhancement of Confocal Images of Tissues at Bulk Optical Immersion. 5.

68. Ke, M.-T., Fujimoto, S. & Imai, T. SeeDB: a simple and morphology-preserving optical clearing agent for neuronal circuit reconstruction. *Nat. Neurosci.* **16**, 1154–1161 (2013).

69. Tsai, P. S. *et al.* Correlations of Neuronal and Microvascular Densities in Murine Cortex Revealed by Direct Counting and Colocalization of Nuclei and Vessels. *J. Neurosci.* **29**, 14553–14570 (2009).

70. Kuwajima, T. *et al.* ClearT: a detergent- and solvent-free clearing method for neuronal and non-neuronal tissue. *Development* **140**, 1364–1368 (2013).

71. Staudt, T., Lang, M. C., Medda, R., Engelhardt, J. & Hell, S. W. 2,2'-Thiodiethanol: A new water soluble mounting medium for high resolution optical microscopy. *Microsc. Res. Tech.* **70**, 1–9 (2007).

72. Aoyagi, Y., Kawakami, R., Osanai, H., Hibi, T. & Nemoto, T. A Rapid Optical Clearing Protocol Using 2,2'-Thiodiethanol for Microscopic Observation of Fixed Mouse Brain. *PLOS ONE* **10**, e0116280 (2015).

73. Costantini, I. *et al.* A versatile clearing agent for multi-modal brain imaging. *Sci. Rep.* **5**, 9808 (2015).

74. Yang, B. *et al.* Single-Cell Phenotyping within Transparent Intact Tissue through Whole-Body Clearing. *Cell* **158**, 945–958 (2014).

75. Hama, H. *et al.* Scale: a chemical approach for fluorescence imaging and reconstruction of transparent mouse brain. *Nat. Neurosci.* **14**, 1481–1488 (2011).

76. Susaki, E. A. *et al.* Whole-Brain Imaging with Single-Cell Resolution Using Chemical Cocktails and Computational Analysis. *Cell* **157**, 726–739 (2014).

77. Chung, K. *et al.* Structural and molecular interrogation of intact biological systems. *Nature* **497**, 332–337 (2013).

78. Yun, D. H. *et al. Ultrafast immunostaining of organ-scale tissues for scalable proteomic phenotyping*. http://biorxiv.org/lookup/doi/10.1101/660373 (2019) doi:10.1101/660373.

79. Betzig, E. *et al.* Imaging intracellular fluorescent proteins at nanometer resolution. *Science* **313**, 1642–1645 (2006).

80. Rust, M. J., Bates, M. & Zhuang, X. Sub-diffraction-limit imaging by stochastic optical reconstruction microscopy (STORM). *Nat. Methods* **3**, 793–796 (2006).

81. Wildanger, D., Medda, R., Kastrup, L. & Hell, S. W. A compact STED microscope providing 3D nanoscale resolution. *J. Microsc.* **236**, 35–43 (2009).

82. Gustafsson, M. G. Surpassing the lateral resolution limit by a factor of two using structured illumination microscopy. *J. Microsc.* **198**, 82–87 (2000).

83. Chen, F., Tillberg, P. W. & Boyden, E. S. Expansion microscopy. *Science* **347**, 543–548 (2015).

84. Dempsey, G. T. *et al.* Photoswitching Mechanism of Cyanine Dyes. *J. Am. Chem. Soc.* **131**, 18192–18193 (2009).

85. Vaughan, J. C., Dempsey, G. T., Sun, E. & Zhuang, X. Phosphine quenching of cyanine dyes as a versatile tool for fluorescence microscopy. *J. Am. Chem. Soc.* **135**, 1197–1200 (2013).

86. Vaughan, J. C., Jia, S. & Zhuang, X. Ultrabright photoactivatable fluorophores created by reductive caging. *Nat Methods* **9**, 1181–1184 (2012).

87. Ando, R., Hama, H., Yamamoto-Hino, M., Mizuno, H. & Miyawaki, A. An optical marker based on the UV-induced green-to-red photoconversion of a fluorescent protein. *Proc. Natl. Acad. Sci.* **99**, 12651–12656 (2002).

88. Burns, D. H., Callis, J. B., Christian, G. D. & Davidson, E. R. Strategies for attaining superresolution using spectroscopic data as constraints. *Appl. Opt.* **24**, 154–161 (1985).

89. Betzig, E. Proposed method for molecular optical imaging. *Opt. Lett.* **20**, 237–239 (1995).

90. Heilemann, M., Margeat, E., Kasper, R., Sauer, M. & Tinnefeld, P. Carbocyanine Dyes as Efficient Reversible Single-Molecule Optical Switch. *J. Am. Chem. Soc.* **127**, 3801–3806 (2005).

91. Bates, M., Blosser, T. & Zhuang, X. Short-Range Spectroscopic Ruler Based on a Single-Molecule Optical Switch. *Phys. Rev. Lett.* **94**, 108101 (2005).

92. Klar, T. A. & Hell, S. W. Subdiffraction resolution in far-field fluorescence microscopy. *Opt. Lett.* **24**, 954–956 (1999).

93. Klar, T. A., Jakobs, S., Dyba, M., Egner, A. & Hell, S. W. Fluorescence microscopy with diffraction resolution barrier broken by stimulated emission. *Proc. Natl. Acad. Sci.* **97**, 8206–8210 (2000).

94. Hell, S. W. & Wichmann, J. Breaking the diffraction resolution limit by stimulated emission: stimulated-emission-depletion fluorescence microscopy. *Opt. Lett.* **19**, 780–782 (1994).

95. Bailey, B., Farkas, D. L., Taylor, D. L. & Lanni, F. Enhancement of axial resolution in fluorescence microscopy by standing-wave excitation. (1993).

96. Heintzmann, R. & Cremer, C. G. Laterally modulated excitation microscopy: improvement of resolution by using a diffraction grating. in (eds. Bigio, I. J., Schneckenburger, H., Slavik, J., Svanberg, K. & Viallet, P. M.) 185–196 (1999). doi:10.1117/12.336833.

97. Heintzmann, R. & Huser, T. Super-Resolution Structured Illumination Microscopy. *Chem. Rev.* **117**, 13890–13908 (2017).

98. Chozinski, T. J. *et al.* Expansion microscopy with conventional antibodies and fluorescent proteins. *Nat. Methods* **13**, 485–488 (2016).

99. Tillberg, P. W. *et al.* Protein-retention expansion microscopy of cells and tissues labeled using standard fluorescent proteins and antibodies. *Nat. Biotechnol.* **34**, 987–992 (2016).

100. Ku, T. *et al.* Multiplexed and scalable super-resolution imaging of three-dimensional protein localization in size-adjustable tissues. *Nat. Biotechnol.* **34**, 973–981 (2016).

101. Chang, J.-B. *et al.* Iterative expansion microscopy. *Nat. Methods* **14**, 593–599 (2017).

102. Gambarotto, D. *et al.* Imaging cellular ultrastructures using expansion microscopy (U-ExM). *Nat. Methods* **16**, 71–74 (2019).

103. M'Saad, O. & Bewersdorf, J. Light microscopy of proteins in their ultrastructural context. *Nat. Commun.* **11**, 3850 (2020).

104. Alon, S. *et al. Expansion Sequencing: Spatially Precise* In Situ *Transcriptomics in Intact Biological Systems*. http://biorxiv.org/lookup/doi/10.1101/2020.05.13.094268 (2020) doi:10.1101/2020.05.13.094268.

105. Chen, F. *et al.* Nanoscale imaging of RNA with expansion microscopy. *Nat. Methods* **13**, 679–684 (2016).

106. Gao, M. *et al.* Expansion Stimulated Emission Depletion Microscopy (ExSTED). *ACS Nano* (2018) doi:10.1021/acsnano.8b00776.

107. Pernal, S. P. *et al.* Differential expansion microscopy. *bioRxiv* 699579 (2019) doi:10.1101/699579.

108. Chozinski, T. J. *et al.* Volumetric, Nanoscale Optical Imaging of Mouse and Human Kidney via Expansion Microscopy. *Sci. Rep.* **8**, (2018).

109. Halpern, A. R., Alas, G. C. M., Chozinski, T. J., Paredez, A. R. & Vaughan, J. C. Hybrid Structured Illumination Expansion Microscopy Reveals Microbial Cytoskeleton Organization. *ACS Nano* **11**, 12677–12686 (2017).

110. Jiang, N. *et al.* Superresolution imaging of *Drosophila* tissues using expansion microscopy. *Mol. Biol. Cell* **29**, 1413–1421 (2018).

111. Freifeld, L. *et al.* Expansion microscopy of zebrafish for neuroscience and developmental biology studies. *Proc. Natl. Acad. Sci.* 201706281 (2017) doi:10.1073/pnas.1706281114.

112. Unnersjö-Jess, D. *et al.* Confocal super-resolution imaging of the glomeruluar filtration barrier enables by tissue expansion. *Kidney Int.* (2017) doi:https://doi.org/10.1016/j.kint.2017.09.019.

113. Cahoon, C. K. *et al.* Superresolution expansion microscopy reveals the three-dimensional organization of the *Drosophila* synaptonemal complex. *Proc. Natl. Acad. Sci.* **114**, E6857–E6866 (2017).

114. Cainero, I. *et al.* Combining Expansion Microscopy and STED Nanoscopy for the Study of Cellular Organization. *Biophys. J.* **112**, 140a (2017).

115. Yu, C.-C. (Jay) *et al.* Expansion microscopy of C. elegans. *eLife* **9**, (2020).

116. Shim, S. H. *et al.* Super-resolution fluorescence imaging of organelles in live cells with photoswitchable membrane probes. *Proc. Natl. Acad. Sci.* **109**, 13978–13983 (2012).

117. Nägerl, U. V., Willig, K. I., Hein, B., Hell, S. W. & Bonhoeffer, T. Live-cell imaging of dendritic spines by STED microscopy. *Proc. Natl. Acad. Sci.* **105**, 18982–18987 (2008).

118. Stephan, T., Roesch, A., Riedel, D. & Jakobs, S. Live-cell STED nanoscopy of mitochondrial cristae. *Sci. Rep.* **9**, 12419 (2019).

119. Demmerle, J. *et al.* Strategic and practical guidelines for successful structured illumination microscopy. *Nat. Protoc.* **12**, 988–1010 (2017).

120. Rusk, N. The fluorescence microscope: First fluorescence microscope, First epifluorescence microscope, The dichroic mirror. *Nat. Cell Biol.* **11**, S8–S9 (2009).

121. Sjöback, R., Nygren, J. & Kubista, M. Absorption and fluorescence properties of fluorescein. *Spectrochim. Acta. A. Mol. Biomol. Spectrosc.* **51**, L7–L21 (1995).

122. Liu, M. *et al.* A coumarin-based fluorescent turn-on probe for detection of biothiols in vitro: Coumarin-based probe for the detection of biothiols. *Luminescence* **30**, 1395–1402 (2015).

123. Puente-Muñoz, V. *et al.* New Thiol-Sensitive Dye Application for Measuring Oxidative Stress in Cell Cultures. *Sci. Rep.* **9**, 1659 (2019).

124. Li, L.-L. *et al.* A near-infrared water-soluble fluorescent probe for the detection of biothiols in living cells and *Escherichia coli*. *Anal. Methods* **11**, 821–826 (2019).

125. Kuimova, M. K. Mapping viscosity in cells using molecular rotors. *Phys. Chem. Chem. Phys.* **14**, 12671 (2012).

126. Li, W. & Zheng, G. Photoactivatable fluorophores and techniques for biological imaging applications. *Photochem. Photobiol. Sci.* **11**, 460 (2012).

127. Grimm, J. B. *et al.* Bright photoactivatable fluorophores for single-molecule imaging. *Nat. Methods* **13**, 985–988 (2016).

128. Paige, J. S., Wu, K. Y. & Jaffrey, S. R. RNA Mimics of Green Fluorescent Protein. *Science* **333**, 642–646 (2011).

129. Würth, C., Grabolle, M., Pauli, J., Spieles, M. & Resch-Genger, U. Relative and absolute determination of fluorescence quantum yields of transparent samples. *Nat. Protoc.* **8**, 1535–1550 (2013).

130. Olmsted, John. Calorimetric determinations of absolute fluorescence quantum yields. *J. Phys. Chem.* **83**, 2581–2584 (1979).

131. Song, W., Strack, R. L., Svensen, N. & Jaffrey, S. R. Plug-and-Play Fluorophores Extend the Spectral Properties of Spinach. *J. Am. Chem. Soc.* (2014).

132. Shaner, N. C., Steinbach, P. A. & Tsien, R. Y. A guide to choosing fluorescent proteins. *Nat. Methods* **2**, 905–909 (2005).

133. Plamont, M.-A. *et al.* Small fluorescence-activating and absorption-shifting tag for tunable protein imaging in vivo. *Proc. Natl. Acad. Sci.* **113**, 497–502 (2016).

134. Klima, J. C. *et al.* Incorporation of Sensing Modalities Into De Novo Designed Fluorescence-activating Proteins. *Rev. Nat. Chem. Biol.* (2020).

135. Sahl, S. J., Hell, S. W. & Jakobs, S. Fluorescence nanoscopy in cell biology. *Nat. Rev. Mol. Cell Biol.* **18**, 685–701 (2017).

136. Sigal, Y. M., Zhou, R. & Zhuang, X. Visualizing and discovering cellular structures with super-resolution microscopy. *Science* **361**, 880–887 (2018).

137. Tainaka, K., Kuno, A., Kubota, S. I., Murakami, T. & Ueda, H. R. Chemical Principles in Tissue Clearing and Staining Protocols for Whole-Body Cell Profiling. *Annu. Rev. Cell Dev. Biol.* **32**, 713–741 (2016).

138. Schermelleh, L. *et al.* Super-resolution microscopy demystified. *Nat. Cell Biol.* **21**, 72–84 (2019).

139. Schnell, U., Dijk, F., Sjollema, K. A. & Giepmans, B. N. G. Immunolabeling artifacts and the need for live-cell imaging. *Nat. Methods* **9**, 152–158 (2012).

140. *Theory and practice of histological techniques*. (Elsevier Churchill Livingston, 2013).

141. Elfer, K. N. *et al.* DRAQ5 and Eosin ('D&E') as an Analog to Hematoxylin and Eosin for Rapid Fluorescence Histology of Fresh Tissues. *PLOS ONE* **11**, e0165530 (2016).

142. Ornstein, L., Mautner, W. & Davis, B. new horizons in fluorescence microscopy. *1957* **24**, 1066.

143. Weinblatt, F. M., Shannon, W. A. & Seligman, A. M. A new fluorescent method for the demonstration of macromolecular aldehydes. *Histochemistry* **41**, 353–359 (1975).

144. Lomant, A. J. & Fairbanks, G. Chemical probes of extended biological structures: synthesis and properties of the cleavable protein cross-linking reagent [35S]dithiobis(succinimidyl propionate). *J. Mol. Biol.* **104**, 243–261 (1976).

145. Bragg, P. D. & Hou, C. Subunit composition, function, and spatial arrangement in the Ca2+- and Mg2+-activated adenosine triphosphatases of Escherichia coli and Salmonella typhimurium. *Arch. Biochem. Biophys.* **167**, 311–321 (1975).

146. Baskin, J. M., Dehnert, K. W., Laughlin, S. T., Amacher, S. L. & Bertozzi, C. R. Visualizing enveloping layer glycans during zebrafish early embryogenesis. *Proc. Natl. Acad. Sci.* **107**, 10360–10365 (2010).

147. Saitoh, Y. *et al.* Three-dimensional reconstruction of living mouse liver tissues using cryotechniques with confocal laser scanning microscopy. *J. Electron Microsc. (Tokyo)* **59**, 513–525 (2010).

148. Hill, D. E., Fetterer, R. H. & Urban, J. F. Biotin as a probe of the surface of Ascaris suum developmental stages. *Mol. Biochem. Parasitol.* **41**, 45–52 (1990).

149. Swirski, F. K. *et al.* A Near-Infrared Cell Tracker Reagent for Multiscopic In Vivo Imaging and Quantification of Leukocyte Immune Responses. *PLoS ONE* **2**, e1075 (2007).

150. Renier, N. *et al.* iDISCO: A Simple, Rapid Method to Immunolabel Large Tissue Samples for Volume Imaging. *Cell* **159**, 896–910 (2014).

151. Murray, E. *et al.* Simple, Scalable Proteomic Imaging for High-Dimensional Profiling of Intact Systems. *Cell* **163**, 1500–1514 (2015).

152. Glaser, A. K. *et al.* Multi-immersion open-top light-sheet microscope for high-throughput imaging of cleared tissues. *Nat. Commun.* **10**, 2781 (2019).

153. Giacomelli, M. G. *et al.* Virtual Hematoxylin and Eosin Transillumination Microscopy Using Epi-Fluorescence Imaging. *PLOS ONE* **11**, e0159337 (2016).

154. Fagerberg, L. *et al.* Mapping the Subcellular Protein Distribution in Three Human Cell Lines. *J. Proteome Res.* **10**, 3766–3777 (2011).

155. Itzhak, D. N., Tyanova, S., Cox, J. & Borner, G. H. Global, quantitative and dynamic mapping of protein subcellular localization. *eLife* **5**, e16950 (2016).

156. Pahari, S., Sun, L. & Alexov, E. PKAD: a database of experimentally measured pKa values of ionizable groups in proteins. *Database* **2019**, (2019).

157. Chen, Y. *et al.* Rapid pathology of lumpectomy margins with open-top light-sheet (OTLS) microscopy. *Biomed. Opt. Express* **10**, 1257 (2019).

158. Xie, W. *et al.* Microscopy with ultraviolet surface excitation for wide-area pathology of breast surgical margins. *J. Biomed. Opt.* **24**, 12 (2019).

159. Karagiannis, E. D. *et al. Expansion Microscopy of Lipid Membranes*. http://biorxiv.org/lookup/doi/10.1101/829903 (2019) doi:10.1101/829903.

160. Beliveau, B. J. *et al.* Versatile design and synthesis platform for visualizing genomes with Oligopaint FISH probes. *Proc. Natl. Acad. Sci.* **109**, 21301–21306 (2012).

161. Lehnertz, B. *et al.* Suv39h-Mediated Histone H3 Lysine 9 Methylation Directs DNA Methylation to Major Satellite Repeats at Pericentric Heterochromatin. *Curr. Biol.* **13**, 1192–1200 (2003).

162. Zhao, Y. *et al.* Nanoscale imaging of clinical specimens using pathology-optimized expansion microscopy. *Nat. Biotechnol.* (2017) doi:10.1038/nbt.3892.

163. Baker, M. Blame it on the antibodies. *Nature* **521**, 274–276 (2015).

164. Richter, K. N. *et al.* Glyoxal as an alternative fixative to formaldehyde in immunostaining and super-resolution microscopy. *EMBO J.* e201695709 (2017) doi:10.15252/embj.201695709.

165. Mao, C. *et al.* Feature-rich covalent stains for super-resolution and cleared tissue fluorescence microscopy. *Sci. Adv.* **6**, eaba4542 (2020).

166. *The molecular probes handbook: a guide to fluorescent probes and labeling technologies*. (Life Technologies, 2010).

167. Banks, P. R. & Paquette, D. M. Comparison of Three Common Amine Reactive Fluorescent Probes Used for Conjugation to Biomolecules by Capillary Zone Electrophoresis. *Bioconjug. Chem.* **6**, 447–458 (1995).

168. Li, Z., Xue, Z., Wu, Z., Han, J. & Han, S. Chromo-fluorogenic detection of aldehydes with a rhodamine based sensor featuring an intramolecular deoxylactam. *Org. Biomol. Chem.* **9**, 7652 (2011).

VITA

EDUCATION

University of Washington (UW) — Seattle, WA, USA
PhD in Chemistry GPA 3.92 — Expected Aug 2020
M. Sc in Chemistry — Sept 2014 – Jul 2016

Nanyang Technological University — Singapore
B. Sc (1st Hons) in Chemistry and Biological Chemistry — Jul 2007 – Jul 2011

RESEARCH EXPERIENCE

University of Washington Chemistry Department — Seattle, WA, USA
Doctoral Research, PhD Candidate — Dec 2014 – Aug 2020
Advisor: Professor Joshua Vaughan

Agency for Science, Technology and Research, Molecular Engineering Lab — Singapore
Post-graduate Research, Research Officer — Sept 2011 – Jul 2014
Employer and Advisor: Dr. Yin Nah Teo and Professor Sydney Brenner

Nanyang Technological University Chemistry Division — Singapore
Undergraduate Research, Undergraduate student — 2008 – 2011
Advisor: Professor Teck Peng Loh

University of Warwick Chemistry Department — UK
Undergraduate Research, Visiting Student — Oct – Dec 2009
Advisor: Professor Paul Taylor

PUBLICATIONS AND PATENT

Halpern AR, **Lee MY**, Vaughan JC. Low-cost customizable DIY spinning disk confocal microscopy for volumetric imaging and localization microscopy. **2020** (*In preparation*)

Klima JC, Doyle LA, Lee JH, Rappleye M, Gagnon LA, **Lee MY**, Barros EP, Vorobieva AA, Dou J, Bremner S, Quon J, Chow CM, Carter L, Mack DL, Amaro RE, Vaughan JC, Berndt A, Stoddard BL, Baker D. Incorporation of Sensing Modalities Into De *novo* Designed Fluorescence-activating Proteins. *Nat. Commun.* **2020** (*Accepted*)

Mao C*, **Lee MY***, Jhan J, Halpern AR, Woodworth MA, Glaser AK, Chozinski TJ, Shin L, Pippin JW, Shankland SJ, Liu JTC, Vaughan JC. Feature-rich Covalent Stains for Super-resolution and Cleared-tissue Fluorescence Microscopy. *Sci. Adv.*, **2020,** *6*, eaba4542.

Dou J*, Vorobieva AA*, Sheffler W, Doyle LA, Park H, Bick MJ, Mao B, Foight GW, **Lee MY**, Gagnon LA, Carter L, Sankaran B., Ovchinnikov S, Marcos E, Huang P, Vaughan JC, Stoddard BL, Baker D. De *novo* design of a fluorescence-activating beta barrel. *Nature*, **2018**, *561*, 485.

Goh WL*, **Lee MY***, Joseph TL, Lim TX, Chua J, Brenner S, Ghadessy FJ, Teo YN. A novel molecular rotor facilitates detection of p53-DNA interactions using the Fluorescent Intercalator Displacement Assay. *Nat. Sci. Rep.*, **2018**, *8*, 12946.

Goh WL*, **Lee MY***, Joseph TL, Quah ST, Brown CJ, Verma C, Brenner S, Ghadessy FJ, Teo YN. Molecular rotors as conditionally fluorescent labels for rapid detection of biomolecular interactions. *J. Am. Chem. Soc.*, **2014**, *136*, 6159.

Sydney Brenner, Yin Nah Teo, Farid Ghadessy, Leng Peng Walter Goh, **Min Yen Lee**.; "Fluorescent molecular rotors", US Patent 9863937B2, Jan 9 2018.

***contributed equally**

AWARDS

University of Washington — Seattle, WA, USA
Raymond And Sally Paxton Endowed Fund in Chemistry — 2017

CONFERENCES

Biophysical Society Annual Meeting — San Diego, CA, USA
Poster "Feature-rich Covalent Stains for Super-resolution microscopy and Cleared Tissue Fluorescence Microscopy" — 15 – 19 Feb 2020
Lee MY, Mao C, Vaughan JC.

Global Young Scientists Summit — Singapore
Participant awarded with GYSS travel grant — 15 – 20 Jan 2017

A*STAR Scientific Conference — Singapore
Poster "Molecular rotors as reporters for biomolecular interactions" — 21 – 22 Oct 2013
Lee MY, Goh WL, Ghadessy FJ, Brenner S, Teo YN

TEACHING EXPERIENCE

University of Washington — Seattle, WA, USA
Teaching Assistant, Chemistry — Sept 2014 – Aug 2020
Mentor, Mentor to Undergraduate Students in research lab — Jan 2016 – Aug 2020

Agency for Science, Technology and Research, Molecular Engineering Lab — Singapore
*Mentor, Mentor to Undergraduate A*STAR scholar for 2 months* — Jul 2013 – Sep 2013